LIGHTCURVE CCD SPECTROPHOTOMETRY OF PLUTO

by

Marc William Buie

A Dissertation Submitted to the Faculty of the

DEPARTMENT OF PLANETARY SCIENCES

In Partial Fulfillment of the Requirements
for the Degree of

DOCTOR OF PHILOSOPHY

In the Graduate College

THE UNIVERSITY OF ARIZONA

1 9 8 4

STATEMENT BY AUTHOR

This dissertation has been submitted in partial fulfillment of requirements for an advanced degree at The University of Arizona and is deposited in the University Library to be made available to borrowers under rules of the Library.

Brief quotations from this dissertation are allowable without special permission, provided that accurate acknowledgement of source is made. Requests for permission for extended quotation from or reproduction of this manuscript in whole or in part may be granted by the head of the major department or the Dean of the Graduate College when in his or her judgment the proposed use of the material is in the interests of scholarship. In all other instances, however, permission must be obtained from the author.

SIGNED: _____

To the unknown, may it always be there.

ACKNOWLEDGEMENTS

There are many people to which thanks should be extended. A project of this size cannot be accomplished alone. For their help in data acquisition through some long and cold nights I wish to thank Michael A. DiSanti, Faith Vilas, and Bob Johnson.

Of course special thanks are always in order for the research advisor and there should be no exception for Uwe Fink. He has provided both opportune and inopportune advice that will no doubt prove invaluable to my career. It is a rare person that one can work with and against, for that quality I am extremely grateful. Many thanks are also due Marty Tomasko for providing a different point of view along with his guidance into the vagaries of scattering and the world of tau.

David Tholen was very helpful in photometric matters concerning Pluto. Bob Marcialis is to be commended for his timing in coming along with his spot model of Pluto at precisely the right time. Thanks to Steve Larson for providing equipment and guidance for astrophotography. Also appreciation is expressed for the use of his overrated computer for the preparation of this dissertation. Rich Poppen was an excellent exmaple to follow for developing better programming skills. His influence will never be forgotten.

Many thanks to all of the people that I have played softball with over the past four years. They are responsible for what sanity I have managed to retain during this educational process. Another person

responsible for helping me maintain my wits is John Spencer. His company on many hikes is appreciated as are the many discussions about this research that we've had over the years.

Finally, deep appreciation is expressed to my wife. Her patience and understanding have made it all possible. She also was the only one that had to put up with all of my ogre phases that came along with the work I had to put in for each major hurdle toward the degree. There really ought to be more of a reward for her at the end of all this.

Many thanks as well to my brother Ken for the frontispiece. It turned out to be more appropriate than he thought.

TABLE OF CONTENTS

LIST OF TABLES

LIST OF ILLUSTRATIONS

LIST OF ILLUSTRATIONS--Continued

ABSTRACT

An observational program was carried out to investigate the spectrum of Pluto at various points on its lightcurve. Spectrophotometry of Pluto in the wavelength range of 5600 to 10500 Å was obtained on four nights covering lightcurve phases of 0.18, 0.35, 0.49, and 0.98. The four phases included minimum light (0.98) and one near maximum light (0.49). The spectra reveal variations in the absorption depths of the methane bands at 6200, 7200, 7900, 8400, 8600, 8900, and 10000 Å. The minimum amount of absorption was found to occur at minimum light.

A model for the surface and atmosphere of Pluto was constructed in an attempt to explain the phase variation observed. The model is based upon a previous photometric two-spot model which was constructed to explain the variations in the lightcurve from 1950 to 1982. Two dark circular spots (46° and 28° in radius, both at latitude -23°, separated by 134° in longitude) were used to constrain the surface distribution of methane frost on the surface of Pluto. The reflectance properties of the two terrains were modelled with a theory by B. Hapke (J.G.R., v. 86, p. 3039, 1981) which includes the effects of multiple scattering in the surface frost. The particle size and continuum optical depth of the frost particles were allowed to vary between the dark regions inside the spot boundaries and the brighter regions surrounding the spots. The transmission of the atmosphere was calculated using the Mayer-Goody band model.

The model fit to the spectrum required the presence of a frost with particle sizes on the order of 1-20 mm in order to explain the observed phase dependence of the methane bands. Using only the atmosphere and no surface frost implies a variation in column abundance of 30% within three days. From energy balance considerations this variation in column abundance is not possible. By including the absorption of methane frost on the surface a range of model solutions was obtained. This range yields an approximate limit of 5.5 m-amagats to the amount of gas that can be present and still achieve a good fit to the phase variation of the 7200 Å band. If the atmosphere is removed from the model an equally good fit to the 7200 Å band is obtained.

A major problem with the model is its failure to reproduce the relative absorption band depths. The gaseous atmospheric calculation on the other hand can fit the spectrum quite well. Possible explanations include a particle size distribution within a given terrain.

CHAPTER 1

INTRODUCTION

Previous observations of Pluto have revealed a very interesting planet. Its orbit has the largest semimajor axis and eccentricity of any known planet in the solar system. This gives it a perihelion distance of 29.58 AU and an aphelion distance of 49.3 AU (eg. Allen, 1976). Pluto's large heliocentric distance offers an excellent opportunity to study a very low surface temperature body that undergoes a large temperature variation during a Plutonian year.

Photometry since 1955 has yielded a lightcurve which may be attributed to albedo variations on the surface (eg. Marcialis, 1983). In the course of a Plutonian year different aspects are exhibited due to the large obliquity and thus may reveal the distributions of light and dark materials.

Photometric studies by Cruikshank et al., (1976); Cruikshank and Silvaggio, (1980); and spectroscopic studies by Soifer et al., (1980); Fink et al.,(1980); and Apt et al., (1983) have shown the presence of methane. A methane atmosphere and surface frost have both been called upon to explain the observed absorption features. At medium to low resolution methane frost and gas display such similar spectra that it is difficult to decide between the two interpretations.

The purpose of this research was to reconcile all of the photometric and spectroscopic information by obtaining new observations

of Pluto. The spectrograph used by Fink et al. (1980) was the instrument used for the new observations because it had demonstrated the ability to acquire a good signal-to-noise spectrum within a single night. With this instrument and the rotational period of Pluto of about 6 days it was possible to gather many spectra covering a range of lightcurve phases.

The lightcurve provides valuable information for deciding between gaseous or solid methane. If the absorptions were due entirely to a uniform atmosphere the equivalent width of the bands should not change as Pluto rotates. A non-uniform frost, on the other hand, would show a variation.

Observations were carried out at the 154 cm Catalina telescope as indicated in Table 1. Chapter 2 contains a description of the techniques used while gathering the data. A presentation of the data reduction methods is given in Chapter 3. Finally, the analysis of this data as it relates to the question of methane gas or frost is presented in Chapter 4.

Table 1

Log of Observations

OBJECT	DATE	START TIME (UT)	EXPOSURE TIME(sec)	AIR MASS	ROTATIONAL PHASE
SAO 120312	1983 Apr 18	5:05:37	25	1.462	
		5:06:27	25	1.462	
		5:43:16	25	1.310	
		5:44:15	25	1.306	
		6:10:49	25	1.232	
		6:11:45	25	1.230	
		6:39:52	25	1.178	
		6:40:47	25	1.177	
109 Virgo	1983 Apr 18	7:33:11	0.12	1.189	
		7:34:40	0.12	1.188	
		7:35:17	0.12	1.186	
		7:36:05	0.12	1.185	
Pluto	1983 Apr 18	7:41:26	600	1.120	0.185
		7:52:30	600	1.121	0.186
SAO 120312	1983 Apr 18	8:05:40	25	1.132	
		8:06:40	25	1.133	
Pluto	1983 Apr 18	8:10:46	600	1.128	0.188
		8:21:54	600	1.135	0.190
SAO 120312	1983 Apr 18	8:35:49	25	1.153	
		8:36:46	25	1.154	
Pluto	1983 Apr 18	8:39:54	600	1.153	0.192
		8:51:07	600	1.168	0.193
SAO 120312	1983 Apr 18	9:05:57	25	1.261	
		9:06:56	25	1.196	
Pluto	1983 Apr 18	9:10:15	600	1.200	0.195
		9:22:17	600	1.226	0.196
SAO 120312	1983 Apr 18	9:36:25	25	1.261	
		9:37:22	25	1.262	

Table 1, Log of Observations

OBJECT	DATE	START TIME (UT)	EXPOSURE TIME(sec)	AIR MASS	ROTATIONAL PHASE
Pluto	1983 Apr 18	9:41:24	600	1.276	0.198
		9:53:00	600	1.312	0.200
		10:05:07	600	1.356	0.201
		10:16:48	600	1.405	0.202
SAO 120312	1983 Apr 18	10:29:58	25	1.462	
		10:30:59	25	1.467	
SAO 120312	1983 Apr 19	5:59:03	25	1.252	
		6:00:32	25	1.249	
Pluto	1983 Apr 19	6:07:46	600	1.212	0.332
		6:18:59	600	1.190	0.333
SAO 120312	1983 Apr 19	6:32:46	25	1.183	
		6:33:45	25	1.181	
Pluto	1983 Apr 19	6:37:00	600	1.161	0.335
		6:49:59	600	1.146	0.336
SAO 120312	1983 Apr 19	7:02:50	25	1.147	
		7:03:53	25	1.146	
Pluto	1983 Apr 19	7:08:46	600	1.130	0.338
		7:19:52	600	1.124	0.339
SAO 120312	1983 Apr 19	7:32:53	25	1.130	
		7:33:50	25	1.130	
Pluto	1983 Apr 19	7:37:04	600	1.120	0.341
		7:48:52	600	1.121	0.343
SAO 120312	1983 Apr 19	8:01:50	25	1.133	
		8:02:46	25	1.133	
Pluto	1983 Apr 19	8:05:35	600	1.127	0.344
		8:16:34	600	1.134	0.346
		8:28:03	600	1.144	0.347
		8:39:29	600	1.157	0.348
SAO 120312	1983 Apr 19	8:51:56	25	1.178	
		8:52:53	25	1.180	

Table 1, Log of Observations

OBJECT	DATE	START TIME (UT)	EXPOSURE TIME(sec)	AIR MASS	ROTATIONAL PHASE
109 Virgo	1983 Apr 19	9:07:00	0.12	1.183	
		9:07:31	0.12	1.183	
SAO 120312	1983 Apr 19	9:13:47	25	1.217	
		9:14:42	25	1.219	
Pluto	1983 Apr 19	9:19:16	600	1.228	0.352
		9:31:12	600	1.258	0.354
		9:42:32	600	1.291	0.355
		9:53:49	600	1.329	0.356
SAO 120312	1983 Apr 19	10:06:59	25	1.375	
		10:07:53	25	1.379	
Pluto	1983 Apr 19	10:11:12	600	1.398	0.358
		10:22:36	600	1.452	0.359
		10:33:51	600	1.513	0.361
		10:46:09	600	1.590	0.362
SAO 120312	1983 Apr 19	10:59:18	25	1.677	
		11:08:00	25	1.743	
109 Virgo	1983 Apr 19	11:19:12	0.12	1.612	
		11:19:52	0.12	1.619	
SAO 120312	1983 Apr 20	5:00:32	25	1.452	
		5:01:33	25	1.447	
Pluto	1983 Apr 20	5:21:15	600	1.332	0.483
		5:32:38	600	1.293	0.484
SAO 120312	1983 Apr 20	5:44:51	25	1.281	
		5:45:45	25	1.278	
Pluto	1983 Apr 20	5:48:28	600	1.248	0.486
		5:58:52	600	1.222	0.487
SAO 120312	1983 Apr 20	6:11:21	25	1.215	
		6:12:15	25	1.213	
Pluto	1983 Apr 20	6:15:12	600	1.189	0.489
		6:26:09	600	1.171	0.490

Table 1, Log of Observations

OBJECT	DATE	START TIME (UT)	EXPOSURE TIME(sec)	AIR MASS	ROTATIONAL PHASE
SAO 120312	1983 Apr 20	6:42:50	25	1.164	
		6:43:50	25	1.163	
Pluto	1983 Apr 20	6:47:08	600	1.145	0.492
		6:57:43	600	1.135	0.494
SAO 120312	1983 Apr 20	7:10:09	25	1.138	
		7:11:08	25	1.138	
Pluto	1983 Apr 20	7:13:41	600	1.125	0.495
		7:30:42	600	1.120	0.497
SAO 120312	1983 Apr 20	7:43:14	25	1.129	
		7:44:20	25	1.129	
Pluto	1983 Apr 20	7:48:41	600	1.122	0.499
		7:59:04	600	1.126	0.500
SAO 120312	1983 Apr 20	8:10:48	25	1.139	
		8:11:41	25	1.139	
109 Virgo	1983 Apr 20	8:14:48	0.12	1.160	
		8:15:31	0.12	1.160	
Pluto	1983 Apr 20	8:19:37	600	1.140	0.503
		8:30:43	600	1.151	0.504
		8:41:35	600	1.165	0.505
		8:52:15	600	1.182	0.506
SAO 120312	1983 Apr 20	9:05:09	25	1.208	
		9:06:02	25	1.209	
Pluto	1983 Apr 20	9:08:42	600	1.213	0.508
		9:19:20	600	1.238	0.509
		9:30:24	600	1.267	0.510
		9:41:09	600	1.299	0.511
SAO 120312	1983 Apr 20	9:53:29	25	1.340	
		9:54:21	25	1.343	
109 Virgo	1983 Apr 20	10:01:21	0.12	1.289	
		10:01:52	0.12	1.291	

Table 1, Log of Observations

OBJECT	DATE	START TIME (UT)	EXPOSURE TIME(sec)	AIR MASS	ROTATIONAL PHASE
Pluto	1983 Apr 23	7:51:00	600	1.127	0.969
		8:01:51	600	1.135	0.970
SAO 120312	1983 Apr 23	8:14:56	25	1.152	
		8:15:57	25	1.153	
Pluto	1983 Apr 23	8:20:48	600	1.154	0.972
		8:31:33	600	1.168	0.974
SAO 120312	1983 Apr 23	8:43:38	25	1.190	
		8:45:00	25	1.192	
Pluto	1983 Apr 23	8:47:24	600	1.194	0.975
		8:58:25	600	1.217	0.976
SAO 120312	1983 Apr 23	9:10:40	25	1.246	
		9:11:37	25	1.248	
Pluto	1983 Apr 23	9:14:39	600	1.256	0.978
		9:25:12	600	1.287	0.979
		9:35:47	600	1.322	0.980
SAO 120312	1983 Apr 23	9:55:31	25	1.394	
		9:56:35	25	1.399	
109 Virgo	1983 Apr 23	10:06:21	0.10	1.191	
		10:06:57	0.10	1.190	

r = 29.891 AU . . . . . Pluto - Sun distance
d = 28.934 AU . . . . . Earth - Pluto distance
α = 0.7 degrees . . . . phase angle between the earth and the sun as seen from Pluto.

CHAPTER 2

DATA ACQUISITION

The data analyzed for this project were acquired during a one week period. This data set represents a culmination of three years of observations. Along with the observations of Pluto, data were acquired for asteroids (Vilas, 1984), comets (Johnson et al., 1984), and satellites. It was also during this phase that proper data acquisition techniques were developed. It was found that absolute spectrophotometry necessitates regular observations of the standards and comparison objects, an entrance slit at least 10" wide, careful centering of the object in the slit, good flat fielding practices, and careful attention to data reduction techniques. The techniques developed are described in more detail below. If the goal is simply to obtain a relative spectrum the requirements are less strict.

Spectrograph

The spectrograph used for the observations was a simple transmission grating system. A schematic diagram of the instrument is shown in Figure 1. The telescope focused starlight onto the entrance slit of the spectrograph. The slit used measured 18 mm high with a variable width that could be adjusted by a micrometer up to 2 mm wide. Exposures were controlled by a solenoid driven shutter blade located just behind the slit jaws. From the slit the light passed through a

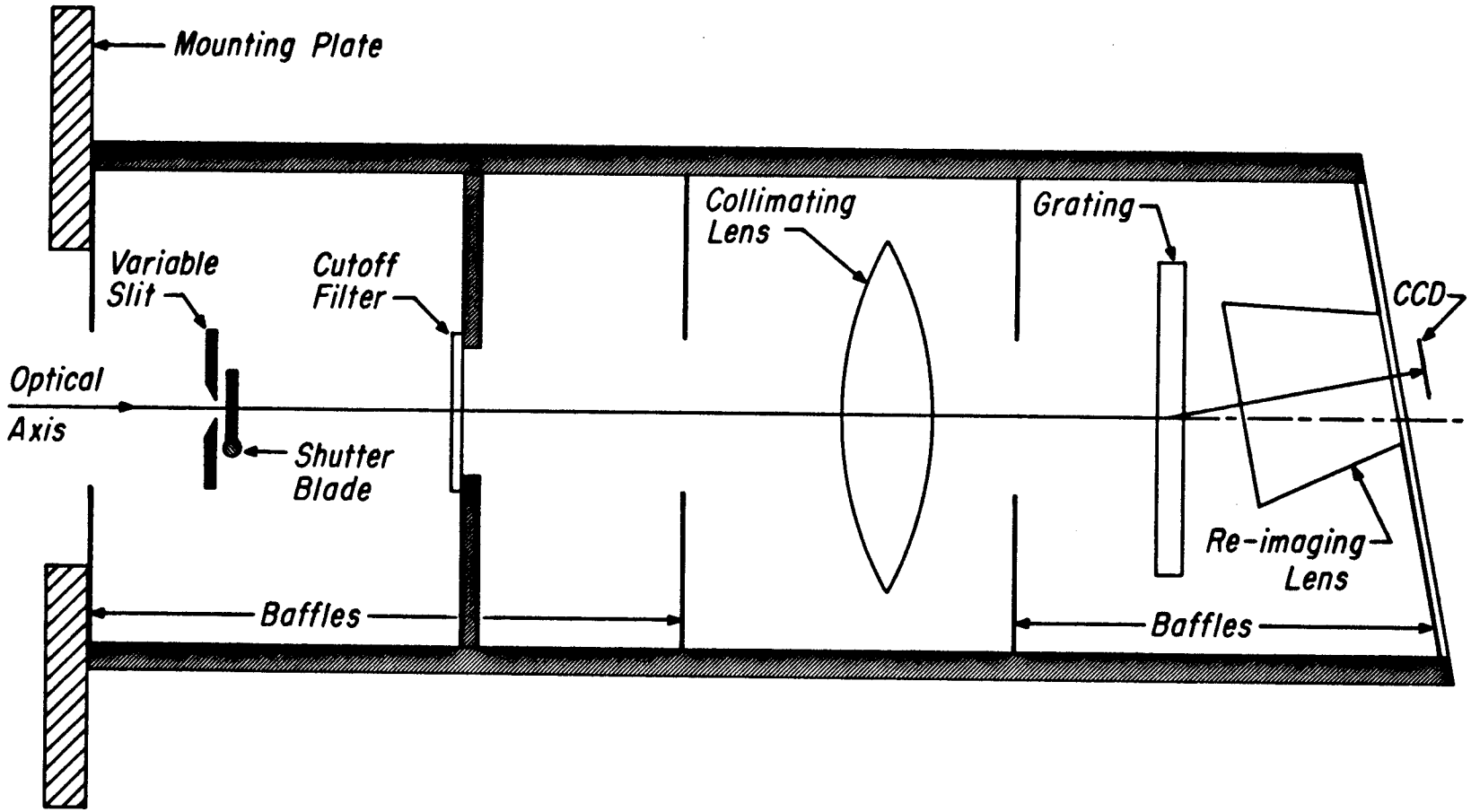

Figure 1 Schematic Diagram of Spectrograph

Light from the telescope enters from the left. The baffles indicate physical obstructions within the spectrograph to block out stray light.

Schott RG 570 filter which transmitted longward of 5600 Å. This cutoff filter was necessary since the different orders of the diffracted light overlap in the final image plane. The instrument thus had an effective bandpass from 5600 Å to 11000 Å, the infrared limit being determined by the detector sensitivity fall off. The diverging beam was collimated, dispersed by the grating, and imaged onto the detector with a f/1.4 camera lens. The grating used was a Bausch and Lomb replica grating with a ruling of 200 lines/mm and blazed for 9150 Å in first order.

This design was chosen to match the f/13.5 beam supplied by the 154 cm Catalina telescope, make the alignment simple and expedient, and reduce the amount of light lost within the instrument by minimizing the number of optical elements. The spectrograph was about 2 meters long, a length which proved to be cumbersome at times.

The image scale at the entrance slit was 10 "/mm, yielding a field of view of 180" along the slit and up to 20" across the slit. The slit width was thus comparable to standard photometric apertures. The reduction of the beam by the final lens gave a scale of about 80 "/mm along the length of the slit and a dispersion of about 700 Å/mm.

Included in the spectrograph but not shown on Figure 1 were two eyepieces for positioning the object in the slit. The first provided a 2' field of view for indentification and coarse positioning. The second and most heavily used looks through the slit itself and permits the observer to center the object in the slit. The design required using the human eye for the task of centering. This turned out to be

the limiting factor in determining how faint the spectrograph could be effectively used. For a dark night this limit was about magnitude 17.

The duration of an exposure was controlled by a simple digital countdown circuit. The duration of an exposure was measured to be accurate to 0.05% from 100 milliseconds to 30 minutes. Below 100 milliseconds the accuracy slowly deteriorated, falling to 9% at 10 milliseconds. There was a systematic error in the timing circuit such that the ratio of actual exposure time to the selected value was 98.4 ± 0.4. This correction was not used since exposure times only appeared as a ratio to another exposure time and the constant divides out.

CCD Camera

The detector employed for all of the observations was a Charge Coupled Device (CCD) array manufactured by Texas Instruments for the Space Telescope camera. The CCD and its associated readout electronics was used in cooperation with the Space Telescope Wide Field Planetary Camera investigation definition team (Team members are: W. B. Baum, A. D. Code, D. G. Currie, G. E. Danielson, J. E. Gunn, T. Kelsall, J. Kristian, C. R. Lynds, P. K. Seildelman, B. A. Smith, and J. A. Westphal).

Each detector element on the CCD measured 15 microns on a side. The total size of the array was 800 x 800 pixels. This particular CCD had only 3 bad columns so that very little work was needed to eliminate chip defects. Combining the size of the pixels with the magnification of the telescope and the spectrograph optics yielded a scale of about

1.2 "/pixel perpendicular to the spectrum and 10.6 Å/pixel along the spectrum. For spectroscopy only a portion of the chip was used since the spectrum only occupied 150 x 500 pixels (cf. Figure 3). This permitted avoiding bad areas of the chip which improved the quality of the data. The full width of the CCD was not utilized because the spectograph was originally designed for a 500 x 500 TI CCD.

The spectral response of the CCD was well suited to the task of showing the methane features in Pluto's spectrum. Figure 2 shows a plot of quantum efficiency vs. wavelength (Gunn and Westphal, 1981). The peak efficiency of 80% plus the design of the instrument helped to bring the total instrumental efficiency nearly up to that of a standard photometer.

The gain of the electronic readout system was 1 (Westphal 1981), implying that one count represents one electron/hole pair or one photon detected. Throughout the rest of this document counts and photons will be used interchangably. Noise estimates done on the system (Westphal, 1981) indicate that the readout noise was about 10 electrons. This means that for any count above 100 the dominant source of noise is due to photon counting statistics.

An important consequence of the low noise level was the relatively large dynamic range it allowed. The full well capacity of a pixel for the CCD used was about 60,000 counts. The linearity of the chip, however, began to fail at $\sim$50,000 counts. A properly exposed spectrum is one for which the exposure time is of sufficient length to bring the brightest regions up to this level of non-linearity. This yielded a dynamic range of 5000 for the photon counting noise limited

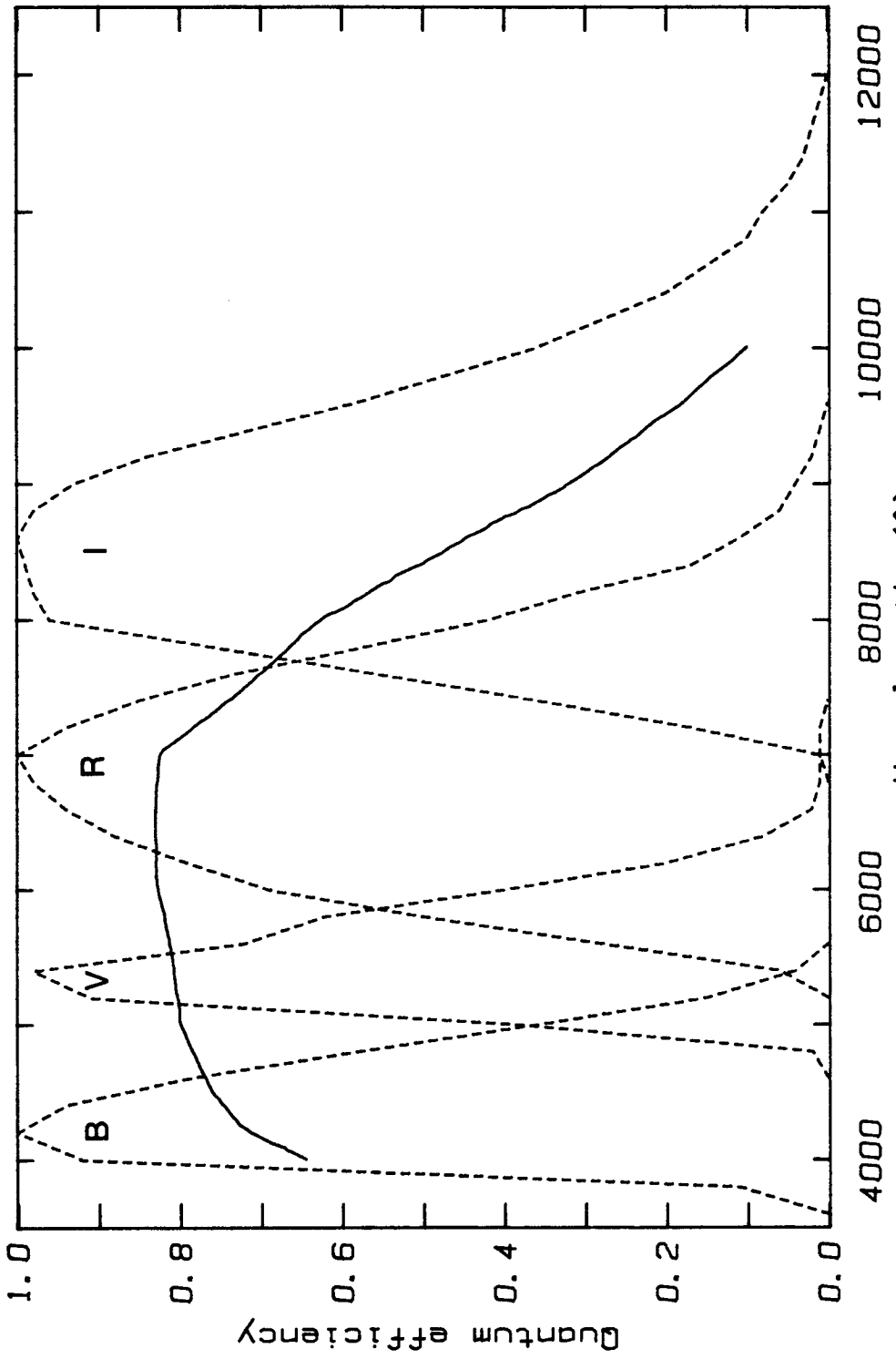

Figure 2 Quantum Efficiency of CCD

The solid curve shows the quantum efficiency of the CCD. The dashed curves show the filter response curves for the standard BVRI filters from Johnson (1980).

regime. Effectively this meant that for bright objects (negligible sky contribution) the infrared wavelength cutoff near 1 micron occurred where the signal fell below about 100 counts. For faint objects the large sky signal must be considered in addition to the object photons in the determination of the limiting wavelength cutoff.

Observational Techniques

All observations in this work were made using a 1 mm wide slit, corresponding to a 10" aperture. This width ensured that all of the light was passed through the slit, which is necessary for good photometric results. Unfortunately this wide slit admitted more sky signal than optimal for obtaining the best signal-to-noise ratio. For a more complete description of this effect refer to Chapter 3.

An important adjustment was the rotation of the camera with respect to the spectrograph, such that the principal axes of the spectrum were exactly aligned with the rows and columns on the CCD. When this adjustment is made the pixels within a column sample the intensity profile along the slit at a fixed wavelength. If the spectrum is skew it is necessary to interpolate the pixel counts to obtain the intensity profile. To facilitate the data reductions this rotational adjustment was always carried out at the start of each observing run.

Before starting an exposure the object was carefully centered in the slit. This step ensured that the spectra were always recorded on nearly the same pixels of the CCD. When the same pixels are used the need for flat field corrections is minimized and the data

reductions are more routine. Centering was also important for eliminating light loss at the entrance slit which would affect the photometric accuracy of the data.

During the observations special care was taken to track the object accurately during integration. The longest single exposure on Pluto was 10 minutes. In order to allow corrections for telluric absorptions all observations of Pluto were sandwiched between exposures of the G-type star, SAO 120312 (cf. Table 1). This regular sampling of a comparison star throughout the night also made it possible to determine extinction coefficients for each night, necessary for the final absolute calibration. As well as monitoring air mass effects, this procedure monitored slow seeing changes which affect the amplitude of the channel fringes (see Chapter 3). SAO 120312 was chosen for its proximity to Pluto, similarity in color to the sun and its reletively low brightness level (Mv=9.2). The latter allowed long enough exposures ($\sim$25 seconds) to average out seeing fluctuations so that spectra of the comparison star were of seeing disk averages and thus comparable to Pluto.

Flat fields for these observations were acquired at the telescope by illuminating the inside of the dome with a high intensity lamp. With the telescope focused at infinity this provided quite a uniform illumination of the slit. The flat field is strongly dependent on the slit width used because of the channel fringes (see Chapter 3). For this reason the flat fields were recorded at the same slit width as used for the objects. Tests were carried out which verified that the flat fields effectively removed sensitivity variations without

introducing spurious features that would depend on the lamp or the reflecting surface used.

The wavelength dispersion of the instrument was calibrated using emission lamps of helium and xenon which provided lines throughout the spectrum. These standards were recorded at the observatory just before mounting the instrument on the telescope and assured good calibration for that particular mating of the camera and the spectrograph. The camera/spectrograph combination remained fixed to the telescope during the entire observing run. It is not known if this was necessary but given the limited amount of time the CCD camera was available it was felt to be the safest procedure.

CHAPTER 3

DATA REDUCTION

Long slit spectrophotometry using CCD detectors is a relatively recent instrumental development. In fact, the first published CCD spectrum (a spectrum of Pluto in the 8900 Å region that clearly showed the presence of methane) was obtained with the same spectrograph but with a different CCD only four years ago by Fink et al. (1980). Since that time new techniques for the data reduction process have been developed to improve the quality of the final data. Several of these will be described in the following sections. The two most important are cosmic ray event removal and shifting by partial pixels. If not corrected both are important non-random noise sources that can be considerably larger than photon noise.

This chapter traces the sequence of steps followed during the reduction process. The length of each description is not intended to convey the relative amounts of time each operation requires.

The basic format of all data that is obtained from the CCD is shown in Figure 3a. A slice perpendicular to the spectrum is shown in Figure 3b. Three basic regions contained on all spectrum images are evident. The DC bias is the portion outside the slit. It consists of dark current collected during the exposure and a constant DC offset added by the electronics to every pixel as it is read out. The sky background recorded on each image can be seen extending the full 180"

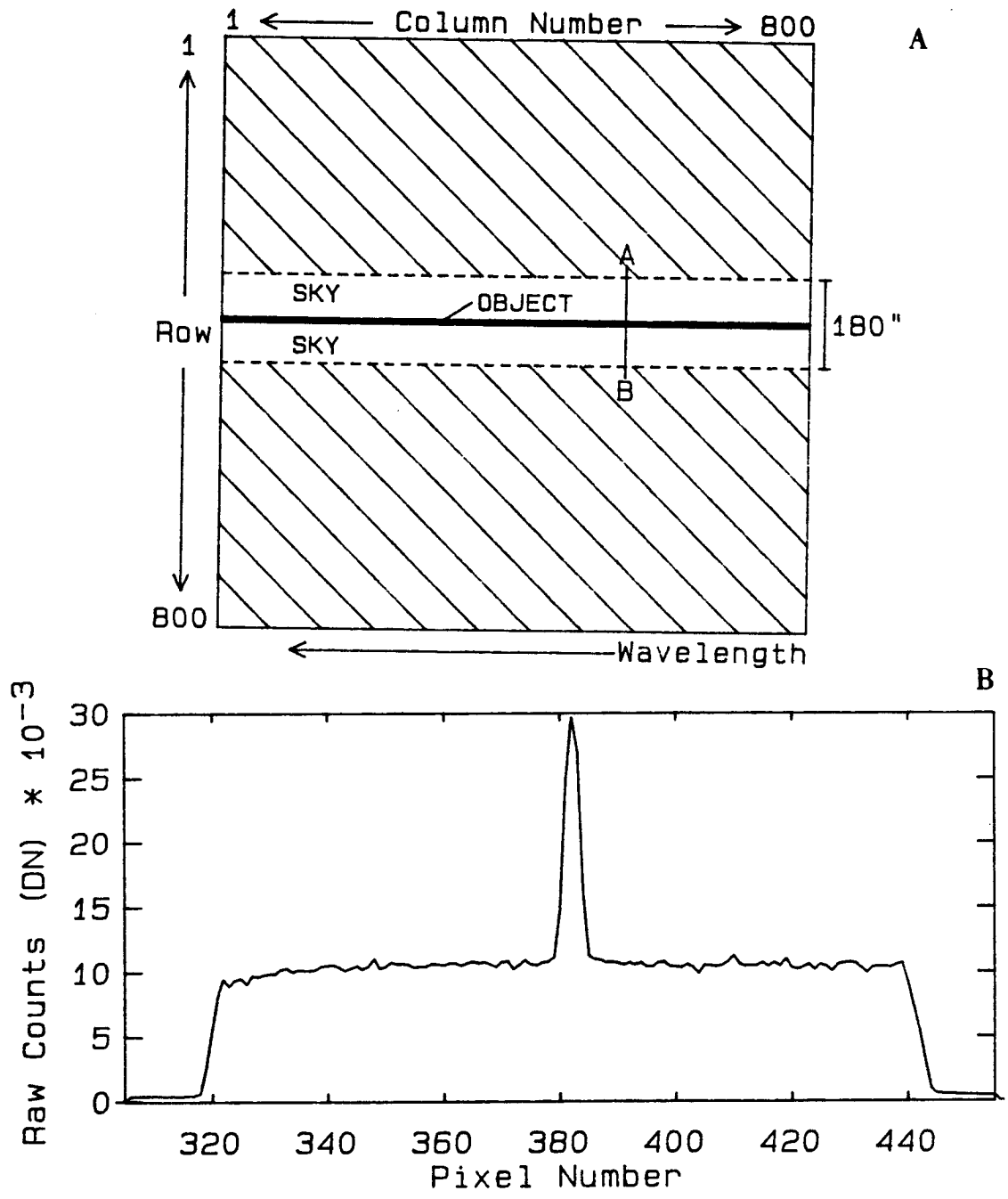

Figure 3 **Spectrum Image Format**

3a shows the basic format of a CCD spectrum image. The shaded areas are outside the slit and are not illuminated. 3b is a trace across the spectrum perpendicular to the direction of dispersion between the points A and B indicated on the schematic.

length of the slit. Light from the object over the extent of the seeing disk is displayed in the middle of the slit. The ability to simultaneously monitor the sky and object is essential for faint object spectroscopy. Any field stars that are present in the slit are also recorded. They must be avoided when measuring the sky background level during the data reduction process.

Cosmic Ray Event Removal

A cosmic ray event or strike is a generic term describing any spurious peak of counts on an original data frame. Strikes can be characterized in a variety of ways. They are basically random events that occur as non-repeatable features on separate images. On spectroscopic images where the light is dispersed, cosmic ray strikes can be distinguished as point sources. Figure 4 shows two adjacent columns from the same image. The top curve exhibits an extraneous spike which is clearly a strike because it appears only in one column.

On average, a single 10 minute exposure contained roughly 20 strikes within the 500 x 150 pixel area containing the data. Unless the effects of the strikes were removed, 20 points in the reduced spectrum would be contaminated by spurious charge. A final average of 10 spectra would then have up to 200 contaminated points. Thus the removal of cosmic ray strikes was essential for obtaining a clean spectrum.

Due to the large number of frames processed it was necessary to find an automatic procedure that would characterize a strike. Table 2 is a printout of the pixel counts near a sample strike together with

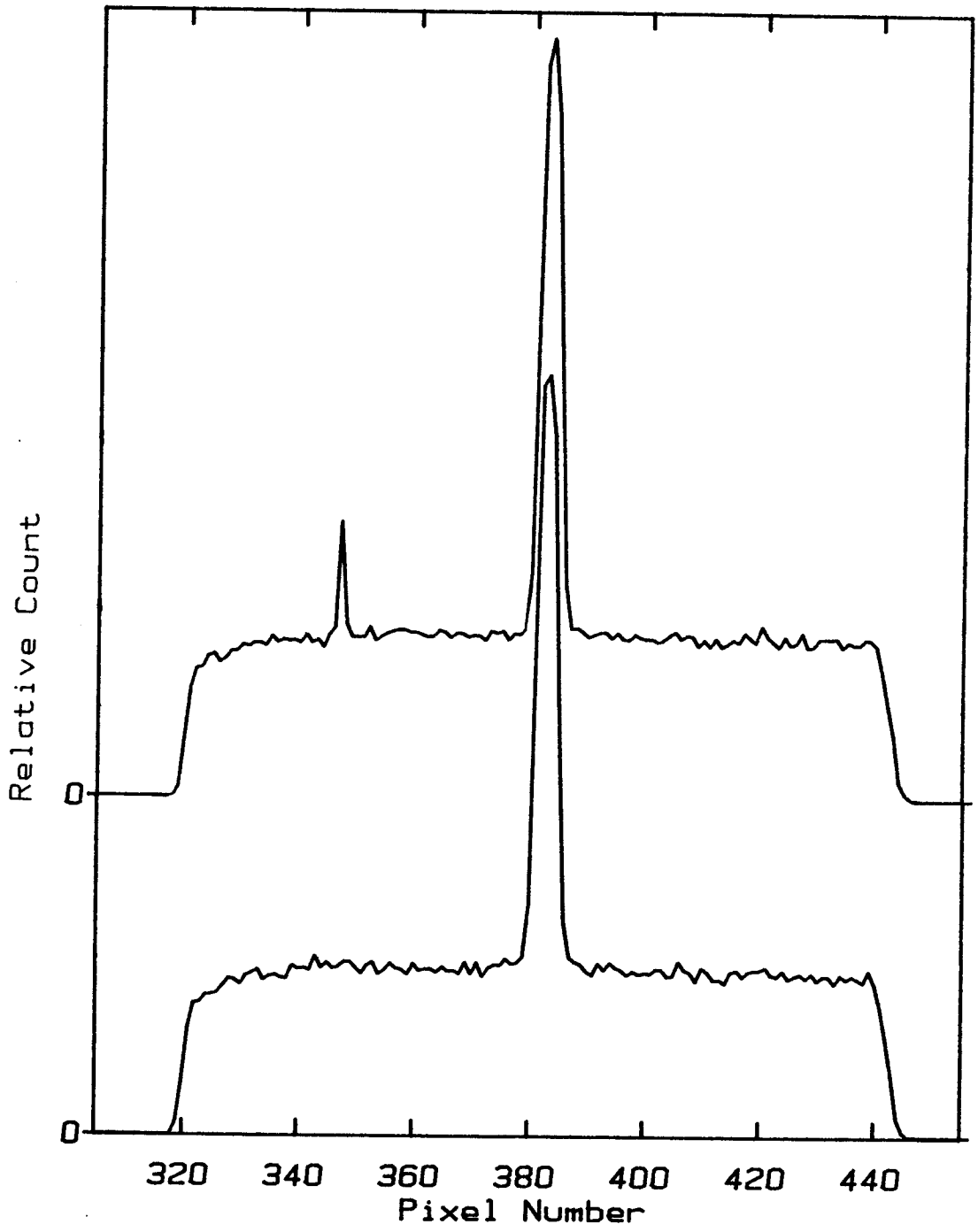

Figure 4 Cosmic Ray Identification

The two curves are slices across the spectrum at two adjacent columns on the same image. The smaller secondary peak is due to a cosmic ray strike.

Table 2

Cosmic Ray Event

Counts

(Column) Row>	(437)	(438)	(439)	(440)	(441)	(442)	(443)
344>	4470	4452	4085	4195	4741	4914	4874
345>	4332	4346	4368	4586	4899	4744	4982
346>	4514	4609	4474	4789	4730	5163	4976
347>	4581	4521	5992	7735	4786	4719	4941
348>	4422	4527	4426	4853	4918	4975	4838
349>	4597	4516	4243	4485	4913	4813	4856
350>	4487	4618	4259	4498	4744	4918	5049

Sigma From Mean

344>	-0.51	-0.55	-1.23	-1.02	-0.01	+0.32	+0.24
345>	-0.77	-0.74	-0.70	-0.30	+0.29	0.00	+0.44
346>	-0.43	-0.25	-0.50	+0.08	-0.03	+0.78	+0.43
347>	-0.30	-0.42	+2.33	+5.58	+0.08	-0.05	+0.37
348>	-0.60	-0.41	-0.59	+0.20	+0.32	+0.43	+0.17
349>	-0.27	-0.43	-0.93	-0.48	+0.31	+0.13	+0.21
350>	-0.48	-0.24	-0.90	-0.46	0.00	+0.32	+0.57

the deviation from the mean in units of a standard deviation. The event occured at pixel (347,440), 5.6 sigma above the mean with some nearby pixels showing smaller amounts of contamination.

The search was carried out by examining each pixel of the frame area required for generating a spectrum. The value of each pixel was compared to running averages of the pixels above, below, to the right, and to the left using the standard deviation as a discriminator. The average count and standard deviation was computed in each direction. Then the target pixel was compared to these numbers setting a flag for each direction when the target pixel count was greater than the mean plus a threshold. This threshold was usually set at four sigma. A pixel was classified as a strike if it was flagged in three or four directions. This procedure discriminated against linear features which are characteristic of spectra. The search was quite effective in locating the centers of most events.

To completely remove the effects of a strike it was necessary to visually inspect the regions around the strikes that were flagged. Plotting a histogram of these areas allowed for quick identification of any remaining outlying points which were then removed.

The procedure worked quite well in the sky area but was considerably more delicate near the object signal. The most reliable method of finding strikes in the object region was to compute a spectrum and note those features that did not repeat from spectrum to spectrum. This identified columns on the image that had strikes near the object signal.

Once identified, the cosmic ray strikes were corrected differently depending on where they occurred. In the sky region where a relatively large number of pixels were available the affected pixels were excluded from the computation of the average sky signal at that wavelength. In the object data region, the affected point was reconstructed by interpolation from nearby neighbors on the frame. For cases where this was not possible, a spectrum was calculated including the pixel with the cosmic ray strike. The affected point was then replaced by the linearly interpolated value from the two adjacent wavelengths.

Reduction from Image to Spectrum

The process of correcting for variations in the pixel sensitivity across the CCD is called flat fielding and was carried out next. The flat field frame used for the reductions was constructed by summing 8 single flat fields each of which was obtained as described in Chapter 2. Since the pixel counts were recorded as 16 bit integer values, the sum for each pixel was maintained in 32 bit floating point format. After summing the exposures each pixel was divided by 8 and converted back to a 16 bit integer value. This procedure reduced the noise in the final flat field image and ensured that no loss of precision occurred as a result of the averaging.

The peak of the object signal at all wavelengths is called the spectrum centerline and was determined by measuring the peak of column slices (cf. Figure 5). The centerlines for all of the spectra were

within a few pixels of each other thus minimizing the flat field corrections.

A spectrum was calculated by summing the light from the object at each wavelength and subtracting the sky counts according to the following formula,

$$S_i = \sum_{j=1}^{M} \frac{C_{ji} - DC}{f_{ji}} - \frac{M}{N} \sum_{k=1}^{N} \frac{C_{ki} - DC}{f_{ki}} \qquad (1)$$

where

S is the spectrum value,

M is the number of pixels in the object aperture,

N is the number of pixels in the sky aperture,

DC is the DC bias offset plus the dark count for the image,

C is the raw pixel value in the image,

f is the corresponding flat field pixel value,

i is the column number of the pixel, and

j and k are running indicies of the row number of the pixel (see Figure 3).

The first term in Equation (1) sums the counts over the object. The bias does not represent a true signal and thus is always subtracted first. The division of the object frame count by f accomplishes flat fielding. The second sum divided by N is the average sky signal per pixel. Multiplying by M yields the total sky contribution to the object sum.

Figure 5 shows profiles at 6000 and 9500 Å and the apertures used for a typical Pluto exposure. Determining exactly which rows should be used in the two sums was a critical step in obtaining precise spectrophotometry. If the object window is chosen too small, the object signal will be underestimated. On the other hand if the aperture is too large, the noise will be increased because of the inclusion of unnecessary sky signal. It should be noted that a similar effect also exists if too large a slit width is used. If the sky summation does not contain enough points the average sky signal would be poorly measured. On the other hand the region used for the sky must be free of field stars and signal due to the object. In the case shown in Figure 5 note a field star that was excluded from the sky aperture.

An expression can be derived for the signal-to-noise ratio in terms of the signal and the average sky signal from Equation (1), and the sizes of the object and sky apertures, M and N, respectively and is given by

$$\frac{S_i}{N_i} = \frac{S_i}{(S_i + M\bar{P}\ (1 + \frac{M}{N})\ )^{\frac{1}{2}}} \qquad (2)$$

This analysis summarizes a study done in collaboration with P. Hartigan. Flat fields were considered to contribute negligible noise because they are averages of many frames. Also the readout noise was considered negligible in comparison to sky and object photon noise.

A practical example of the above effect is illustrated in Figure 6. The object counts collected as the aperture is increased is

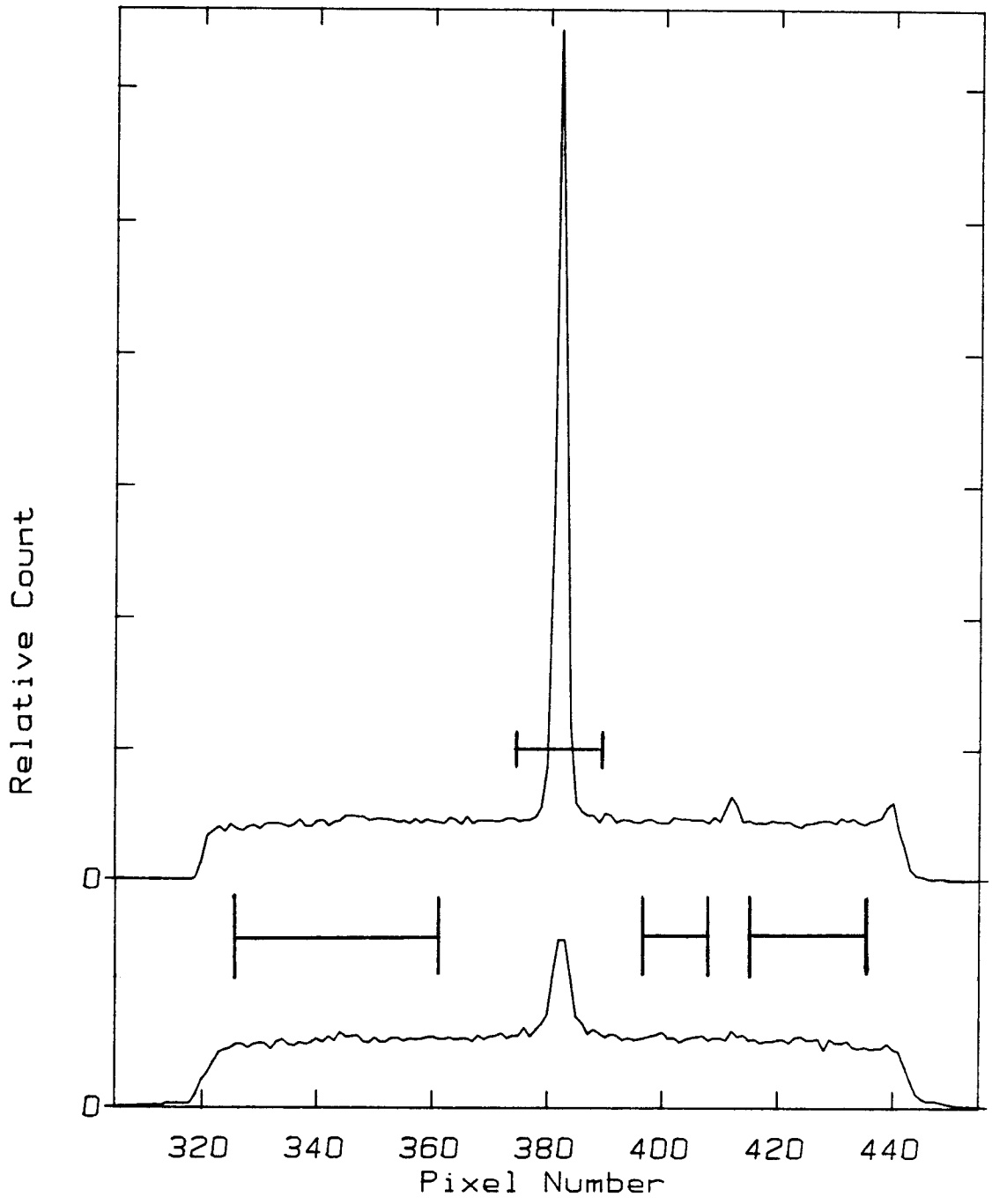

Figure 5 **Numerical Aperture**

Shown are two profiles of a Pluto spectrum image at 6000 Å and 9500 Å. The sky aperture is shown on both sides of the signal. Also shown is contamination from a field star.

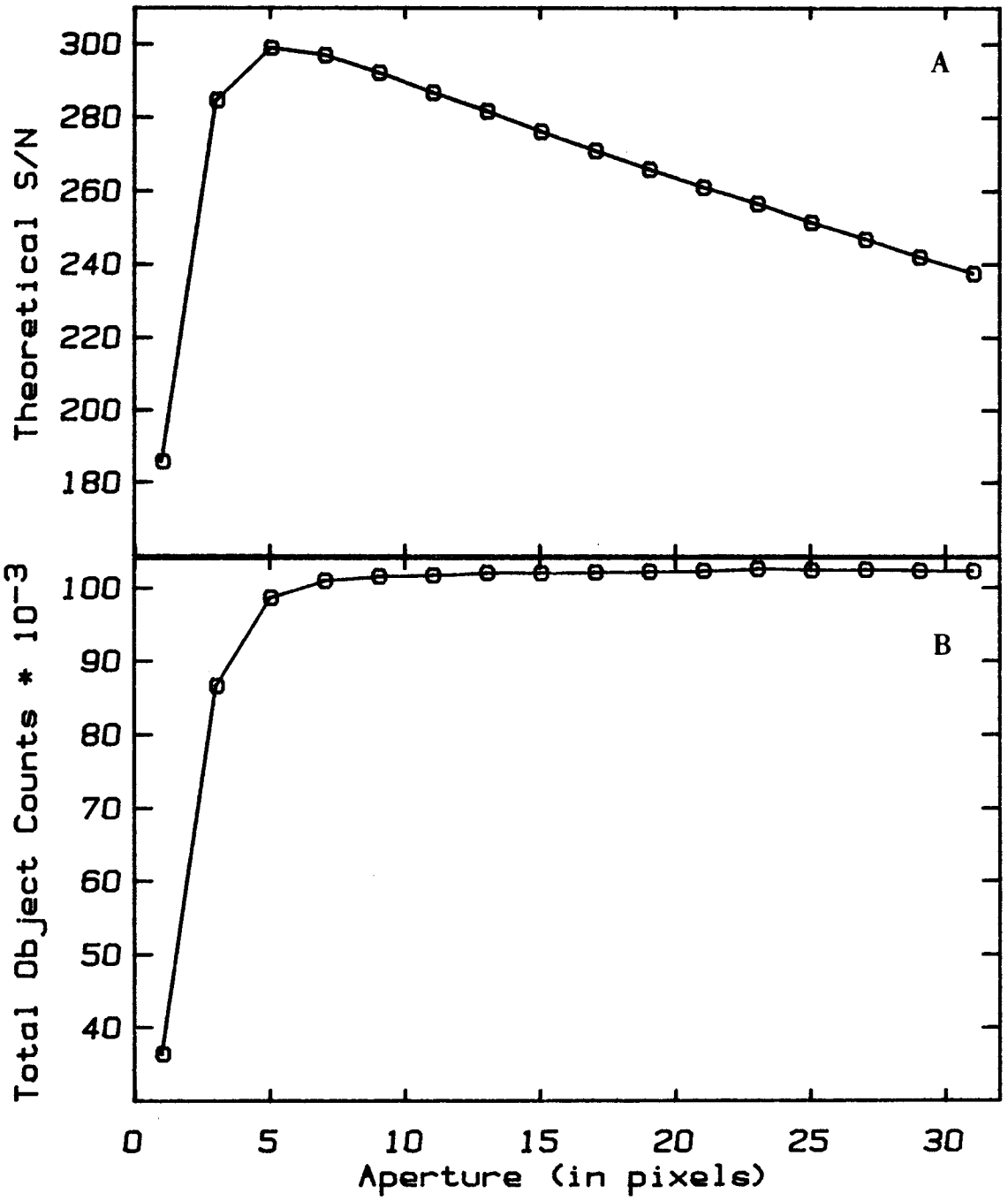

Figure 6 Signal-to-Noise Profile

Profile of signal-to-noise ratio as a function of object aperture on the top curve and sky corrected object counts appear on the bottom curve. The sky window was held constant for both profiles.

plotted in Figure 6b. An asymptotic value for the sky corrected object count is quite evident. In Figure 6a the signal-to-noise ratio is calculated from Equation (2) for the same apertures. This function peaks at an object aperture of 5 pixels and then slowly tails off.

For accurate spectrophotometry summing all the signal was considered to be the primary objective. A slight degradation of the signal-to-noise ratio was therefore allowed. For most of the data the object aperture was chosen to be 9 pixels. This yields approximately 90% of the maximum signal-to-noise. The same aperture was also used for the comparison star so that any fractional loss of light ratioed out.

Wavelength Calibration

Wavelength calibration of the data was carried out with exposures of a Helium emission lamp standard. The slit of the spectrograph was narrowed as much as possible so that the imaged emission lines would show the instrumental profile of the spectrograph. The lines at 5876, 6678, 7065, 7281, and 10830 Å were used for the calibration. Figure 7 is a plot of the calibration spectrum. The superposed curve for the 10830 Å line is of a longer exposure to bring out this line which is weak because of the failing quantum efficiency of the detector.

The dispersion determined from a linear least squares fit was 10.60 Å/pixel. The zero point calibration of 4140.10 Å at pixel 800 was determined from the position of the telluric O_2A absorption band present in all Pluto and stellar exposures. The zero point calibration

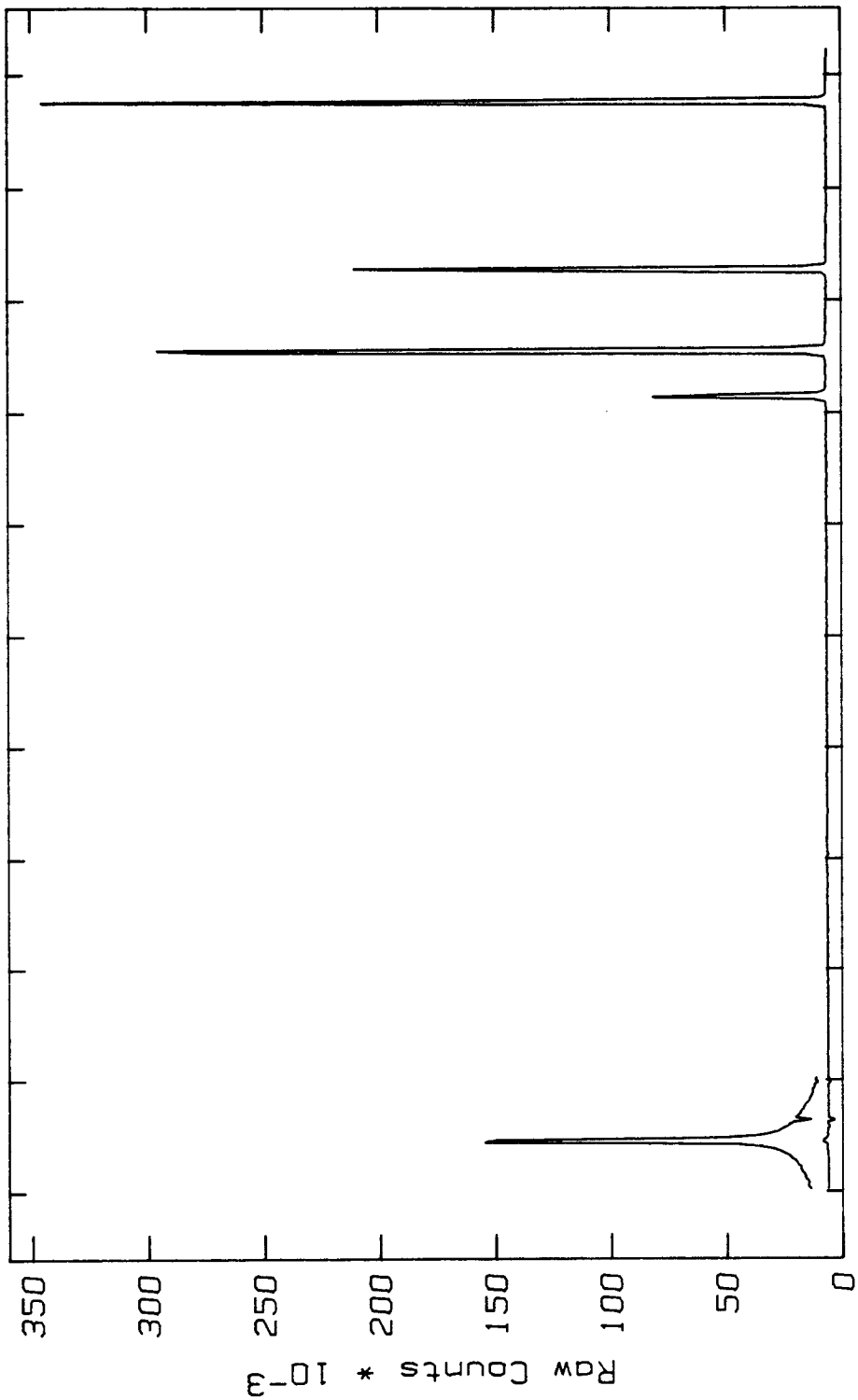

Figure 7 Wavelength Calibration Spectrum

This is a plot of the calibration spectrum versus pixel number for a Helium emission lamp. The superposed plot is of a longer exposure bringing out the 10830 Å line.

of the emmision lamp was not used because errors in positioning the object in the slit for individual exposures caused a slight wavelength shift of the spectrum on the CCD. Therefore, to obtain a precise wavelength scale it was necessary to use the known positions of telluric absorptions as reference points for each spectrum.

Figure 8 is a raw spectrum of a comparison star calculated from Equation (1). The shape of the data has been distorted severely by the flat field division. This curve shows no correspondence to the original spectrum or correlation between the signal and the signal-to-noise ratio. In order to obtain a plot that gives a close approximation to the original spectrum and at the same time is flat fielded, Figure 8 was multiplied by a flat field spectrum (Figure 9). The resulting spectrum is shown in Figure 10. All spectra are multiplied by this flat field spectrum to ensure that noisy regions are always at low signal levels. Since the final spectrum used in the analyses are all ratios of Pluto and the comparison star, the flat field spectrum will ratio out and its exact shape is not critical for the data reduction.

Shifting

Telluric absorptions and "channel fringes" are two features that are evident on Figure 10 and must be corrected. The channel fringes are caused by interference between the front and back surfaces of the relatively thin (about 16 microns) absorbing silicon layer of the CCD, which is illuminated essentially monochromatically by the spectrograph at each column. Fringes appear as a sinusoidal

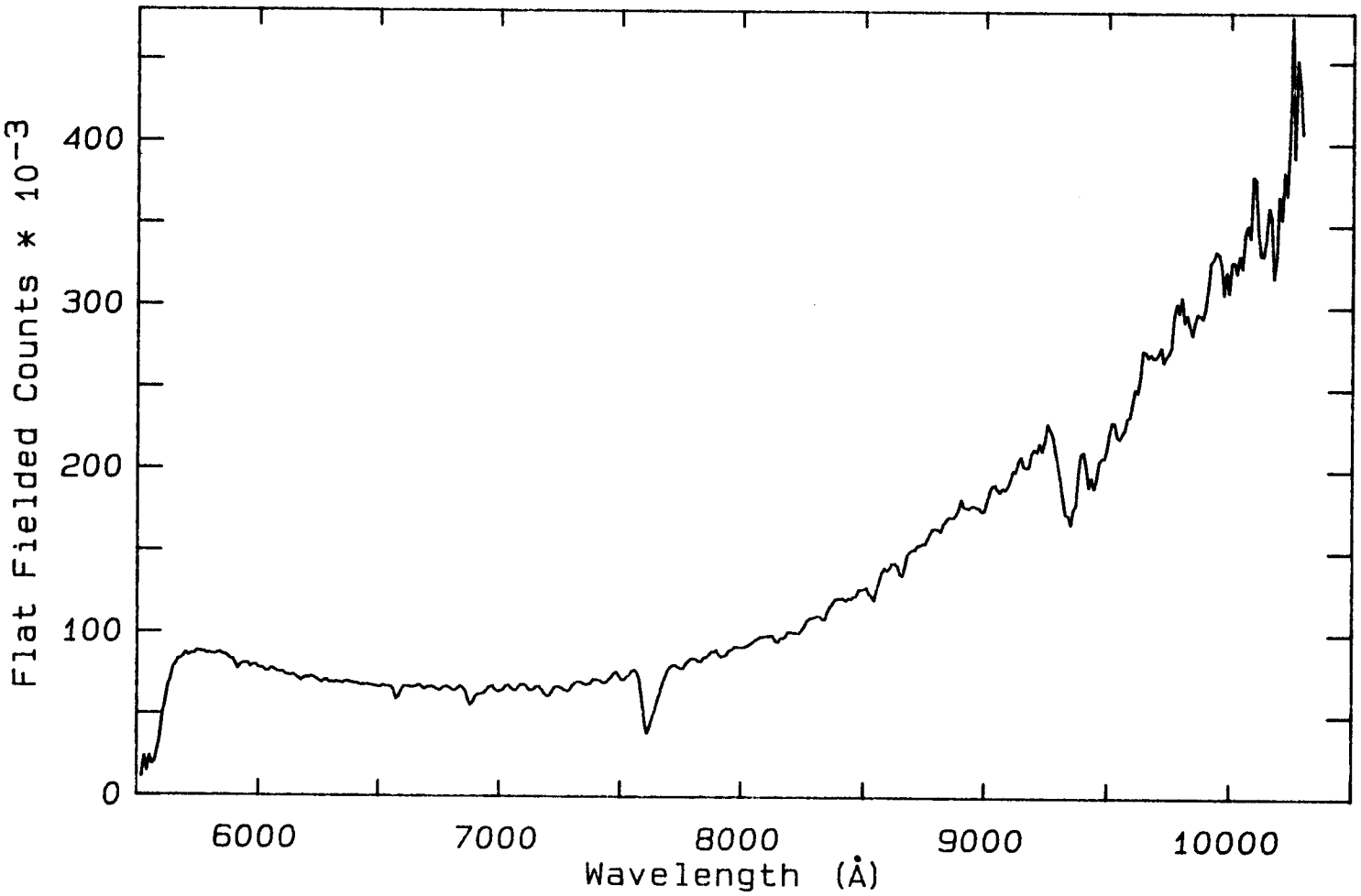

Figure 8 **Raw Comparison Spectrum**

Raw spectrum calculated from an image by using a 1 mm flat field. The overall response of the chip has been removed, thereby distorting the apparent relative strength of the signal.

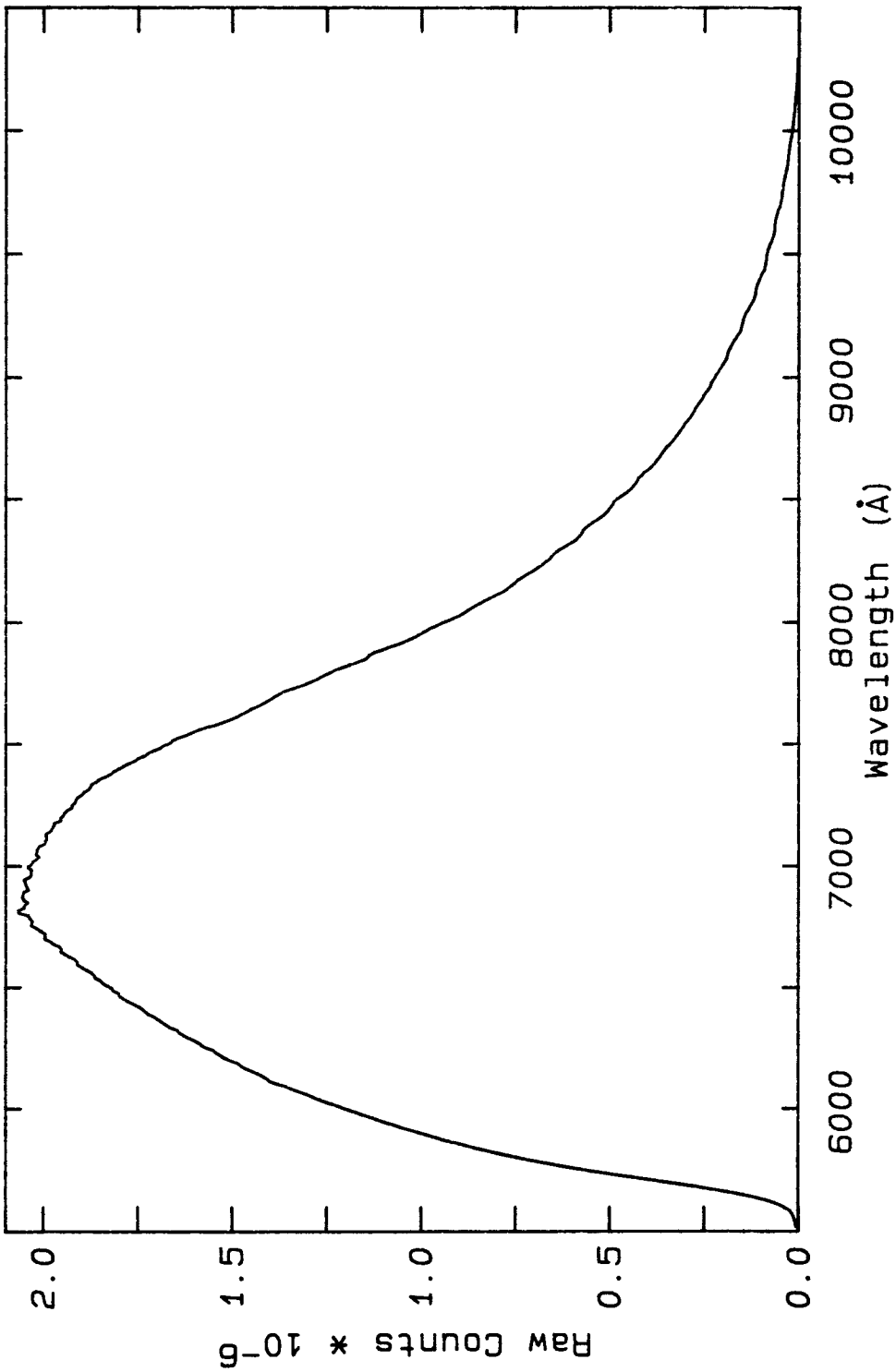

Figure 9 Flat Field Response Curve

1 mm flat field curve showing the overall response of the CCD multiplied by the flat field lamp's spectrum. This was used only as an aid to the data reductions.

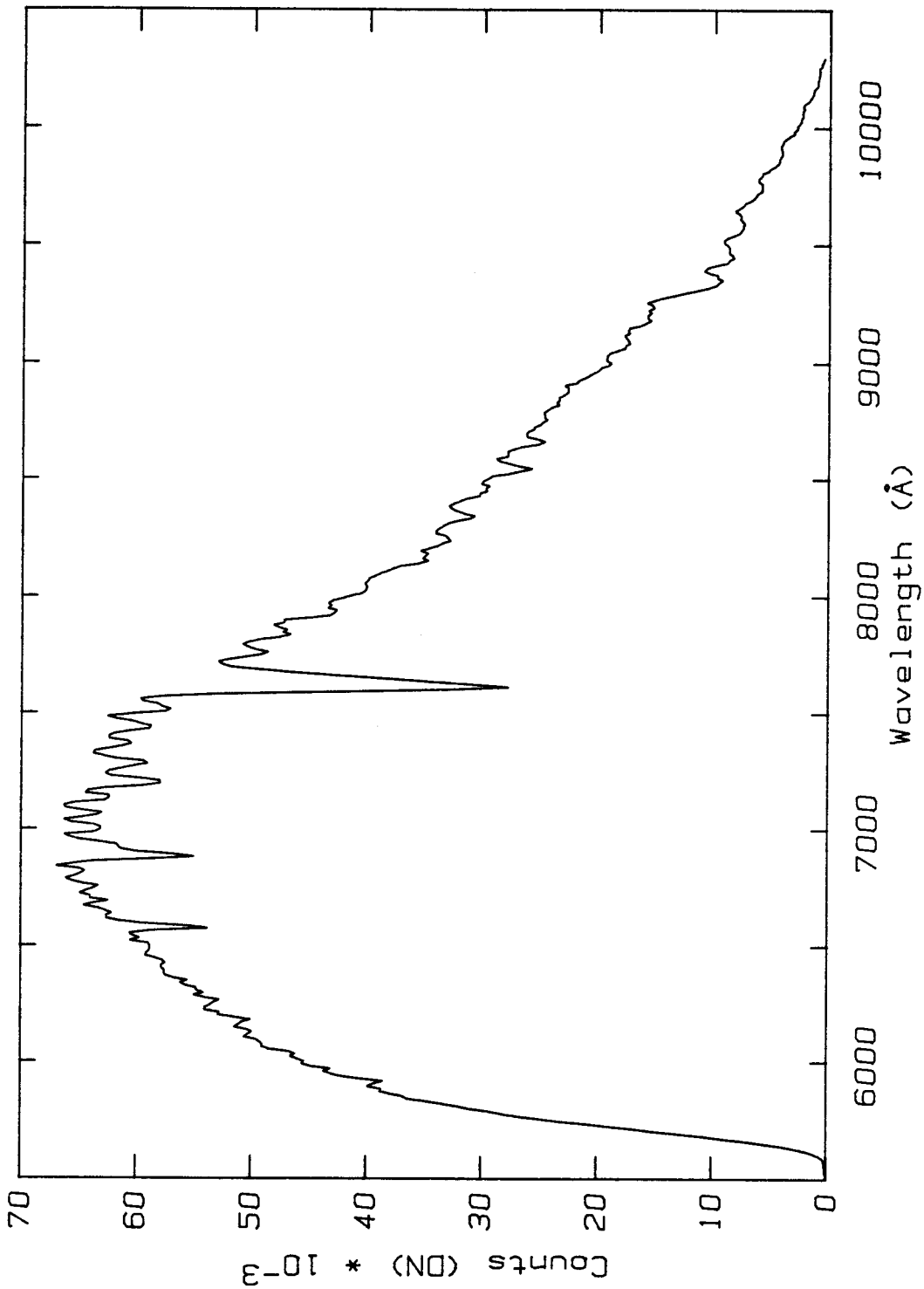

Figure 10 Wavelength Reference Spectrum

Raw spectrum of SAO 120312 that was used as a reference spectrum for shifting.

fluctuation superimposed on the data. The amplitude of the channel fringes is determined by the spectral resolution. If the seeing disk of the object is larger than the slit then the resolution is determined by the slit width, otherwise the resolution is determined by the width of the seeing profile. The dependence of the channel fringe amplitude on spectral resolution can be seen in Figure 11 which shows a flat field spectrum taken with three different slit widths.

The placement of the channel fringes on the chip is a function of the object's position in the entrance slit if the object does not fill the slit. For most cases the half intensity width of the seeing profile was 2-3" which is much smaller than the 10" slit width used. Centering within the entrance slit was accurate to within $\sim$1-3" resulting in random shifts of the spectra and their interference fringes by 1-2 pixels in the focal plane of the array. Without compensating for this misregistration between different exposures spurious noise will appear.

A spectrum represents the intensity of an object as a function of wavelength sampled at regular intervals. The exact position at which the spectrum is sampled depends critically upon where the object was placed in the slit. The error in positioning the object in the slit cannot be expected to be an integral number of pixels. Simple re-indexing will shift the data only by an integral number of pixels and shifting using interpolation to a fractional pixel value was required. The process of shifting is equivalent to re-sampling the data. The re-sampled points become the shifted spectrum at exactly the same grid interval.

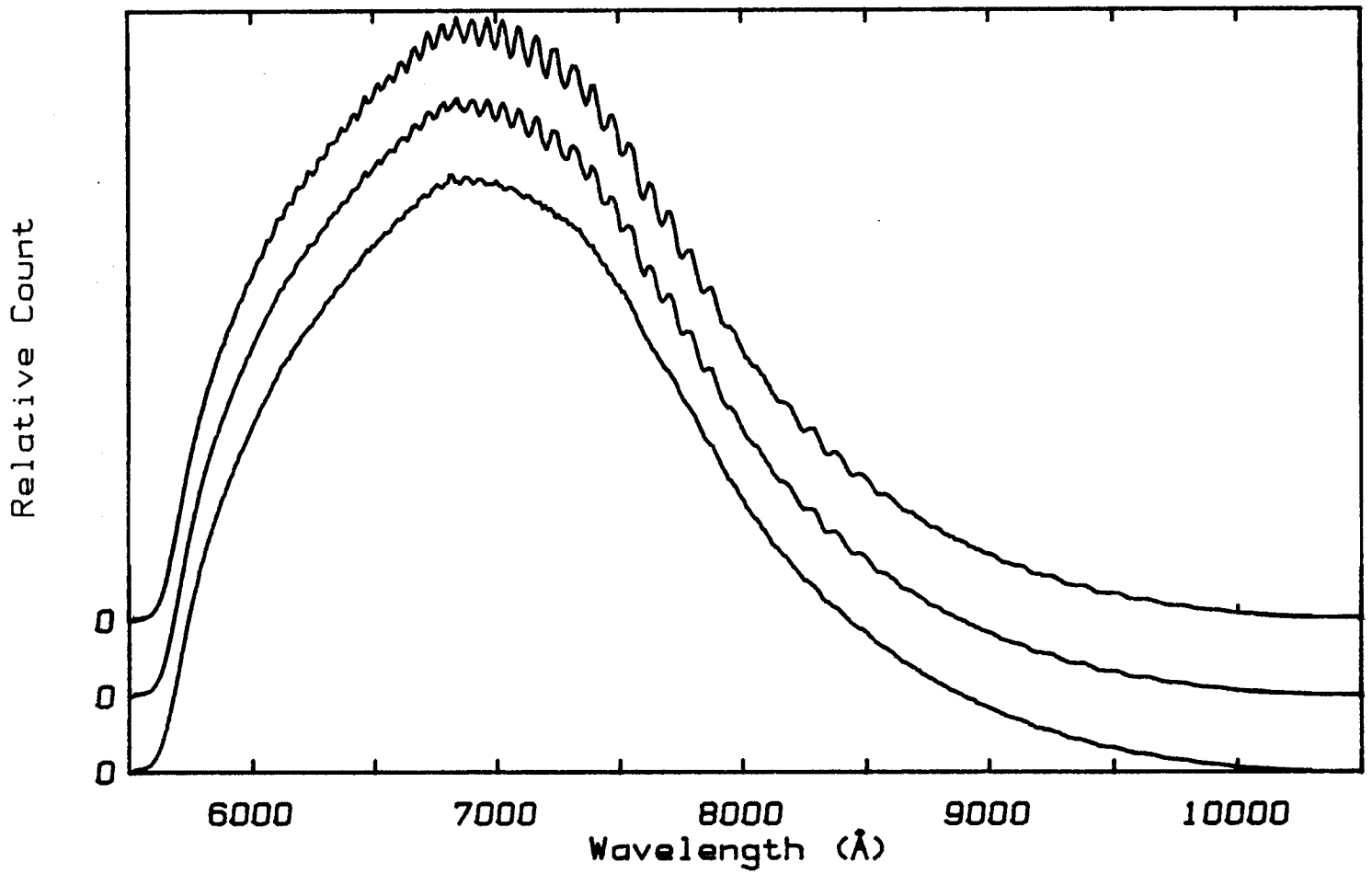

Figure 11 Channel Fringe Variation

Traces of the same row from three flat fields recorded with different slit widths. The top, middle and bottom curves correspond to 0.25 mm, 0.5 mm, and 1 mm slit widths, respectively. Note the increase in the fringe amplitude with increasing spectal resolution.

The light that falls on the detector is a continuous function of wavelength. The intensity is measured at regularly spaced intervals by the CCD. The sampling theorem requires the sampling frequency of the detector to be twice the highest spatial frequency of information contained in the spectrum. If this requirement is met the intermediate points of the spectrum can be regained from the regularly sampled data points (Bracewell, 1965). The half width of the point spread function of the the spectrograph optics was determined from the emission calibration spectra to be just over two pixels. This satisfies the requirements of the sampling theorem completely. When the requirements of the sampling theorem (Chapter 10, Bracewell, 1965) are met, interpolation, with the proper function (see below) will not change the noise level of the spectrum. This is an important consideration for achieving the highest possible signal-to-noise ratio in the data.

For a complete description and proof of the sampling theorem and its applicatios, ie. filtering, interpolation, and shifting the reader is referred to the thorough and detailed discussions in Bracewell, (1965). A brief summary is given below.

Interpolation of the measured spectrum is identical to filtering the Fourier transform of the spectrum. The simplest filter is one that does not change the Fourier transform. The sampling theorem is stated on p. 194 of Bracewell, "A function whose Fourier transform is zero for $|s| > s_c$ is fully specified by values spaced at equal intervals not exceeding $\frac{1}{2}s_c^{-1}$ save for any harmonic term with zeros at the sampling points." In this statement s is the transform variable and s_c is the sampling frequency. A simple filter that is

constant for $|s| < s_c$ and zero for $|s| > s_c$ will not modify the transform of the data. This type of filter is a square filter. The Fourier transform of a square filter is a sinc function. Thus, convolution of a sinc function with the data is mathematically equivalent to filtering the transform of the data with a square filter.

Since the bandpass of the detector was limited (ie. finite number of pixels) it was not possible to determine all frequencies equally well. This effect is compensated by damping the sinc function with a Gaussian. Damping localizes the interpolation and makes the interpolation insensitive to the size of the band pass. A damping constant of 3.75 was chosen to damp the sinc function to zero after 10 points on both sides of the peak of the function. A small improvement may be realized by rigorously deriving the damping constant from the known number of samples. The results were quite good so no attempt at optimization was made. The actual function used was

$$f(x-a) = \frac{\sin[\pi(x-a)]}{\pi(x-a)} \exp\left[\left(\frac{x-a}{3.75}\right)^2\right] \qquad (3)$$

where a is the amount of shift required. The re-sampled spectrum h(x-a) was obtained by convolving the measured spectrum, g(x), with the above function, ie.

$$h(x-a) = f(x-a) * g(x) \qquad (4)$$

where x is pixel value running from 1 to the total number of points in the spectrum. In the limit where a is zero (ie. no shift), f(x-0) is unity at x=0 and zero for all other values of x, thus returning the original function.

Using this approach all of the spectra were registered with respect to a reference spectrum (Figure 10). The optimum shift was determined by minimizing the noise in the ratio of the unknown spectrum and the reference. Figure 12 illustrates this procedure. When the two spectra are not registered the ratio tends to be very noisy due to the mismatch in the channel fringes while the telluric absorptions show a characteristic 'S' shape pattern. The shifts required ranged from no shift to two pixels, with the average shift being about 0.5 pixels.

This technique does not guarantee perfect cancellation of the telluric absorptions and channel fringes. The telluric features are only cancelled when the air mass is well matched and the atmospheric absorbers such as water vapor are constant throughout the night. Similarly, changes in seeing profiles during a night will prevent good cancellation of the interference fringes, because of the varying spectral resolution. The effects of these problems were minimized with frequent and periodic observations of comparison stars (cf. Table 1).

Relative Spectra

After the spectra were computed and registered with respect to the reference spectrum they could be averaged. For each night all of the Pluto spectra were averaged with equal weight. The comparison star average was constructed by using all of its available exposures from

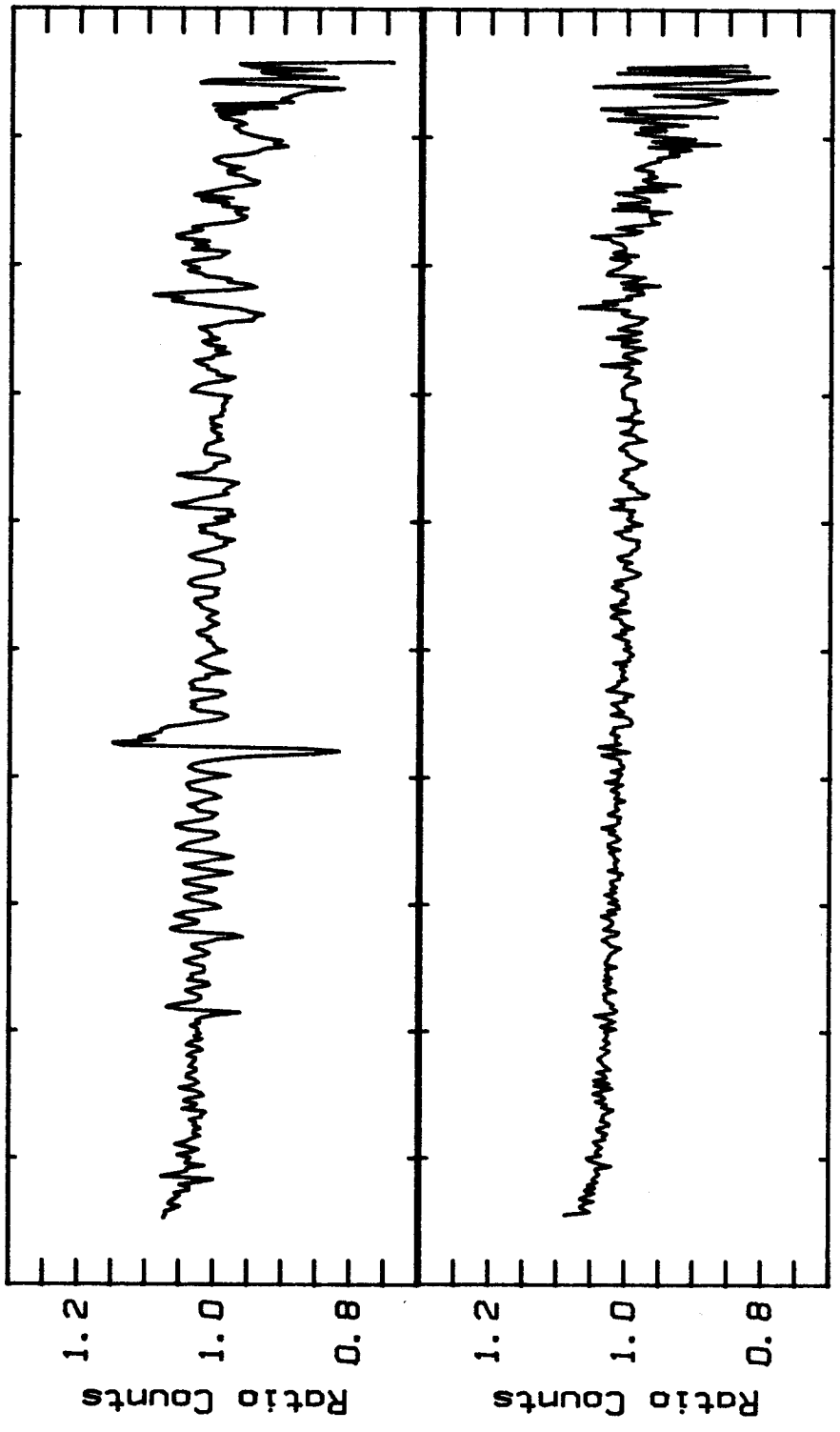

Figure 12 Effects of Shifting Data

Ratio of two different exposures of the same comparison star taken on the night of 23 April 1983 shown with no shifting on the top and a relative shift of 0.877 pixels on the bottom.

that night. If the resulting mean air mass was not identical to that of Pluto one or two comparison star spectra were removed from the average to make the match as close as possible. Figure 13 shows the average Pluto spectrum along with the matching spectrum of the comparison star for the night of 20 April 1983. The ratio, representing the relative spectrum of Pluto for that night, is displayed in Figure 14.

By averaging the spectra from all four nights a significant increase in the signal-to-noise ratio could be obtained over previous results. The grand average is illustrated in Figure 15 where the data from this investigation is compared to the previous spectrum by Fink et al., (1980). Both are plotted on a relative reflectance scale normalized to 1 at 6000 Å. The slight difference in slope is due to different comparison stars used for each observation set.

Atmospheric Extinction Coefficients

Absolute flux calibration of our spectra, described in the next section required knowledge of the atmospheric extinction coefficients. The frequent observations of the comparison star could be used for this purpose. At each point in the spectrum the number of counts recorded for the star was converted to a magnitude. The magnitude measured as a function of air mass was fitted to a linear extinction curve with the method of least squares (eg. Bevington, 1969). The slope obtained from the fit is the extinction coefficient in units of magnitude per air mass. The intercept is the zero air mass spectrum of the star and was not used. This type of plot is also known as a Langley plot. A

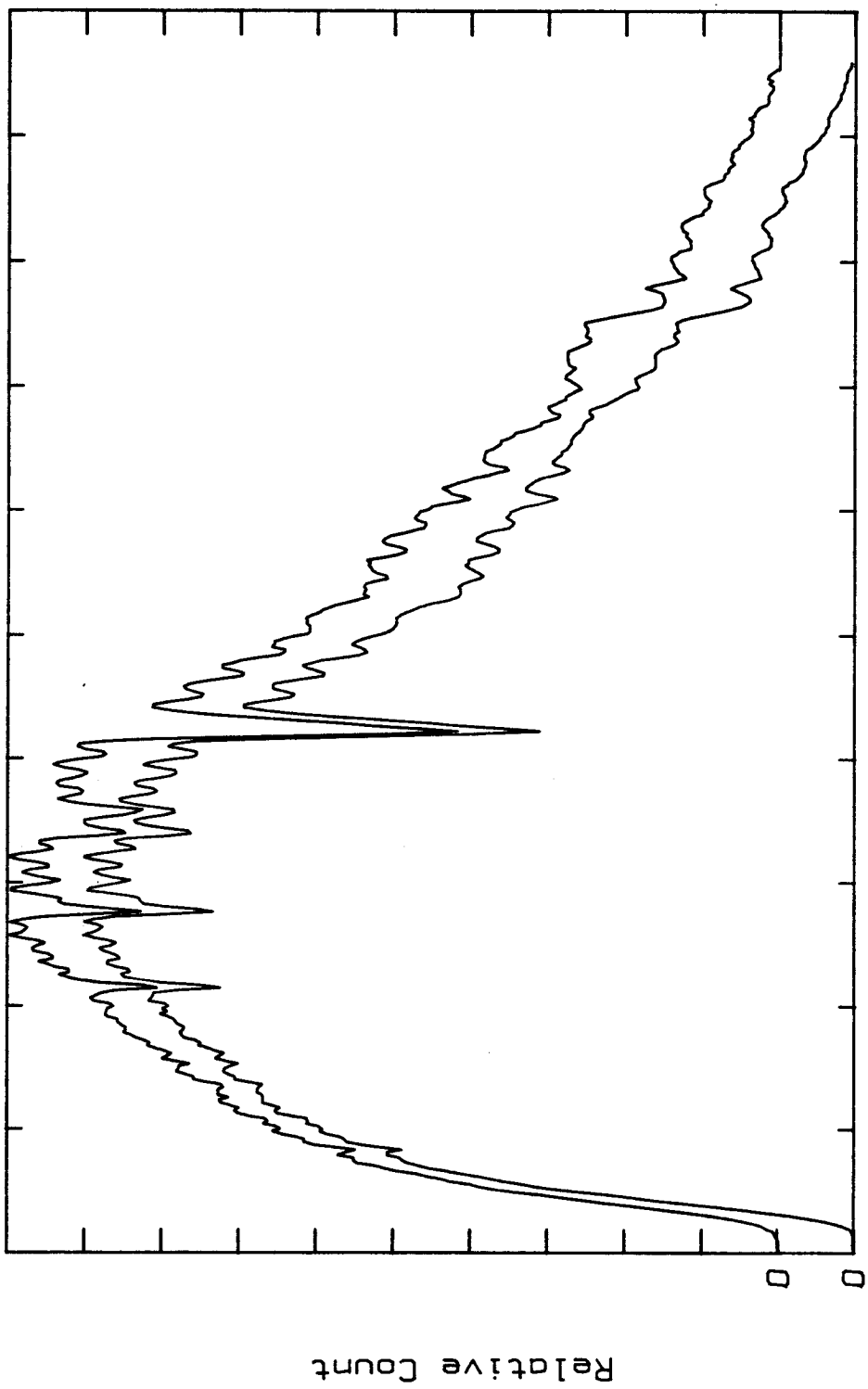

Figure 13 Pluto and Comparison Star Average Spectrum

Data from 20 April 1983 showing the Pluto average and the SAO 120312 average.
Mean Pluto air mass = 1.243. Mean SAO 120312 air mass = 1.249.

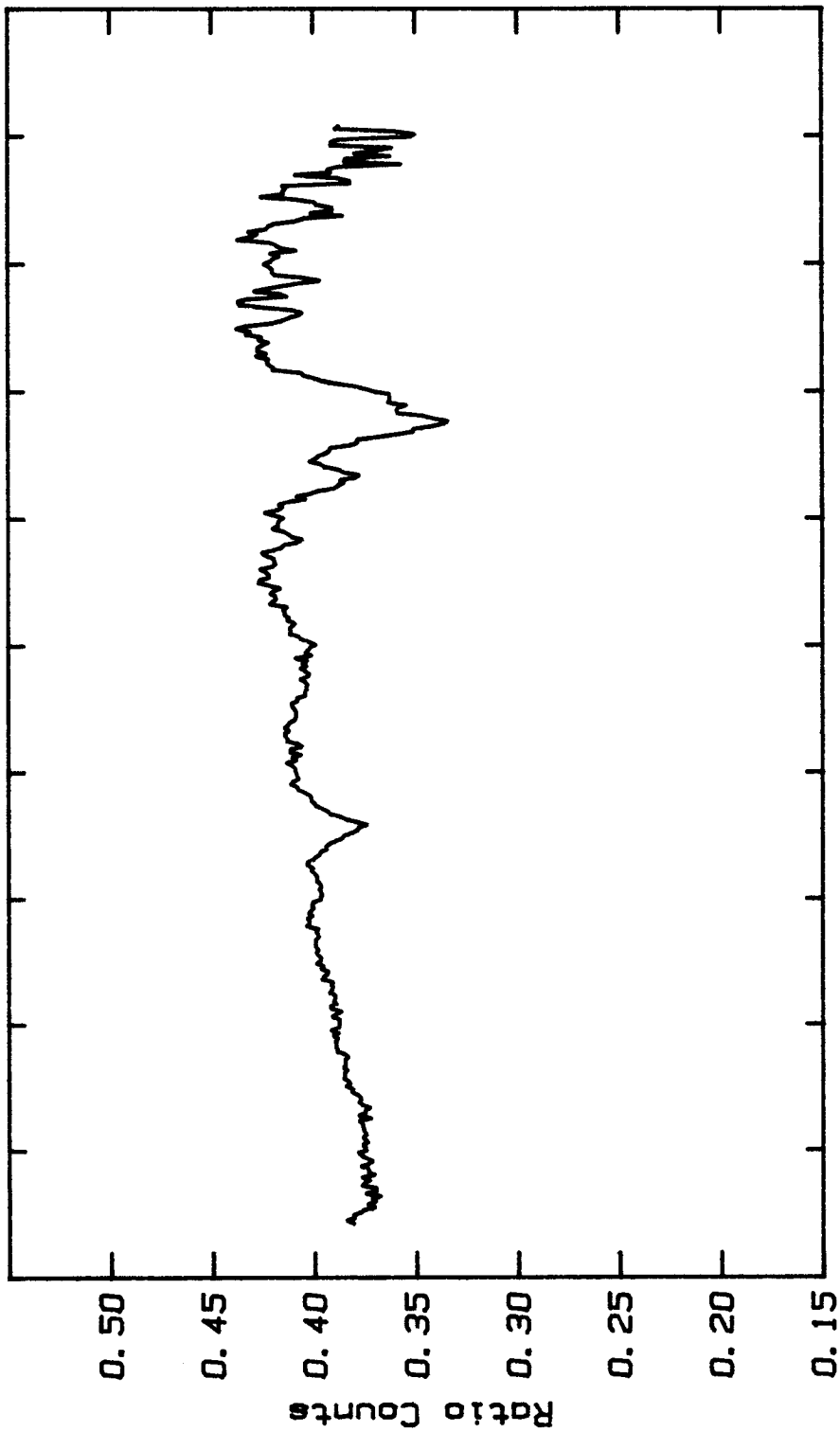

Figure 14 Relative Spectrum of Pluto

Ratio of the two averages shown in Figure 13. The vertical scale indicates the relative count level between the two spectra without correcting for different exposure times.

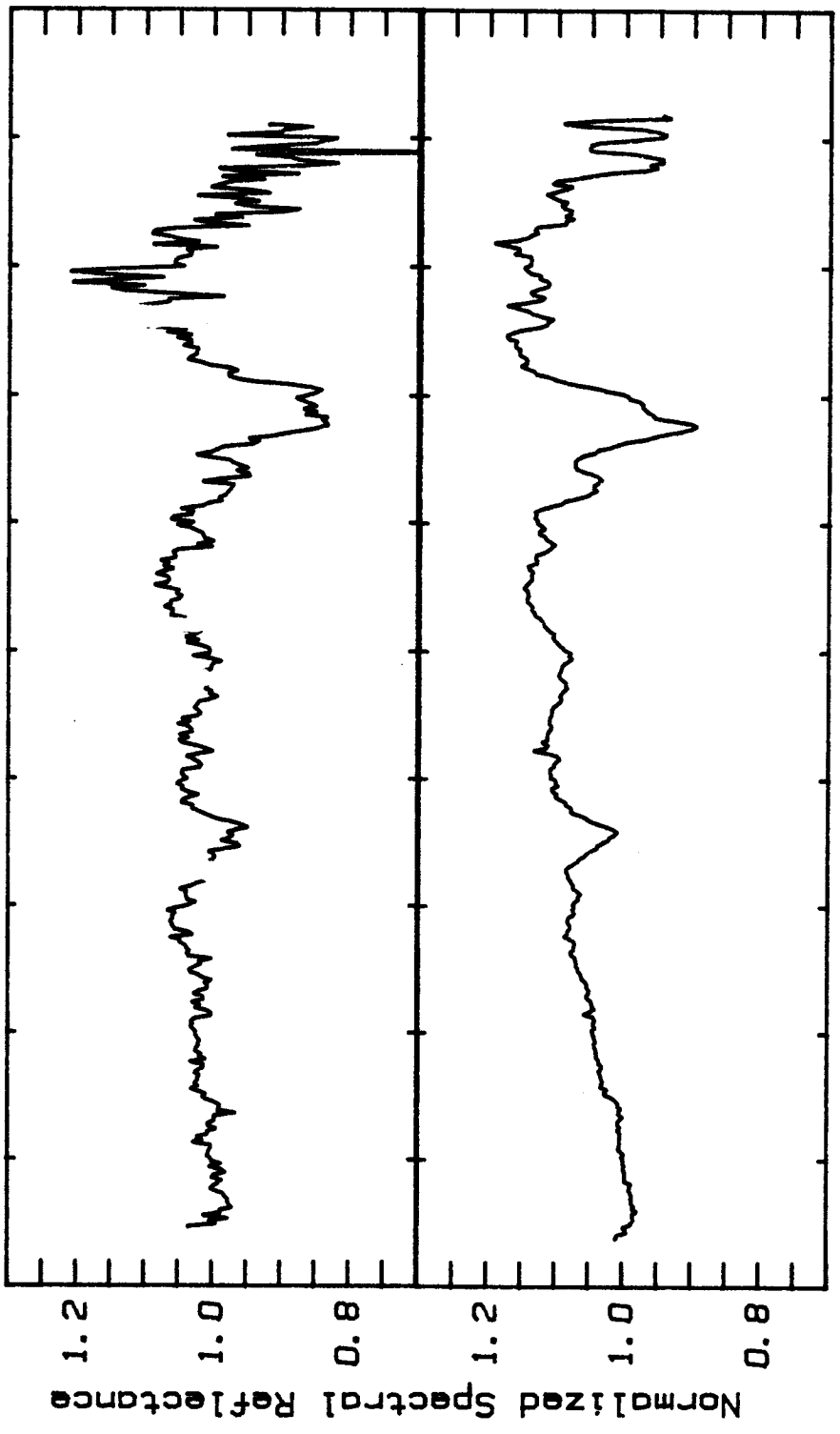

Figure 15 Grand Average Pluto Spectrum

Average of all four Pluto-SAO 120312 ratios for April 1983 compared with the data from Fink et al. (1980). The 1983 data represents 470 minutes of integration on Pluto while the 1980 data represents only 35 minutes.

computer program was written that used all of the comparison star exposures from a given night and determined the extinction coefficient at every wavelength. Figures 16, 17, 18, and 19 show the atmospheric extinction coefficients for each of the four observing nights. It can be seen that the procedure works quite well and results in a spectral plot of the atmospheric transmission at the resolution of the instrument. These figures are shown because there are few spectrally resolved extinction plots available.

While the variation in opacity caused by the changing amount of atmospheric water vapor from night to night is expected, the extinction at the short wavelength end of the spectrum is not readily explained. It is possible that this is due to varying amounts of volcanic dust from the eruption of El Chichon in 1982. A word of caution from this data seems in order about the use of "average" extinction coefficients for a given site. The figures demonstrate that for the best results the extinction must be determined every night.

Absolute Calibration

The final phase of the data reduction procedure involved determination of the absolute flux and geometric albedo for Pluto. Absolute calibration of the spectra for each individual night was carried out by observing the standard stars 109 Virgo and BS 6629 for which absolute flux levels have been published by Johnson (1980).

The absolute flux of the comparison star, SAO 120312, must first be determined. Since the ratios of comparison star/standard star and Pluto/SAO 120312 were smoothly varying, four points of the spectrum

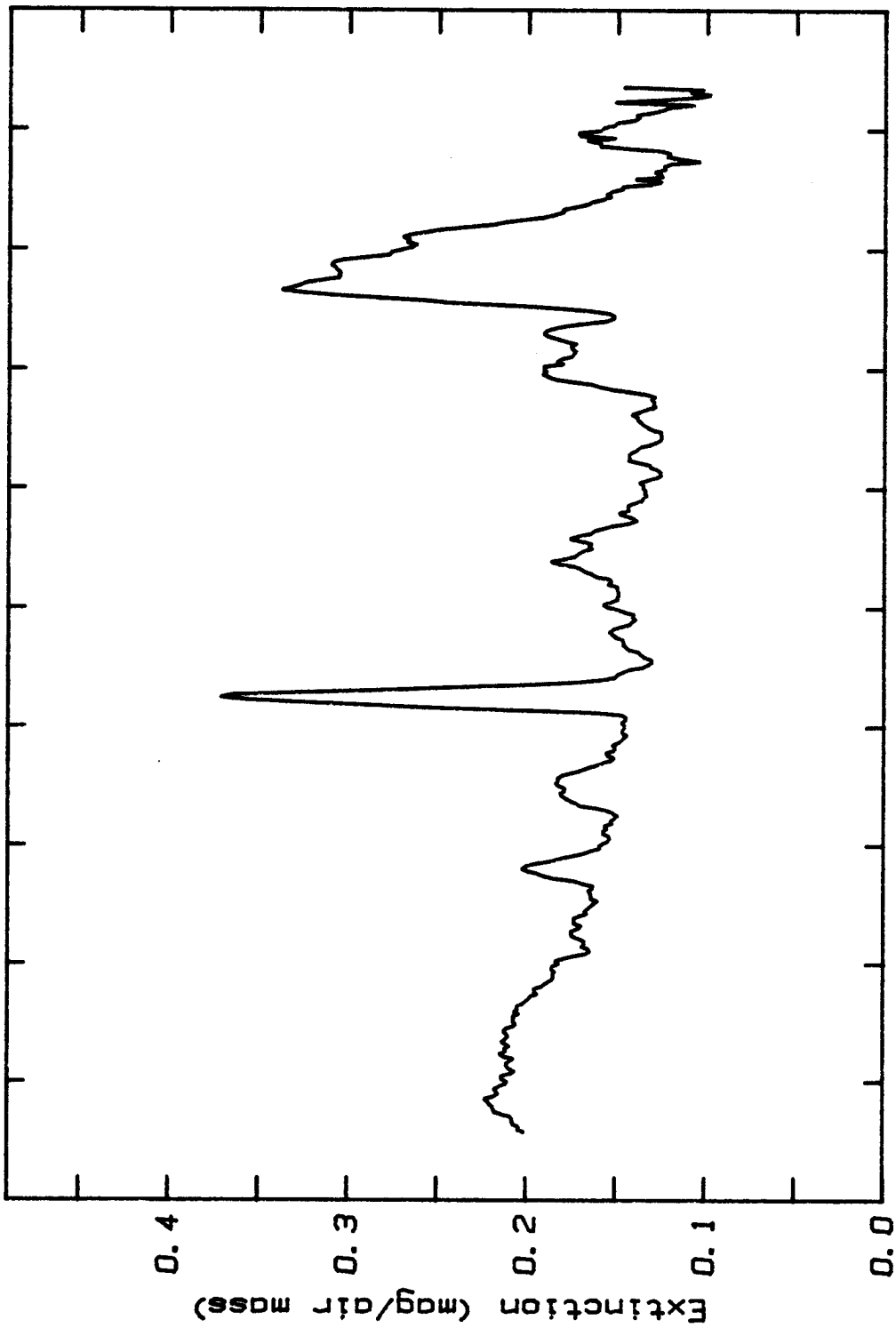

Figure 16 Extinction Curve for 18 Apr 1983

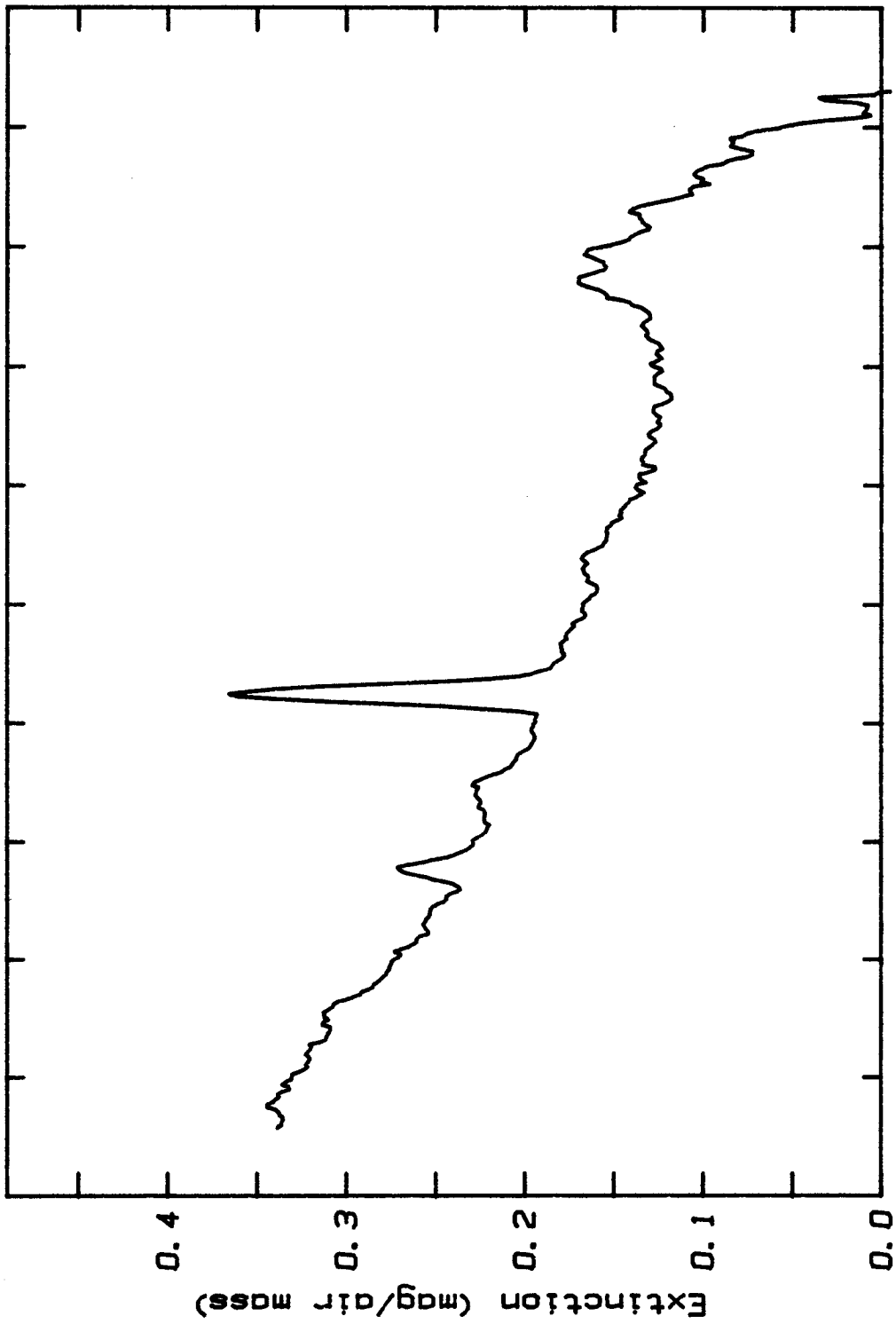

Figure 17 Extinction Curve for 19 Apr 1983

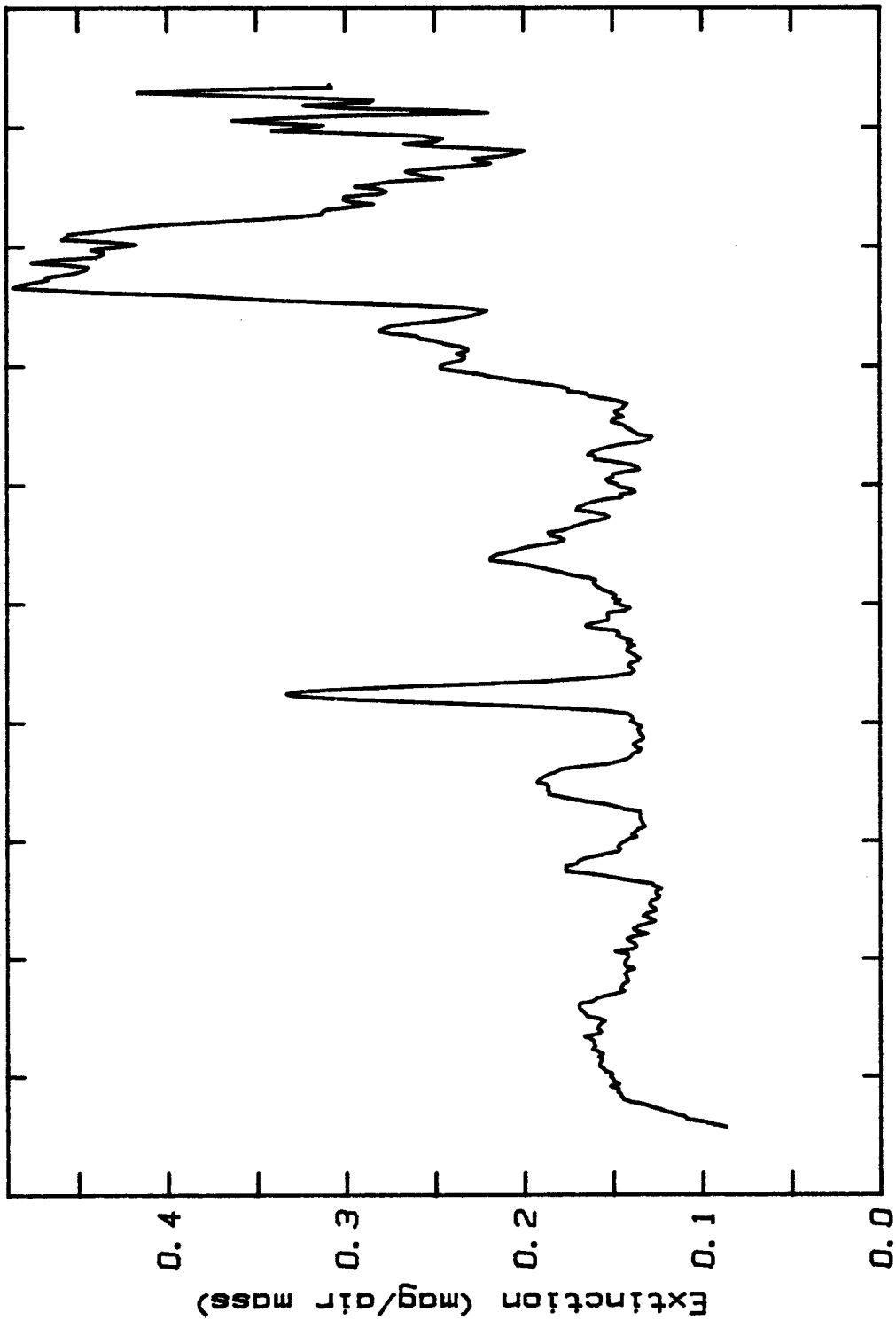

Figure 18 Extinction Curve for 20 Apr 1983

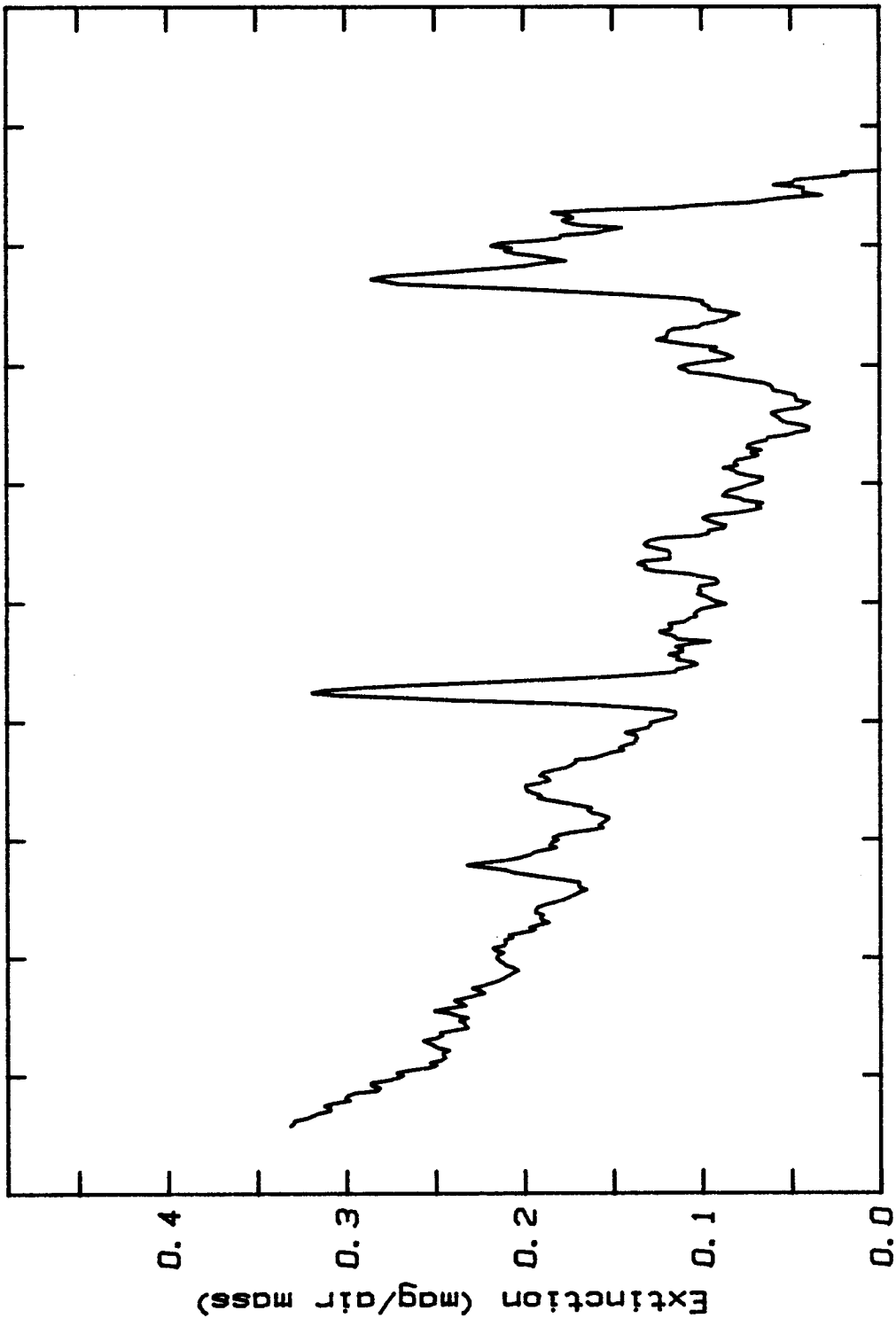

Figure 19 Extinction Curve for 23 Apr 1983

sufficed for calibration purposes. The points were carefully chosen to avoid telluric absorptions and methane features in Pluto's spectrum. At each wavelength the number of counts per second was determined from an average of 15 adjacent points in the spectrum.

The 10" entrance slit of the spectrometer was wide enough to admit all the light so that no correction for the light lost outside the slit was required (Johnson et al., 1984). Multiplying the measured count ratio by the absolute flux of the standard (Johnson, 1980) yielded the absolute flux of the comparison star. The air mass correction was then applied from the previously determined extinction coefficients. This correction was generally about 1% with the largest being 5%. For each night the absolute flux of the comparison star was calculated independently. For the final absolute flux determination of the star SAO 120312 the average was taken, and is shown at the bottom of Table 3. The sigma listed in Table 3 is the standard deviation of the mean from the seven mearurements.

Once the absolute flux of SAO 120312 was established the same procedure was used to determine the absolute flux of Pluto from its ratio to SAO 120312. No airmass correction was necessary since the air masses were matched before ratioing. Table 4 gives the absolute flux determination of Pluto for each of the four nights of observation.

As a check on the calibration, the absolute flux of Pluto was converted to broadband photometric magnitudes. The flux at the wavelength of 7000 Å was converted to an R magnitude using the zero magnitude flux of $I(0) = 1.76 \times 10^{-9}$ ergs/cm^2-s-Å (Johnson, 1965). Convolution with the R filter passband was not carried out. The R

Table 3

Absolute Calibration of SAO 120312

Flux (ergs cm-2 sec-1 Å-1)

DATE (UT)	STANDARD STAR	WAVELENGTH (ANGSTROMS) 6000	7000	8000	9500
18 APR 1983	109 Virgo	5.85(-13)	4.61(-13)	3.74(-13)	3.21(-13)
18 APR 1983	109 Virgo	5.84(-13)	4.60(-13)	3.68(-13)	3.12(-13)
19 APR 1983	109 Virgo	5.94(-13)	4.66(-13)	3.76(-13)	3.25(-13)
19 APR 1983	109 Virgo	5.69(-13)	4.54(-13)	3.64(-13)	3.07(-13)
20 APR 1983	109 Virgo	6.25(-13)	4.88(-13)	3.87(-13)	3.27(-13)
20 APR 1983	109 Virgo	6.05(-13)	4.82(-13)	3.89(-13)	3.39(-13)
23 APR 1983	BS 6629	5.52(-13)	4.48(-13)	3.67(-13)	2.87(-13)
AVERAGE		5.88(-13)	4.66(-13)	3.75(-13)	3.17(-13)
SIGMA		0.09(-13)	0.06(-13)	0.004(-13)	0.06(-13)

Note 1 The parentheses indicate the power of ten which is to be multiplied by the flux value.

Note 2 Pairs of values for a particular data refer to measurement before and after transit of the star.

Table 4

Absolute Calibration of Pluto

Flux (ergs cm-2 sec-1 Å-1)

DATE (UT)	PHASE	WAVELENGTH (ANGSTROMS) 6000	7000	8000	9500
18 APR 1983	0.19	1.04(-14)	8.87(-15)	7.21(-15)	6.33(-15)
19 APR 1983	0.35	1.05(-14)	8.93(-15)	7.31(-15)	6.51(-15)
20 APR 1983	0.48	1.10(-14)	9.27(-15)	7.60(-15)	6.64(-15)
23 APR 1983	0.98	9.14(-15)	7.83(-15)	6.52(-15)	5.78(-15)

magnitude can be converted to a B magnitude using the color indices for Pluto of B-V = 0.80 and V-R = 0.63 from Harris, (1961). Reducing the B magnitude to standard opposition for Pluto (r=39.5 AU, d=38.5 AU, and g=0 degrees) yields the four points shown in Figure 20 overlayed on the most recent absolute broadband B photometry by Tholen et al. (1985). The error bars are determined from the flux calibration of SAO 120312. The systematic shift of 0.07 magnitudes between the points and the lightcurve is typical in transforming one photometric system to another. It is probably due to the oversimplified conversion to an R flux magnitude and maybe due to the V-R color index.

Geometric Albedo vs. Rotational Phase

In order to derive the geometric albedo of Pluto it is necessary to divide by the solar flux incident on Pluto. An approximate method is to use a solar type comparison star whose flux spectrum is very nearly the same as that of the sun. The comparison star SAO 120312 is classified in the SAO catalog as a G5 star. From this it was expected that the ratio spectrum to this star would need only a small correction in slope to yield the geometric albedo directly. Upon comparing the absolute flux spectrum of SAO 120312 to that of the sun (Arvsen et al., 1969) it was found that the relative agreement was within the accuracy of our data, ie. about 1%. Therefore the geometric albedo of Pluto can be determined directly to within this error from the ratio spectrum.

Calibrating the ratio spectra of Pluto then requires determination of the geometric albedo at only one wavelength, which was

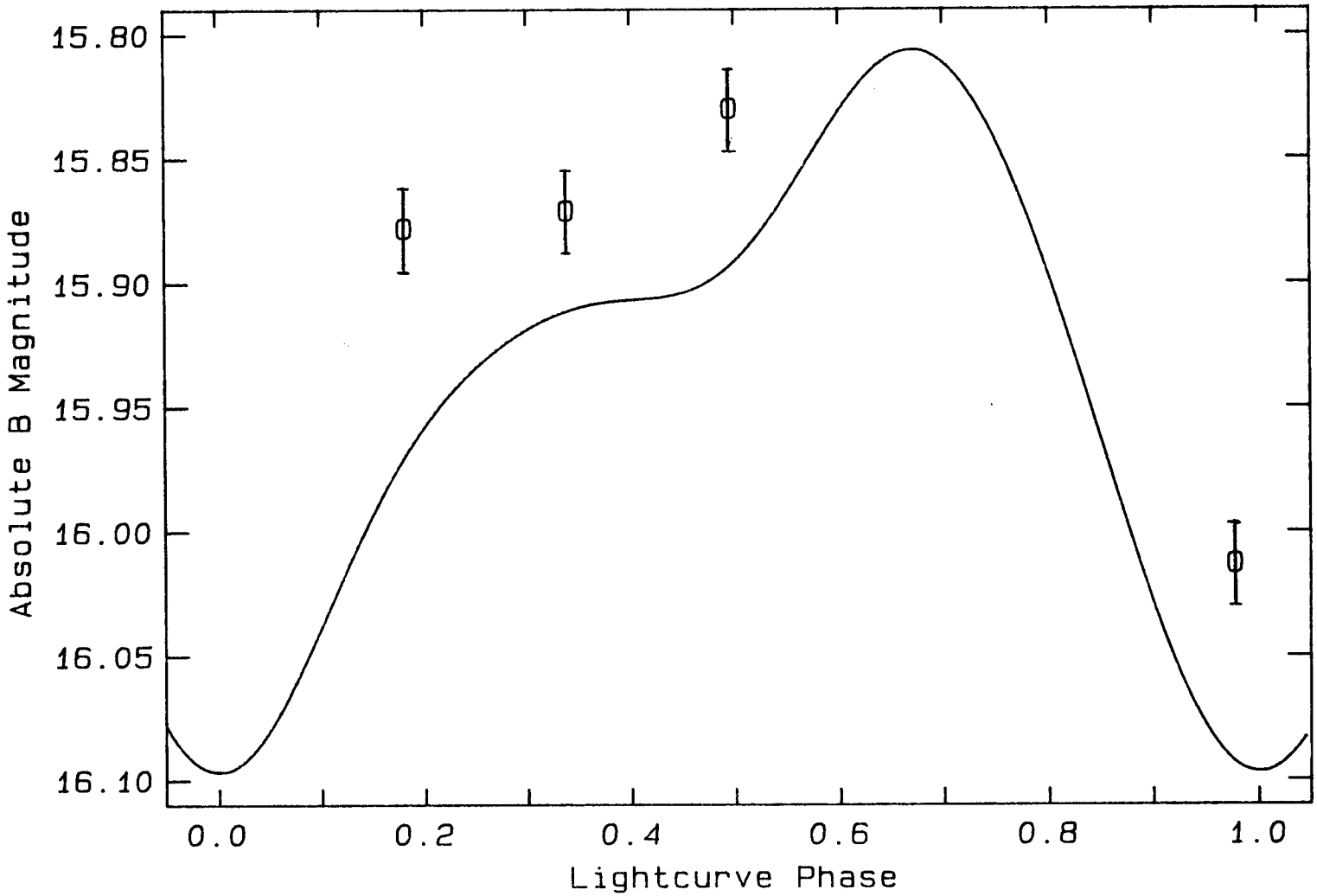

Figure 20 **Comparison of Absolute Calibration with Broadband Photometry**

The solid curve is the broadband lightcurve of Pluto from Tholen et al. (1985). The symbols indicate the equivalent B magnitudes derived from Table 4.

chosen to be 6000 Å. The formula for geometric albedo is

$$P = \frac{\pi F_\lambda r^2 d^2}{f_\lambda A} \qquad (5)$$

where

F is the flux from the object,

f is the flux from the sun at 1 AU,

r is the distance between observer and object in (cm),

d is the distance between object and sun in (AU), and

A is the cross sectional area of Pluto plus Charon.

It should be noted that the derived geometric albedo spectrum is for the Pluto-Charon system. The relative contribution of Charon to the total flux is not precisely known at the present time and may not be constant. The relative flux contributions of Charon will be taken into account in the modelling described in the Chapter 4. Table 5 contains a summary of physical parameters adopted for the Pluto-Charon system from various sources: Trafton and Stern, (1983); Hege et al., (1982); and Tholen et al., (1985). The flux assumed for the sun is from Arvsen et al., (1969). The values for r and d at the time of the observations are listed in Table 1. The cross sectional area of the system is determined from the radii for Pluto and Charon listed in Table 5. Applying these values to Equation (5) as well as Pluto's flux determined earlier (Table 5) yields the geometric albedo of the system at 6000 Å, and thus calibrates all of the Pluto/SAO 120312 ratio spectra on an absolute reflectance scale.

Table 5

Physical Parameters of Pluto and Charon

Pluto mass	M = 1.4(25) g
Pluto radius	R = 1500 km
Charon mass	m = 1.8(24) g
Charon radius	r = 750 km
Charon - Pluto separation	20,000 km
Pluto surface gravity	g = 41.5 cm s-2
Pluto - Charon density	ρ = 1 g cm-3
Charon orbital period	same as lightcurve
First minimum light in 1980	JD 2444240.661
Lighttime correction	0.167 days
Lightcurve period	6.38726 days
Phase coefficient	0.031 mag/degree

The uncertain quantities in the geometric albedo calibration are: 1) Flux of the sun (good to $\sim$3%), 2) Flux of Pluto-Charon (good to $\sim$3-4%), and 3) Area of Pluto and Charon (good to $\sim$50%). The uncertainties in r and d are negligible. The importance of the large uncertainty in the area of Pluto and Charon is lessened by including the radii in the model calculation.

The final observational results of this investigation are displayed in Figures 21, 22, 23, and 24. The figures show the geometric albedo spectrum of Pluto for rotational phases 0.19, 0.35, 0.49, and 0.98 respectively. The vertical scale for all of the figures is the same allowing intercomparison of the changes in the overall brightness as a function of the rotational phase. The range of geometric albedo displayed was chosen to exhibit both the spectral features and the noise level on a reasonable scale.

On all of the spectra the channel fringes are well cancelled so that the spectrum shifts were carried out properly. Two spectra (Figures 23 and 24) have no residual telluric absorptions. The other two (Figures 21 and 22) exhibit slightly imperfect cancellation of the telluric absorptions. The lack of perfect cancellation was due to changing atmospheric conditions during the two nights.

Methane absorption bands at 6200, 7200, 7900, 8400, 8600, 8900, and 10000 Å are clearly evident in all the spectra. It can be easily seen on the spectra for phases 0.49 and 0.98 (Figures 23 and 24) that the depths of the methane absorption features has changed. The overall brightness differences for the various phases, as expected from the lightcurve, is also clearly demonstrated.

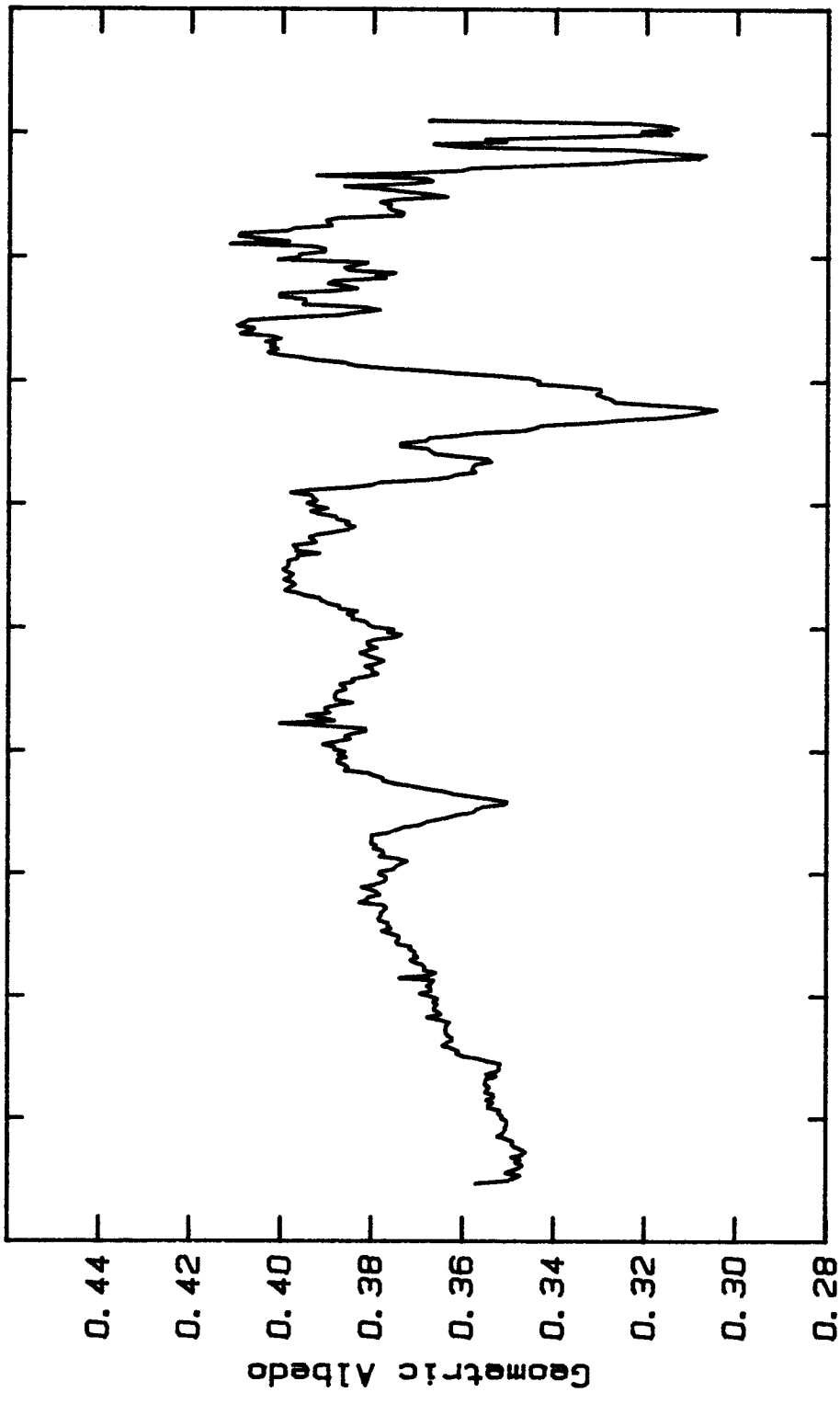

Figure 21 Geometric Albedo of Pluto-Charon, 18 Apr 1983

Final results of the data reductions for phase 0.19. Figures 21-24 are all plotted with the same vertical scale.

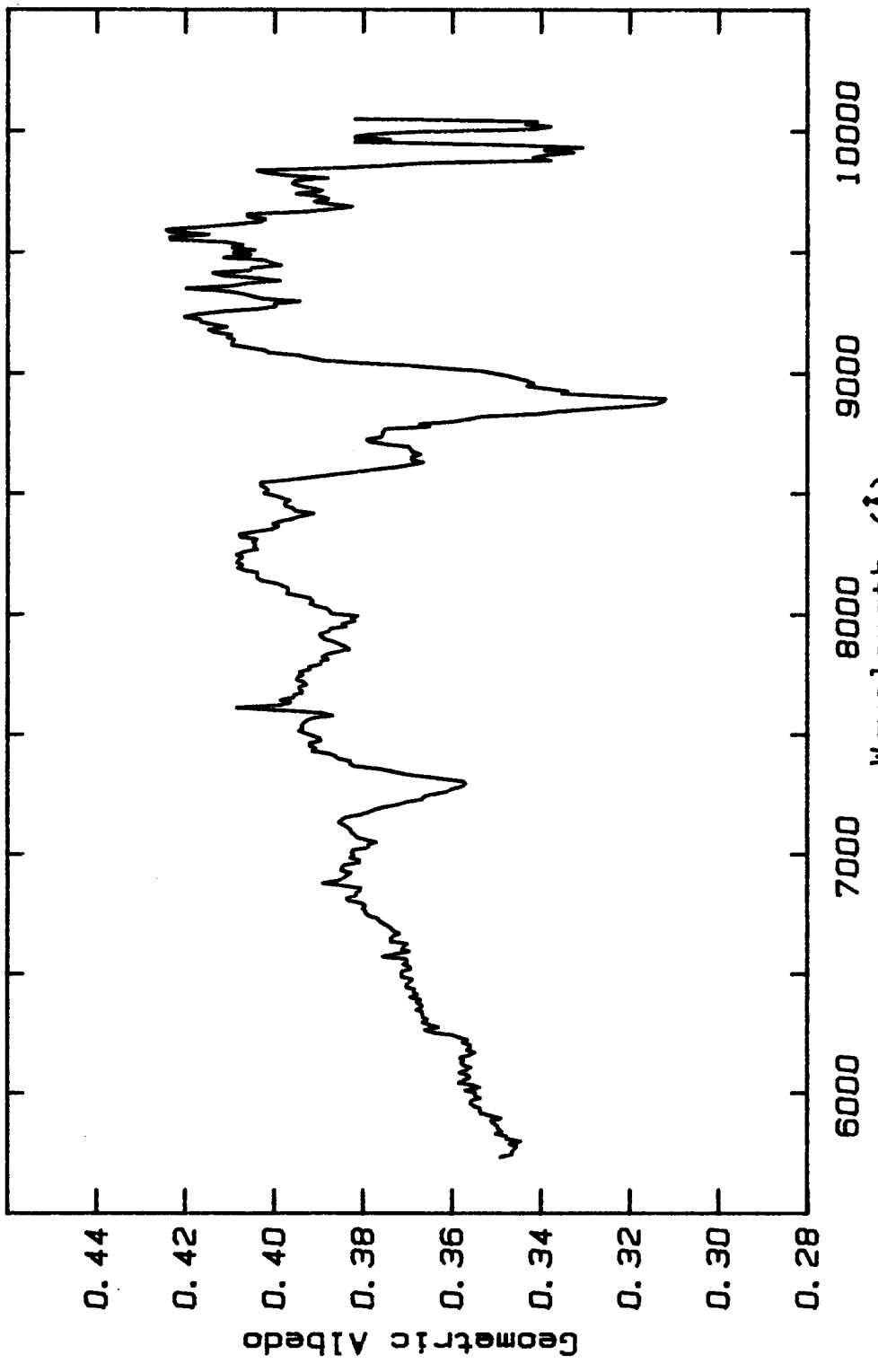

Figure 22 Geometric Albedo of Pluto-Charon, 19 Apr 1983

Final results of the data reductions for phase 0.35.

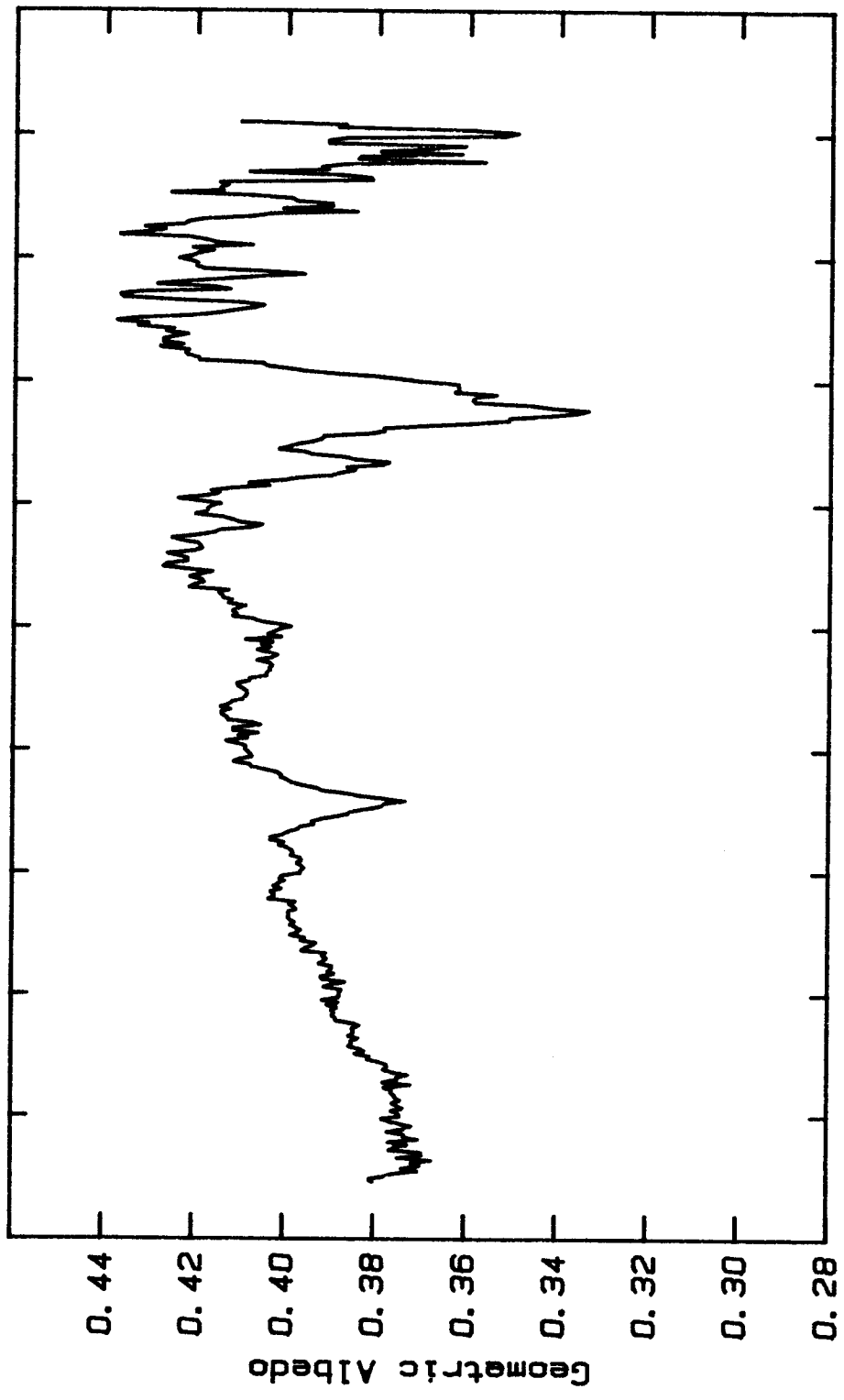

Figure 23 Geometric Albedo of Pluto-Charon, 20 Apr 1983

Final results of the data reductions for phase 0.49.

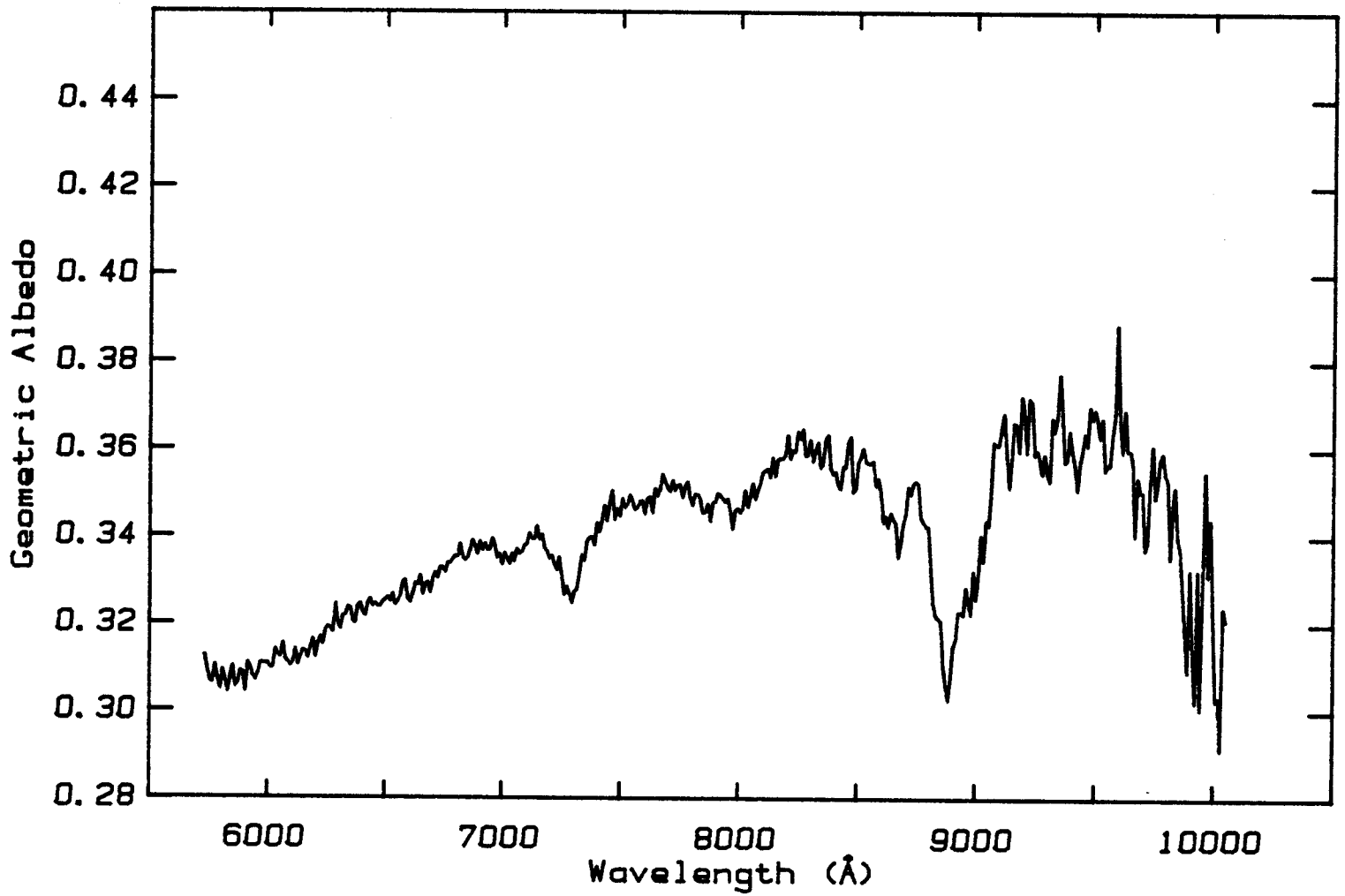

Figure 24 Geometric Albedo of Pluto-Charon, 23 Apr 1983

Final results of the data reductions for phase 0.98.

The 10000 Å feature is noisy because it appears at the edge of sensitivity of the instrument and is not clearly defined, but definitely seems to be present. The 8900 Å band is the strongest throughout the spectrum and is nicely shown. Appearing next to this band are two shoulders at 8400 and 8600 Å. At 7900 Å is a weak and shallow band which is very useful for fitting the column abundance of the atmosphere and constraining the frost model. A very well defined band with a good signal-to-noise ratio is located at 7200 Å. The band is not too strong, but strong enough that it is slightly saturated. Nevertheless, it is the main band used for subsequent model analyses. The weakest feature, at 6200 Å, is not seen clearly on all phases, but seems to be definitely present. On no spectra is this feature as strong as seen in the spectra from Fink et al. (1980). The next chapter is devoted to modeling the observed spectra and their behavior as a function of rotational phase.

CHAPTER 4

MODEL ANALYSIS

The data presented at the end of Chapter 3 provide a substantial amount of spectroscopic information which can be used in trying to understand more about the atmospheric and surface properties of Pluto. The observed phase variation of the methane bands provides a new constraint on descriptions of Pluto. The model presented here contains three components: methane frost, methane gas, and a surface with albedo variations.

Discussion

Explaining the observed spectrum depends upon the behavior of methane frost and methane gas under conditions likely to exist on Pluto. A synthetic match to the Pluto spectrum has already been published for methane gas (Fink et al., 1980) but little has been done for methane frost.

The data in Figures 21-24 clearly show that the depths of the methane features are dependent on rotational phase. Every band of methane observed was weakest at the phase corresponding to minimum light (0.98). There was a perceptible change even between the phases of 0.35 and 0.49. For a uniform amount of gaseous methane the total amount of absorption would remain constant with rotational phase except for some variation expected for an inhomogenous surface because the

albedo pattern will change the column abundance averaged over the disk. If the center of the disk is darker than the area near the limb, the high air mass regions are weighted more in the average. The absorption depth would be larger for this case than for a uniform sphere. If Pluto's lightcurve minimum is caused by a dark spot on the center of the disk then the absorption due to the gas would be greatest at minimum light. This is opposite to what is observed. Thus the data present evidence that a fraction of the methane absorption observed is due to a surface frost layer which is non-uniformly distributed over the surface of Pluto.

Photometric Spot Model

The photometric light curve of Pluto has been measured for nearly 30 years (Walker and Hardie, 1955). Since this time continued photometry has shown that Pluto's brightness at all rotational phases has been decreasing, but that and the lightcurve amplitude has been increasing with time; Hardie (1965), Kiladze (1967), Andersson and Fix (1973), Neff et al. (1974), Lane et al. (1976), Tedesco and Tholen (1980), Binzel and Mulholland (1983), and Tholen and Tedesco (1985). The changing amplitude has been attributed to a large obliquity of the rotational axis (Andersson and Fix, 1973). This has since been supported by the discovery of the satellite, Charon, by Christy et al. (1978). The changing amplitude and the shape of the lightcurve can be explained with two fixed dark spots on the surface of Pluto. However, two spots cannot explain the 0.35 magnitude drop in mean light since 1955 (Marcialis, 1983). This dimming can be explained by a more

complicated surface albedo distribution, including polar caps or bands. It can also be explained by physical changes of Pluto's surface properties such as the evaporation of ices, which can be caused by Pluto's changing distance from the sun.

From these considerations the oversimplified two spot model cannot be expected to lead to a unique interpretation of the spectroscopic data. Nonetheless it is a physically reasonable model which can be used to constrain two different types of terrain with different optical properties.

A two spot model has been developed by Marcialis (1983). This spot model explains the lightcurve of Pluto using two dark circular spots on the surface (46 and 28 degrees in radius, both at latitude -23 degrees, separated by 134 degrees in longitude). Photometric data from 1953 to 1982 was used to constrain the placement of the spots. In deriving these parameters the model assumed linear limb darkening with a limb darkening coefficient of 0.5 (eg. Russel and Merrill, 1952) and a contrast ratio between bright and dark regions of 2:1. Charon was assumed to contribute 20% of the flux that would be seen from the system without adding spots to the surface of Pluto.

The latitude of the sub-Earth point (i) on Pluto is given as a function of time by:

$$j_o = -19°,$$

$$j = j_o + 2.^{\circ}2\ T + 0.^{\circ}005\ T^2, \text{ and} \qquad (6)$$

$$i = j - 1.^{\circ}8\ \cos[2\pi(t-0.6)]$$

where

j_o is the latitude of the sub-solar point at the reference epoch of 1980.0,

T is the time in years since the reference epoch,

t is the fraction of the year, and

j is the latitude of the sub-solar point at time T.

Marcialis used a slightly different value for j_o (-16 degrees). This will have a small effect on the locations and the sizes of the spots but for the purposes of this study the change in j_o is not important. Note that the direction of Pluto's north pole has been defined in accord with the right hand rule for spin vectors in physics (ie. choice c. from Davies et al., 1980, page 215; which is different from the adopted convention). This places the current sub-Earth point south of Pluto's equator and approaching its equator at about 2.2 degrees per year.

The two spot model gives a plausible description of the variation in observed brightness of Pluto as it rotates. Figure 25 is

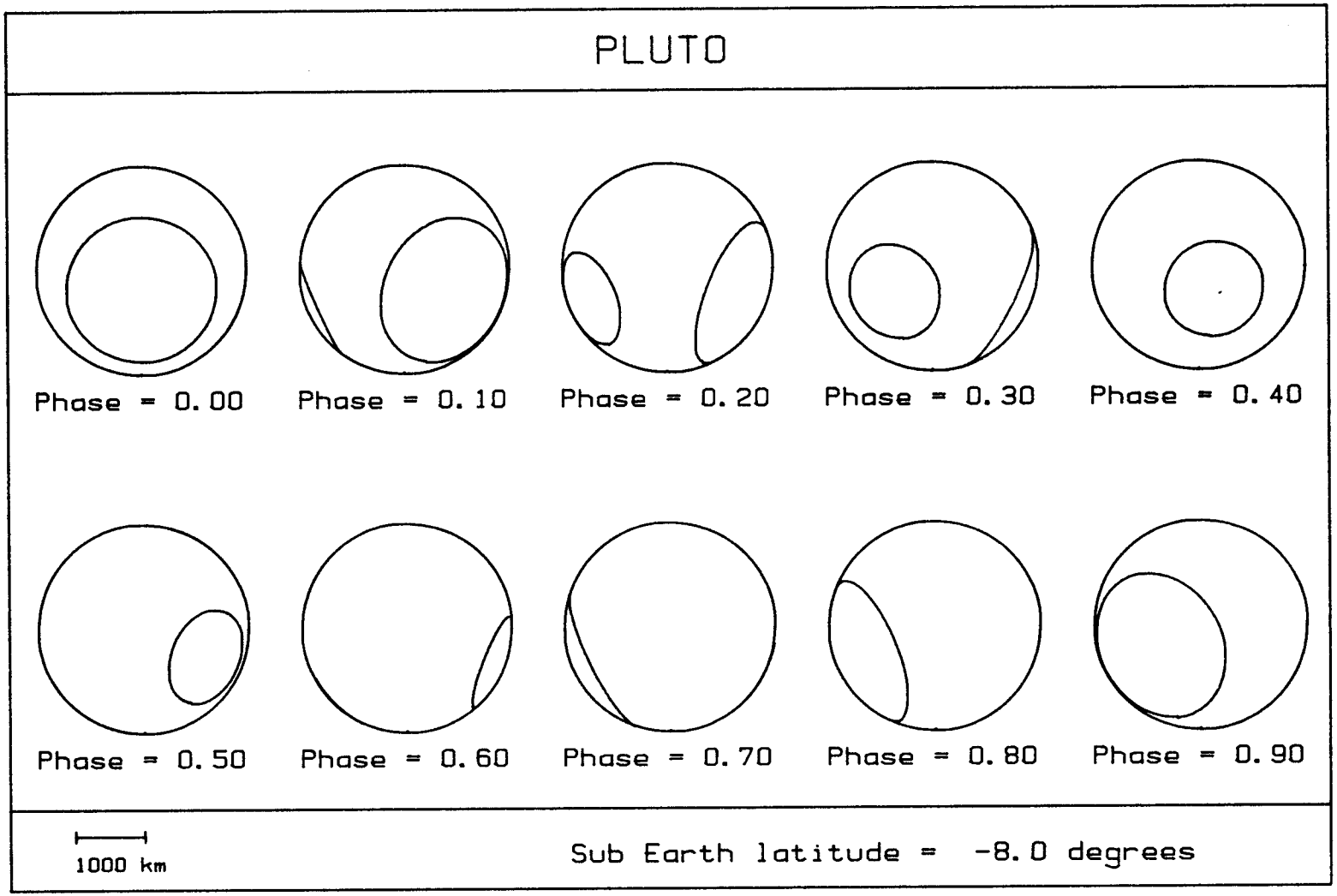

Figure 25 Spots on Pluto

A projected view of Pluto as it rotates from left to right. North is up.

a sequence representing the predicted appearance of Pluto for April 1983 as it rotates. The only parameters used from the two spot model were the sizes and locations of the spots. The contrast ratio and limb darkening are determined in the current treatment. The spots were used to constrain the distribution of the material on Pluto.

Synthetic Frost Calculations

Calculating the reflected light from a scattering and absorbing particulate surface is not a simple calculation. The target material on Pluto's surface is assumed to be methane frost. Such a frost would be expected to be made up of particles with a high single scattering albedo. For the single scattering case, discussed by Fink et al. (1980), the band depth ratios are very much different from the observed spectrum. If the strong features are matched the weak features show essentially no absorption. Multiple scattering acts to enhance the weak features more than the strong ones. Since the particles have a lower absorption coefficient in the weaker bands they will incur more scattering events, enhancing their absorption relative to the stronger bands.

A rigorous solution to the general scattering problem of a closely packed surface frost with arbitrary particle shapes has not been worked out yet. A recent paper by Hapke (1981), hereafter referred to as the Hapke Theory, details an approach for the approximate calculation of a spectrum for multiply scattering, close packed surface particles given sufficient knowledge of the composition.

For a detailed description of all of the assumptions refer to the paper (Hapke, 1981).

Physically the Hapke Theory is based on the equation for radiative transfer in a well dispersed medium without imbedded light sources. The transfer equation can be separated into a singly and a multiply scattered component. The single scattering part is solved using an average phase function for the particles. To simplify finding a solution an approximate form of the Chandrasekhar H function is used (see following description). The multiply scattered light is treated by isotropic scattering. This was found to be a reasonable approximation because multiple scattering averages out directionality.

Extending the treatment to a close packed material requires including three effects: 1) The far-field approximation is no longer valid (particles are touching), 2) shadowing occurs, causing an increased backscattered intensity, and 3) diffraction ceases to be important. Coherent interference patterns between the particles is expected since the spacing between particles is of the same order as the size of the particles. This is not important if the surface particles are not arranged in a regular lattice structure. An average over a small region of the surface should average out the effects of coherent interference. The random nature of a particulate surface will also average out shadowing. In the Hapke Theory the effect of 2) is accounted for by the addition of a backscatter function (Hapke, 1963) as a small correction to the singly scattered radiation. The backscatter function depends in part on how the surface particles are packed. It is critical only if the scattering behavior for varying

solar phase angles needs to be explained. This is not a concern in the present investigation. Thirdly, the contribution of diffraction to the scattering efficiency is removed. This is justified because the diffraction patterns from the closely spaced particles will overlap, causing the diffracted light to be indistiguishable from the unscattered incident light.

The first step in the Hapke model calculation is to determine the average single scattering albedo from the physical properties of a material such as complex index of refraction and particle size. For a surface which consists of closely spaced, irregularly shaped large particles of one material the average single scattering albedo is equal to the total scattering efficiency. Scattering from internal and external surfaces of a particle is treated in terms of an effective particle size. The effective diameter of a particle is given by

$$D_e = \frac{2}{3} \frac{1-S_E}{1-S_I} D, \tag{7}$$

where D is the diameter of the particle and S_E and S_I are the external and internal scattering coefficients. These two parameters depend only upon the real part of the index of refraction. The values for methane with n_r=1.33, (Marcoux, 1969) turn out to be S_E=0.06 and S_I=0.47. The real part of the index of refraction is assumed to be constant from 5000 to 10000 Å. Thus the effective diameter is 1.18D for methane.

The formula for geometric albedo from the Hapke Theory is

$$A_p = \frac{1}{4}\int_0^1 w\, H^2(\mu)\, \mu d\mu + \frac{1}{4}\int_0^1 w\, [(1+B_o)P(0)-1]\mu d\mu, \qquad (8)$$

where

A_p is the geometric albedo,

w is the average single scattering albedo,

μ is the cosine of the angle of emergence (and incidence),

$H(\mu)$ is the Chandrasekhar H function,

B_o is the backscatter function, and

$P(0)$ is the average phase function of the particles for a phase angle of zero.

A useful approximation to $H(\mu)$ is also given and has the form

$$H(\mu) = \frac{2}{1+\gamma}\ [1 + r_o\ (\mu-0.5)], \qquad (9)$$

Other formulas needed to evaluate Equations (8) and (9) are

$$
\begin{aligned}
w &= (1+\tau)^{-1}, \\
\tau &= \alpha D_e, \\
\alpha &= \frac{4\pi n_i}{\lambda}, \\
B_o &\simeq \exp[-\tfrac{1}{2} w^2], \\
\gamma &= (1-w)^{1/2}, \text{ and} \\
\Gamma_o &= \frac{1-\gamma}{1+\gamma}
\end{aligned}
\tag{10}
$$

where

τ is the optical depth across the particle,

n_i is the imaginary index of refraction,

λ is the wavelength of light, and

α is the absorption coefficient.

The imaginary index of refraction can be calculated from the absorption coefficient for the particles as a function of wavelength. Imaginary indices are not available for solid methane. Optical depths for liquid methane have been reported by Ramaprasad et al. (1978). These were converted to imaginary indices. Due to the weak intermolecular bonding in the methane solid it is expected that the difference between the solid and the liquid indices will be small. The value determined for the liquid will therefore be used in the subsequent analyses.

For a given particle size the scattering albedo and thus $H(\mu)$ and the value of the backscatter function, B_o is now determined. One further parameter needs to be specified: the phase function. This function depends on the average particle shape and is not known a priori, but does not affect the results very strongly (see discussion below).

The geometric albedo as a function of wavelength can now be calculated leaving only the particle size as a free parameter. The conditions under which Equation (8) is valid are: 1) particle size must be much larger than the wavelength of light, 2) particles are closely spaced, 3) particles are irregularly shaped, and 4) a surface integration element consists of a homogeneous mixture of a single type of particle.

To understand the application of Equation (8) to Pluto it is useful to first investigate a uniformly covered sphere of methane ice. In the case of a uniform planet the expression can be integrated and reduces to

$$A_p = \frac{r_o}{2} + \frac{r_o^2}{6} + \frac{r_o^3}{24} + \frac{w}{8}\left[P(0)(1+B_o)-1\right] \qquad (11)$$

Figure 26 shows a family of curves for different particle sizes. The top curve is a continuum reference level drawn through all of the bands. The absorption features are seen to deepen with increasing particle size. The appearance of the methane features in the synthetic spectrum is quite similar to that of the observed spectrum.

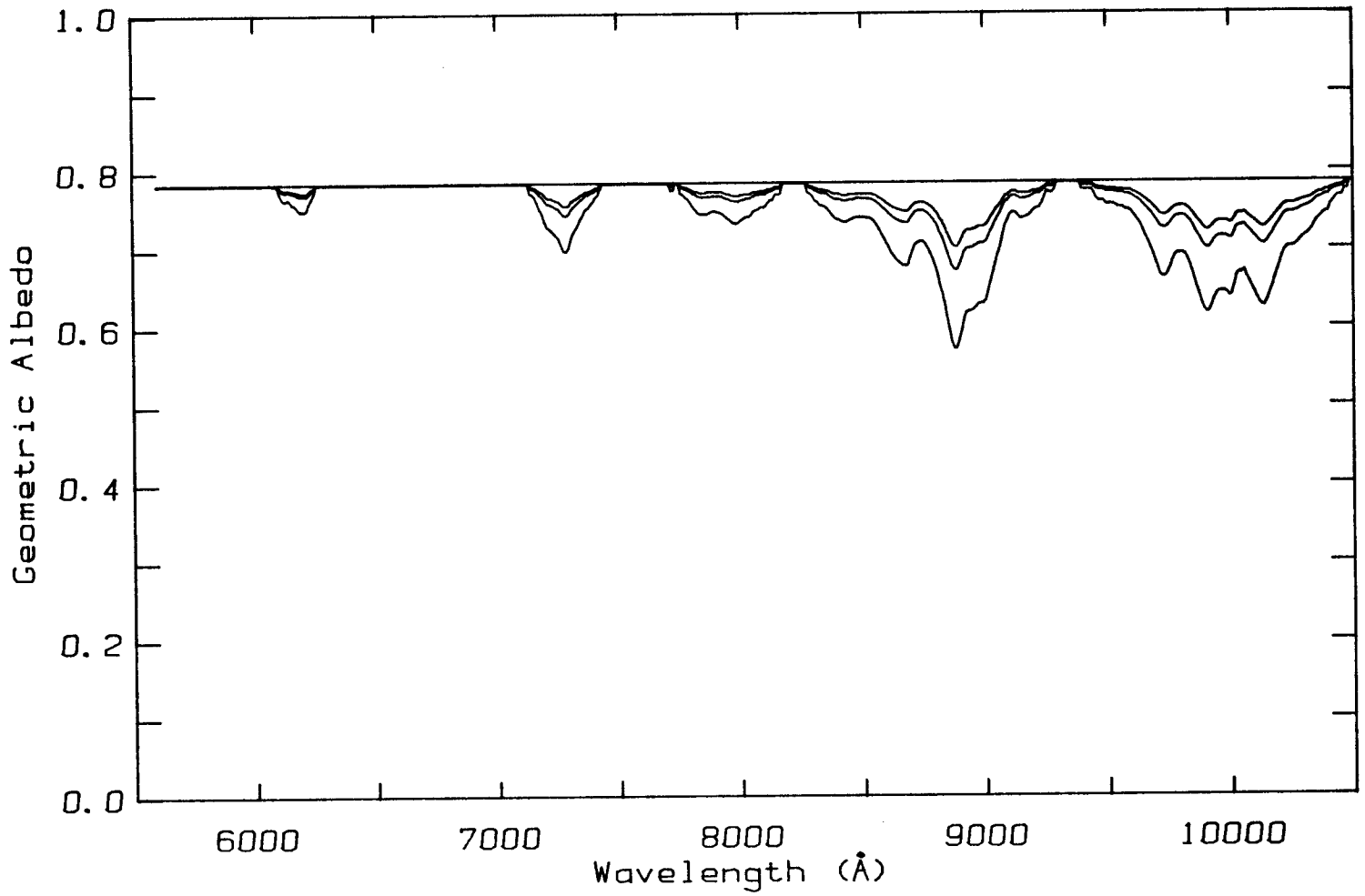

Figure 26 **Variation in Methane Frost Spectrum with Particle Size**

The straight line represents a continuum reference level. The next three curves are for particle sizes of 200, 400, and 1000 microns in order of increasing absorption strength. P(0)=1 for all curves.

The dependence of the synthetic spectrum on P(0) is explored in Figure 27. The depth of the absorptions is not seen to be critically dependent on P(0). Laboratory measurements of cobalt glass powders give a range of P(0) between 0.6 and 1.7 (Hapke and Wells, 1981). The actual value for methane is not known but its value is probably not much different from the isotropic case of P(0) used in Figure 26. Throughout the rest of the analyses this case is therfore assumed.

Using the absorption coefficients of Ramaprasad for methane it is not possible to match the observed wavelength variation of Pluto's continuum. The continuum is the portion of the reflected light which is not affected by methane absorption features. Material having a wavelength dependent absorption coefficient must be added in order to obtain a match. An easy way to fit the observed spectrum is to modify the equation for optical depth shown in Equation (10). The new equation becomes

$$\tau(\lambda) = \alpha(\lambda)\, D_e + \tau_o(\lambda), \qquad (12)$$

where the first term represents the opacity due to methane and the last term is the optical depth due to other absorbing material in the particle. The latter can be considered as the continuum optical depth. This treatment has the advantage that τ_o can be determined independent of the particle size thus separating the task of fitting the continuum albedo and the depths of the methane bands.

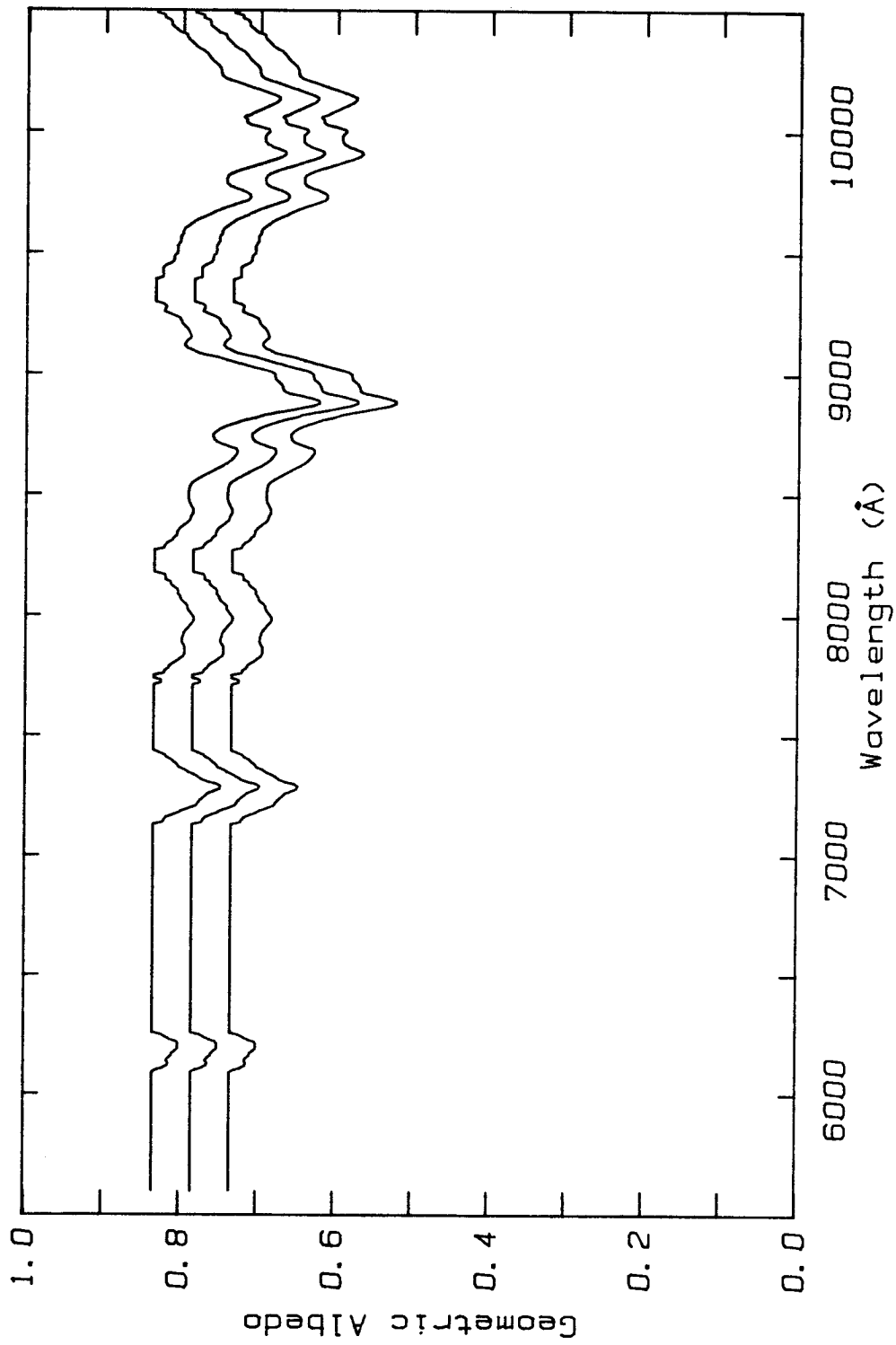

Figure 27 Variation in Methane Frost Spectrum with Phase Function

The three curves are for 1000 micron particle size and P(0) equal to 1.25, 1, and 0.75 for the top, middle, and bottom, respectively.

The effect of using different τ_o's that have no wavelength dependence is illustrated in Figure 28. This τ_o parameter can clearly control the continuum albedo in the synthetic spectrum. It can also wash out the absorptions due to the methane. For wavelengths that have a methane optical depth much larger than the continuum optical depth the geometric albedo is not greatly affected. When the methane optical depth is comparable to or less than τ_o the resulting geometric albedo becomes strongly dependent on τ_o.

The calcualation of the complete model requires addition of the spots and the numerical evaluation of the integral in Equation (8). The model now contains four parameters that must be specified: the particle size and τ_o for the area within the spots and for the area outside of the spot boundaries. The surface is broken up into annuli about the center of the apparent disk. The contribution to the integral for each annulus is the weighted average of the integrand evaluated for each terrain type. The weights are equal to the fraction of the annulus covered by each type. The integral is evaluated using the gaussian quadrature mesh points tabulated in Stroud and Secrest (1966) for a 40 point sum.

The spectra presented at the end of Chapter 3 represent the geometric albedo of the Pluto-Charon system. The model must therefore include the reflected light from Charon. This was modelled by assuming Charon to be a uniform sphere with no methane on its surface. Thus the geometric albedo of Charon is determined by Equation (11) where the optical depth used is τ_o. This adds a fifth free parameter to the model.

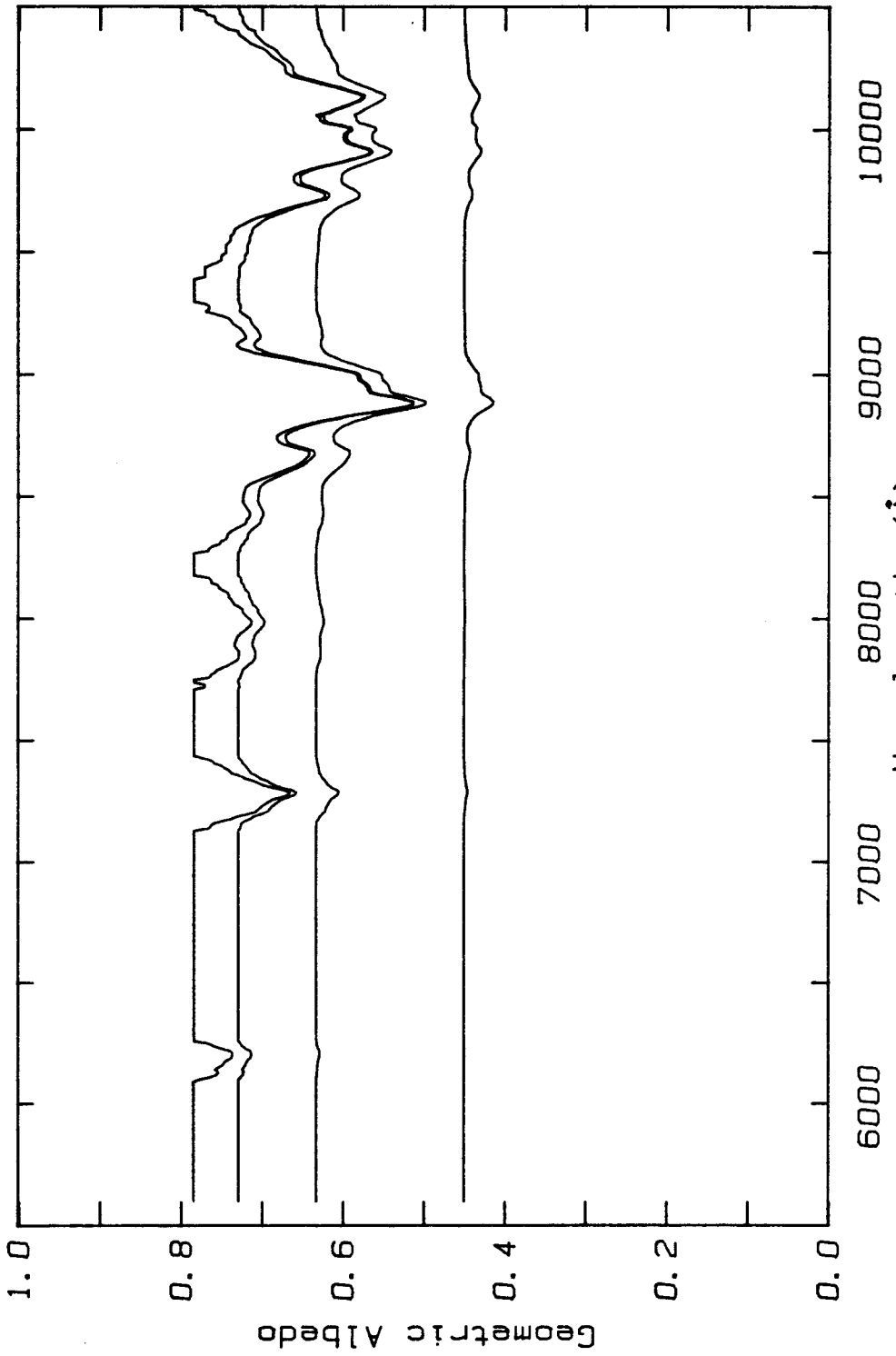

Figure 28 Effect of Continuum Optical Depth on Synthetic Spectrum

The curves shown are for P(0) = 1 and particle size of 2 mm. Top to bottom the value for τ_o is 0, 0.001, 0.01, and 0.1.

The first step in comparing the model to the data is to fit the continuum level. With the value of P(0) fixed at 1, τ_o must be determined for the two terrain types on Pluto and for Charon yielding three unknowns at each wavelength. Since each wavelength has been measured at four different rotational phases three continuum parameters can in principle be determined. Since Charon only contributes roughly 20% of the flux the model cannot be very sensitive to the value chosen for its τ_o. For this reason τ_o for Charon was constrained to be between the τ_o's for the bright and dark regions on Pluto. This now requires only two rotational phases to determine the τ_o's on Pluto.

To simplify the search for a solution five points in the continuum were picked across the spectrum at 6000, 6600, 7600, 8200, and 9360 Å. The spectra from opposite hemispheres, phases 0.49 and 0.98 (i.e. Figures 23 and 24), were used to constrain the model. To simplify the following description bright τ_o refers to the value of τ_o (at a particular wavelength) outside of the spots and dark τ_o refers to τ_o inside the spots. The discussion treats a single wavelength with the same procedure being used for all other points. The treatment of τ_o including its wavelength dependence will be discussed later.

For a given phase and bright τ_o the value of dark τ_o that yields the measured geometric albedo is a solution. Since the bright τ_o was picked arbitrarily many such solutions exist for a single phase. Figure 29 shows a plot of dark τ_o versus bright τ_o for the two phases used as a constraint. The point of intersection of the two curves yields the values of dark τ_o and bright τ_o that fits the observed

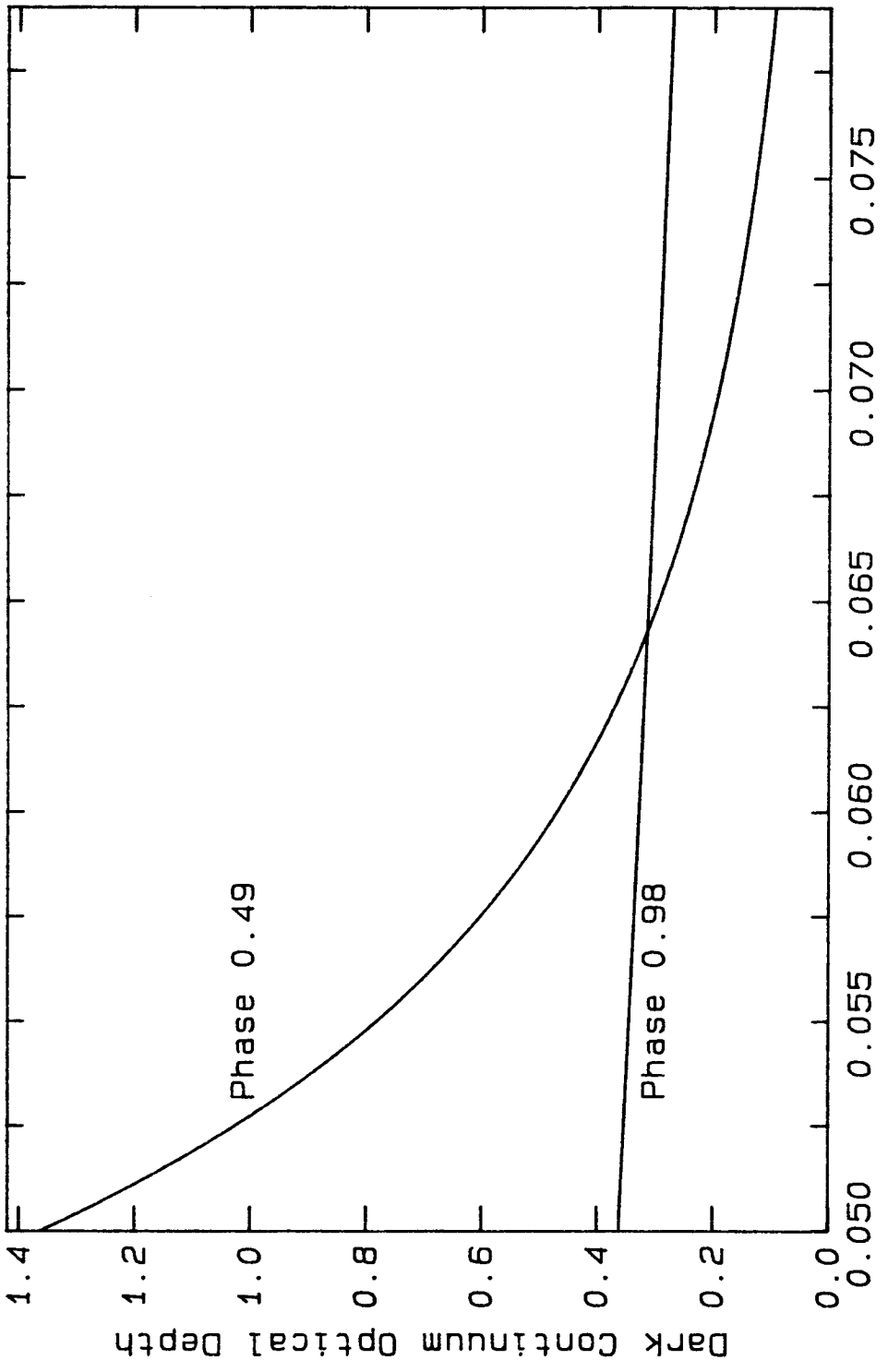

Figure 29 Graphical Solution for Pluto's Continuum Optical Depth

Plot of bright τ_o versus dark τ_o for two different rotational phases. The point of intersection matches the geometric albedos of the two phases simultaneously.

geometric albedo at two phases. This technique proved to be numerically stable but required much computation.

To specify $\tau_o(\lambda)$ the following equation was used,

$$\tau_o(\lambda) = a\lambda^2 + b\lambda + c \qquad (13)$$

The coefficients (a, b, and c) were determined from a least squares fit to the τ_o's for the five chosen points across the spectrum. Figure 30 illustrates how the model fitted the continuum for the two spectra. The coefficients that were used for the rest of the analyses are listed in Table 6.

Once the continuum is determined in the model, the methane bands can be investigated. The methane particle sizes that would match the absorptions were determined by fitting only the center of the 7200 Å band for the two phases. The best fit to the observed spectra (see Figure 31) using this model is for a particle diameter of 8.7 and 12.4 mm for the bright and dark areas, respectively. The model has accurately reproduced the phase dependent behavior of the 7200 Å band. The fit to the other methane bands is also quite good with the exception of the 8900 Å band. A major problem with the model fit is that the weak bands are too weak, or the strong bands are too strong. Multiple scattering in the frost has not enhanced the weak bands enough. Figure 32 shows the fit for particle sizes of 3.4 and 4.5 mm which matches the depths of the 8900 Å band but little else.

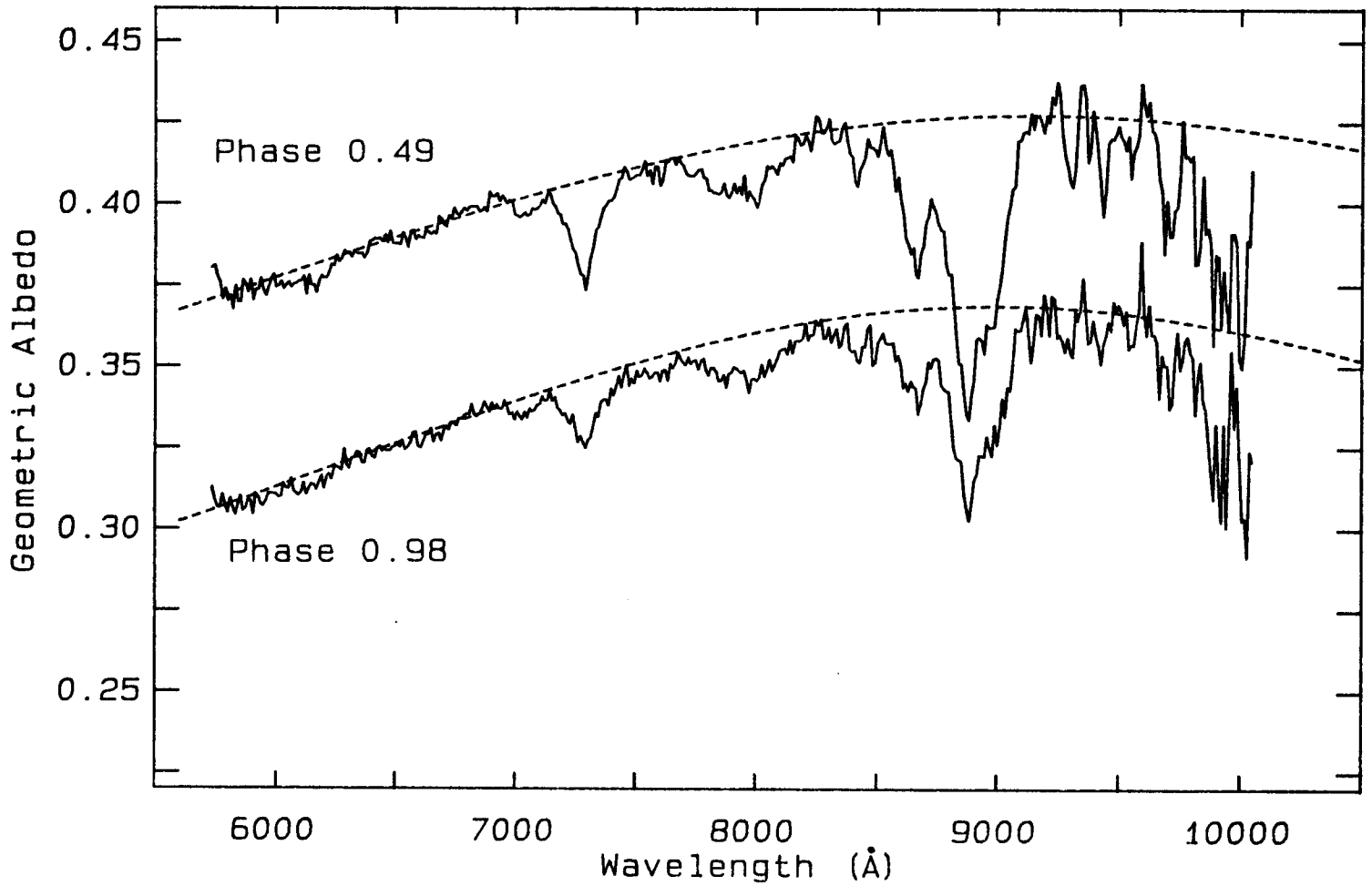

Figure 30 Continuum Fit

This shows the fit to the continuum of the Pluto spectra using the parameters given in Table 6. The top curve is for phase 0.49 and the bottom curve is for phase 0.98. The solid lines are the data and the dotted lines are the calculated curves.

Table 6

Continuum Optical Depth Quadratic Coefficients

	Bright Areas on Pluto	Dark Areas on Pluto	Charon
a	2.641(-9)	1.936(-8)	0
b	-4.763(-5)	-3.414(-4)	-1.143(-5)
c	2.543(-1)	1.659(0)	2.290(-1)

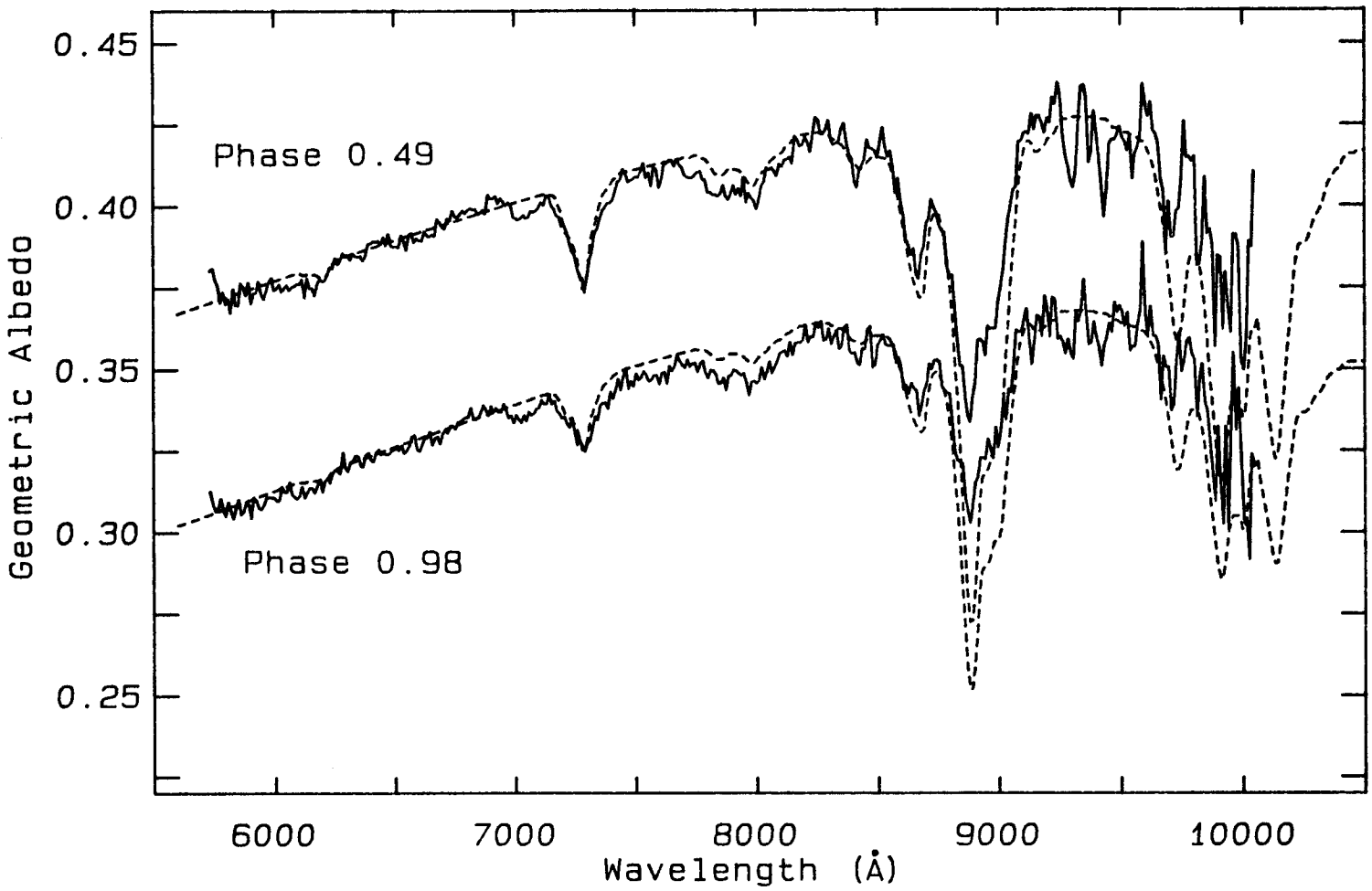

Figure 31 **Pure Frost Synthetic Spectrum Fitted to the 7290 Å Band**

This synthetic spectrum represents the best fit to the data that could be obtained with a pure frost model. The solid lines are the data and the dotted lines are the calculated curves.

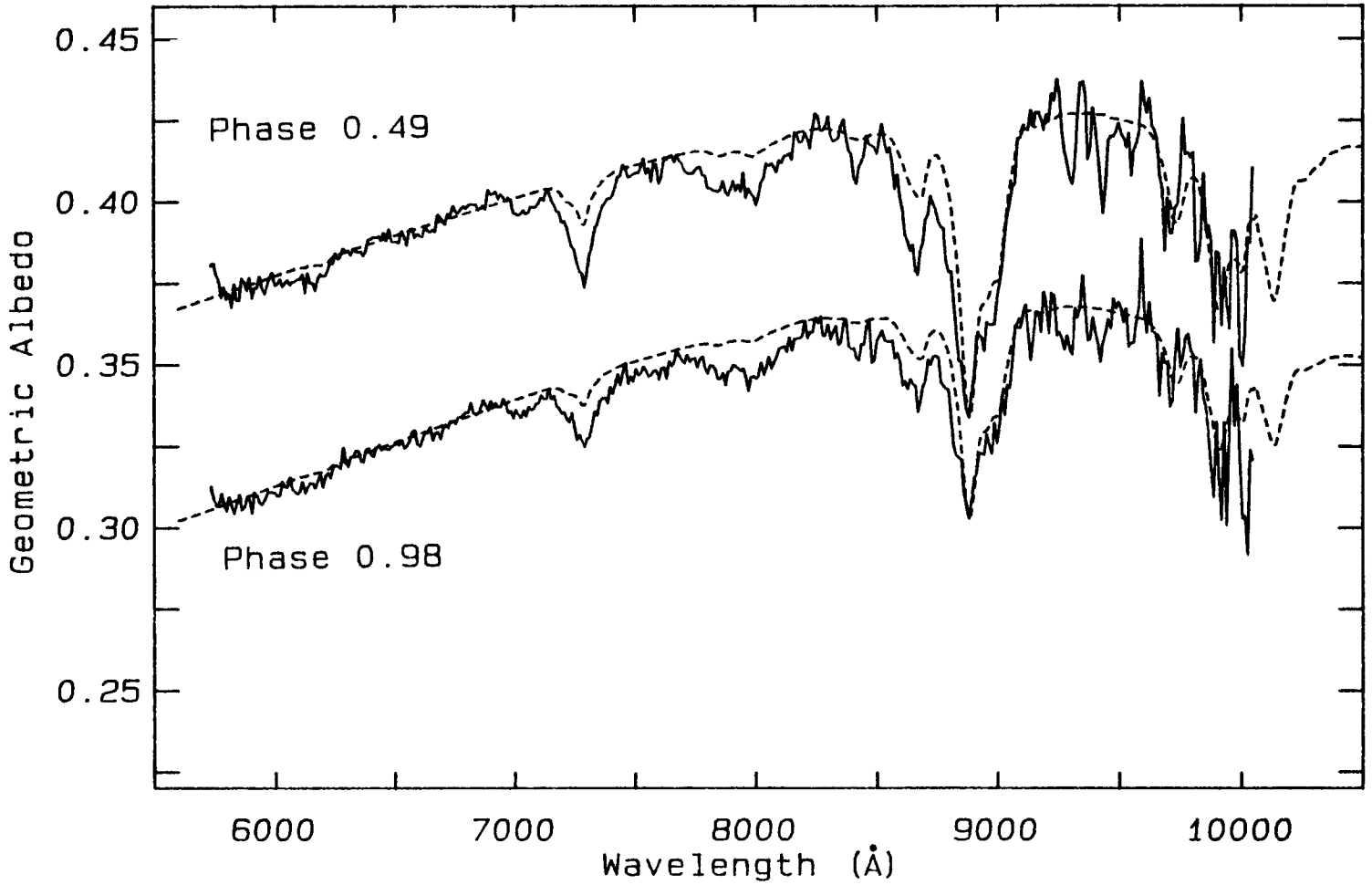

Figure 32 **Pure Frost Synthetic Spectrum Fitted to the 8900 Å Band**

This synthetic spectrum does not fit the observed spectrum as well as the one shown in Figure 31. The 8900 Å band is too strong in the model. The solid lines are the data and the dotted lines are the calculated curves.

Synthetic Gas Calculations

The behavior of an atmosphere over a spotted frost free surface will now be investigated. The continuum is fitted with the same parameters that were used for the frost. The effect of the atmosphere is included by multiplying by its transmission for each surface element. The transmission to a point on the surface as a function of μ is given by

$$\bar{T} = \exp[-\bar{\tau}(A)] \text{ and}$$
$$A = \frac{2A_1}{\mu}, \tag{14}$$

where $\bar{\tau}$ is the optical depth of the atmosphere as a function of abundance, A is the slant path two-way abundance, and A_1 is the one way column abundance along the normal to the surface (ie. unit air mass).

The procedure for calculating the optical depth of methane gas has been discussed in detail by Benner (1979). He describes the use of the Mayer-Goody or random band model with a Lorentz line shape. However for the conditions that exist on Pluto (T = 40-60 K and very low pressure) the Doppler width of individual lines will dominate over the Lorentz width. The Lorentz wings are not totally negligible but it was estimated that the effect is small. Calculating a Voight profile instead of a pure Doppler profile involves computing one more imbedded integral. This increase in computation was not felt to be justified in light of the small correction it would provide. Furthermore neglecting Lorentz broadening is an approximation that will not change the rotational phase dependent behavior of the model.

The basic assumption underlying a random band model requires many overlapping lines in a small wavelength interval (several Å), so that an "average" optical depth can be estimated for this wavelength interval and used in subsequent model calculations. This approximation should hold for the methane features considered which can be shown to consist of thousands of overlapping individual lines. For random line spacing and an assumed exponential line intensity distribution, the formula for calculating the optical depth averaged over a wavelength interval is

$$\bar{\tau}(A) = \frac{1}{\delta}\int_{-\infty}^{\infty} \frac{A\sigma f_\nu}{1+A\sigma f_\nu}\, d\nu, \tag{15}$$

where

δ is the mean line strength,

A is the column abundance,

f_ν is the line shape profile,

ν is the frequency of radiation, and

σ is the mean line strength

(see eqn. 4.26 in Goody, 1964).

The Doppler line shape profile is given by

$$f_\nu = \frac{1}{\alpha_D\sqrt{\pi}}\, e^{-(\nu/\alpha_D)^2}, \tag{16}$$

where α_D is given by

$$\alpha_D = \frac{1}{\lambda} \sqrt{\frac{2kT}{M}} \tag{17}$$

The final expression for average optical depth is

$$\bar{\tau} = \frac{Ak_\nu}{\sqrt{\pi}} \int_{-\infty}^{\infty} \frac{e^{-x^2}}{1+\frac{Ak_\nu}{\sqrt{\pi}y_D} e^{-x^2}} \, dx, \tag{18}$$

where

$k_\nu = \frac{\sigma}{\delta}$ is the mean absorption coefficient,

$y_D = \frac{\alpha_D}{\delta}$, and

$x = \frac{\nu}{\alpha_D}$.

The temperature used in Equation (17) is determined from equilibrium between the methane vapor pressure and atmospheric surface pressure. The thermodynamic expression for the vapor pressure of a gas is

$$P_v = P_o \, e^{-\ell/RT}, \tag{19}$$

where R is the universal gas constant, ℓ is the latent heat of vaporization (9.81×10^{10} erg/mole for methane), and P_o is a constant

(4.4668×10^{4} atm for methane). The surface pressure of the gas is

$$P_s = mgA, \tag{20}$$

where

m is the mean molecular weight (16 g/mole for methane),

g is the surface gravity of Pluto, and

A is the column abundance.

Over the range of column abundances investigated the equilibrium temperature falls in the range of 50 to 60 K. The transmission of the atmosphere is weakly dependent on the temperature so the actual value is not critical.

Equation (18) is integrated numerically to obtain the average optical depth. The methane gas absorption coefficients used are from long path methane absorption spectra from Benner (1979). These absorption coefficients were determined at room temperature ($\sim$300 K) for Lorentz broadened lines (Fink et al., 1977). The mean line spacing was set to a value of 0.1 cm^{-1} for all of the bands. With a constant line spacing for all the bands the model gives a reasonable fit to the relative band intensities (cf. Figures 33 and 34). Of course, from physical considerations the line spacing is not expected to be constant (see discussion in Fink et al., 1980), but the fit is quite good. If the line spacing is varied from band to band an even better fit to the observed spectrum can be obtained, but the model cannot then predict the band ratios.

The gas model clearly cannot explain the phase dependence of the absorptions. Figure 33 shows a column abundance of 9.4 m-amagats which matches the depth of the 7290 Å band for the rotational phase of 0.98. For the other hemisphere (phase = 0.49) 14.6 m-amagats is required to fit the band (shown in Figure 34). This corresponds to a change of 5.2 m-amagats in just 72 hours.

Trafton and Stern have investigated the properties of a methane atmosphere on Pluto (Trafton, 1980; Trafton and Stern, 1983; Stern and Trafton, 1984). They conclude from energy balance considerations that there are no appreciable diurnal tides in the atmosphere. Thus it is not possible to explain the observed phase variation of the spectrum using the presumed spot distribution without adding methane frost.

Final Model

The gaseous and solid methane absorptions calculated previously can be combined. An absolute upper limit to the gas abundance is found from the spectrum showing the minimum absorption (phase of 0.98). A value of 9.4 m-amagats was found under the fitting assumptions described above (see Figure 33). A more realistic model dependent upper limit can be obtained from a model which combines gas and frost. The fit to the continuum is identical to that calculated in the individual models. There are now three parameters available to specify the methane absorptions: particle sizes in the two terrains on Pluto and the column abundance of the gas. The center of the 7290 Å band was used to constrain the calculations. Figure 35 presents the possible values of the three free parameters which yield a match to the observed

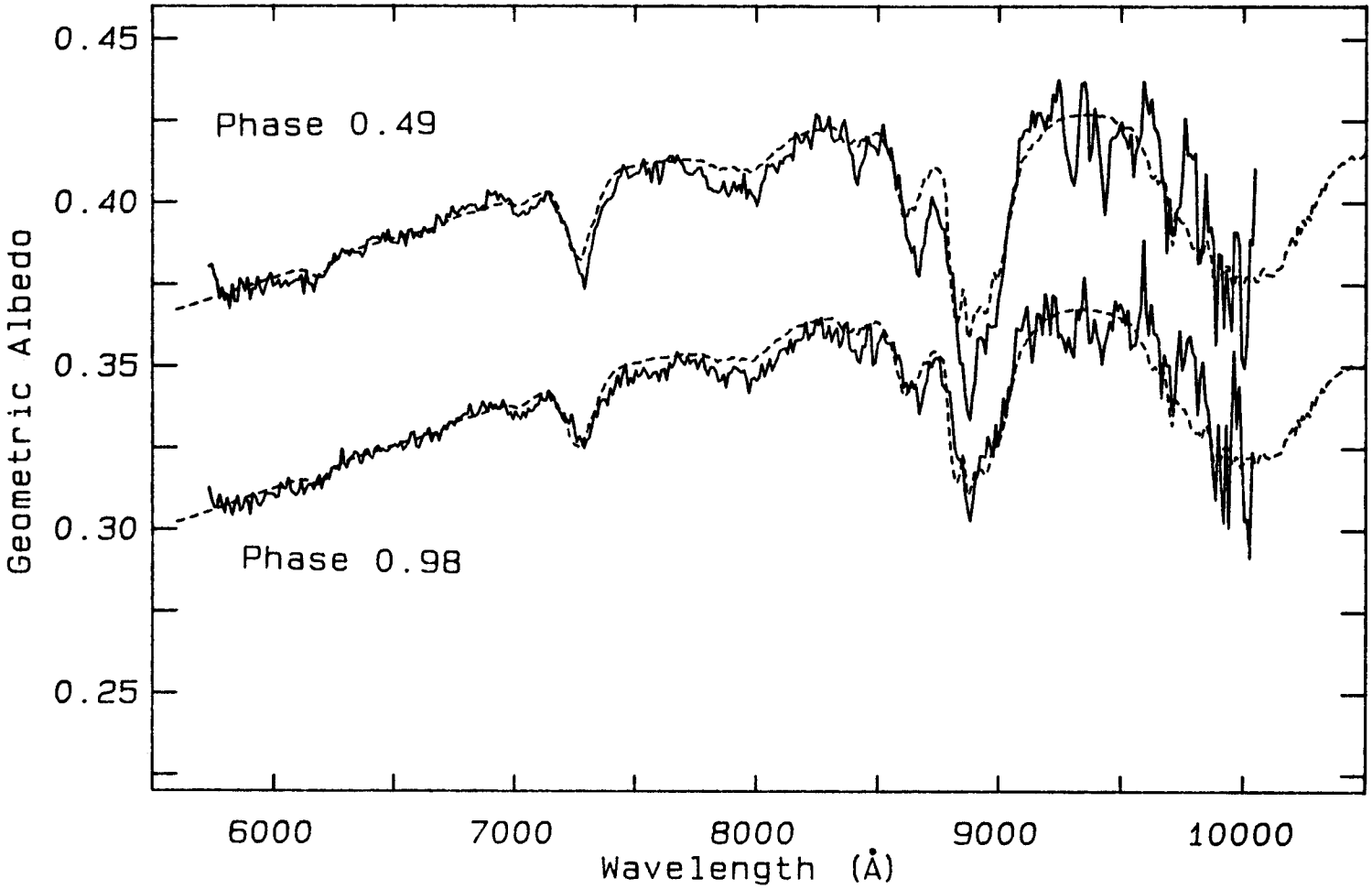

Figure 33 **Pure Gas Synthetic Spectrum Fitted to the Phase 0.98**

This synthetic spectrum represents an atmospheric fit to the data constrained by the rotational phase 0.98. The column abundance is 9.4 m-amagats. The solid lines are the data and the dotted lines are the calculated curves.

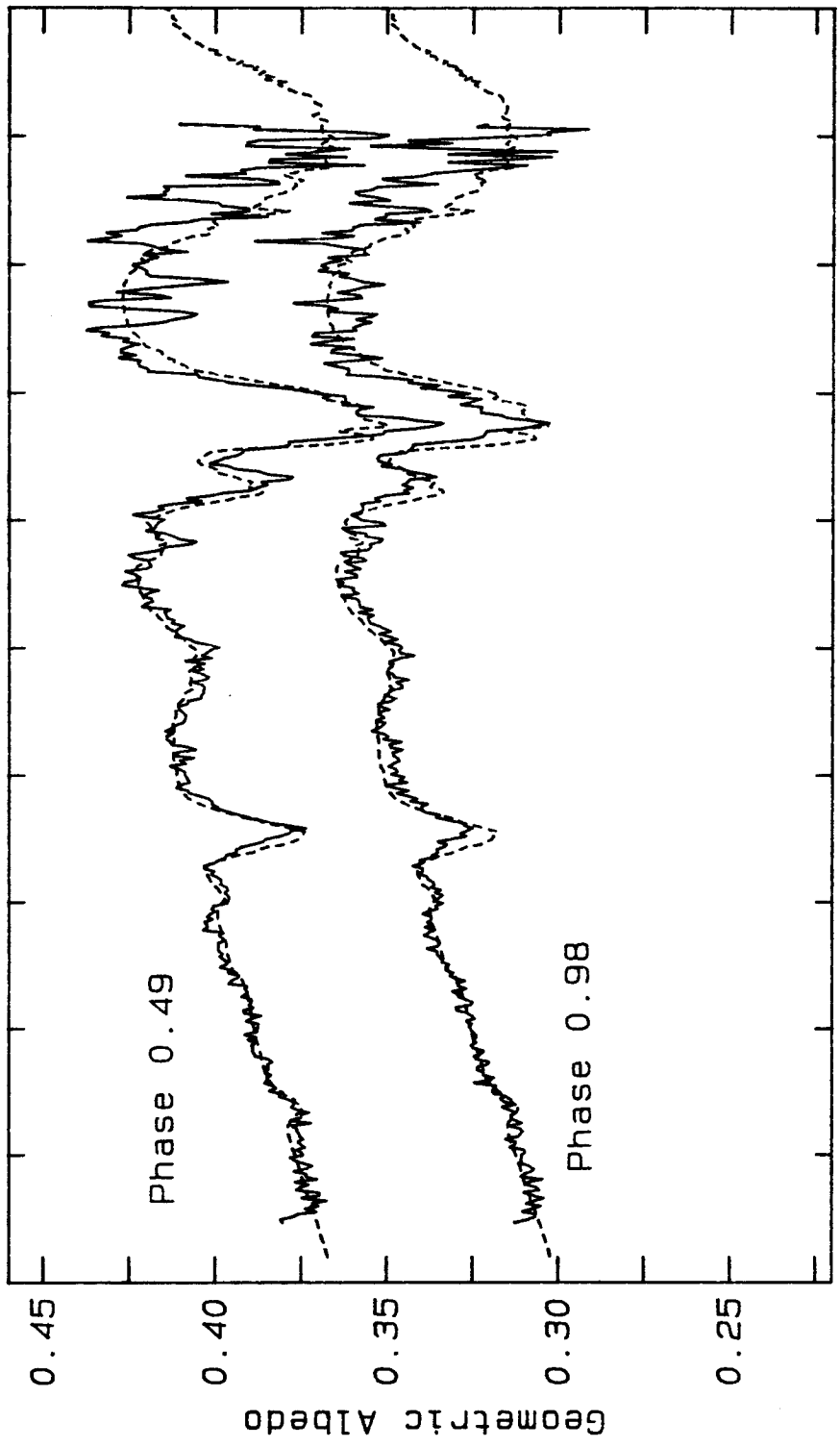

Figure 34 Pure Gas Synthetic Spectrum Fitted to the Phase 0.49

This synthetic spectrum represents an atmospheric fit to the data constrained by the rotational phase 0.49. The column abundance is 14.6 m-amagats. The solid lines are the data and the dotted lines are the calculated curves.

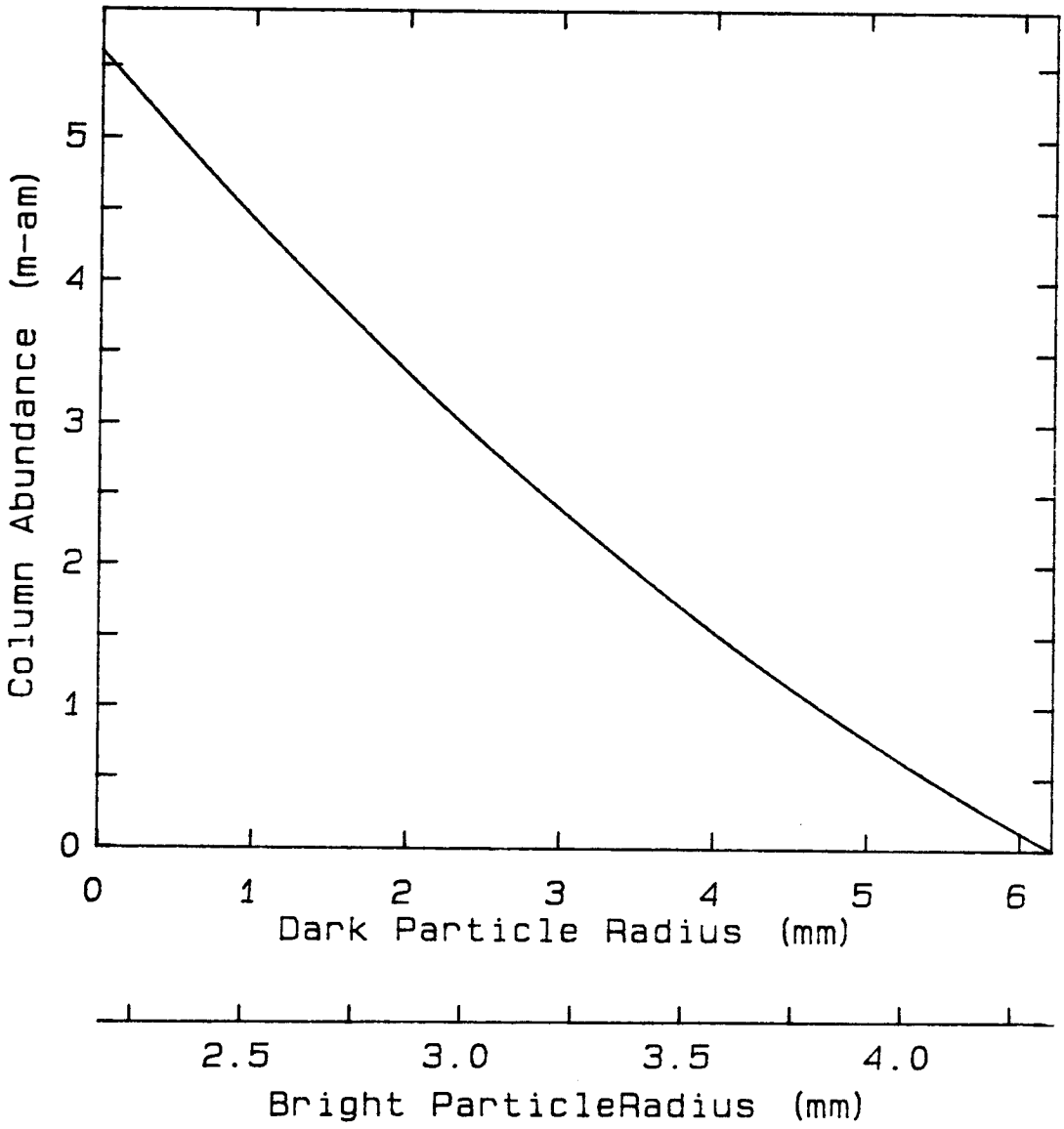

Figure 35 **Range of Model Fit to Observed Spectrum**

The line represents the values of the three parameters that yeild a match to the observed depth of the 7290 Å band in the phase 0.49 and 0.98 spectra.

spectra. The upper limit to the atmosphere is found when there is no methane frost left in the dark areas. For the present model calculations the upper limit is 5.6 m-amagats.

Figures 36 and 37 show the model fit for two selected possible solutions of the parameters plotted in Figure 35. Figure 36 shows the case with the most gas and the dark particle size is zero. Figure 37 is an intermediate case where the column abundance is 3 m-amagats and the particle diameters are 6.1 mm and 4.7 mm for the bright and dark areas, respectively. The case where the gas abundance is zero was shown previously in Figure 31. All three cases fit the 7200 Å band equally well though the fit to the 8900 Å band is not the same for all. When the gas contribution is large the relative band intensities fit better as would be expected (cf. Figure 33 and 34). However, in no case is the fit to the phase variation of the 8900 Å band as good as for the 7200 Å band.

Conclusions

Methane absorption features in the spectrum of Pluto vary with rotational phase. An atmosphere cannot explain the variation by itself. A surface distribution of methane frost with or without an atmosphere is required to explain the phase variation.

An upper limit to the gaseous column abundance assuming no frost contribution to the spectrum is about 9.4 m-amagats. This number can be increased if the weaker bands in the spectrum are fitted at the expense of the stronger ones or if an atmospheric model with varying line spacing is used (eg. Fink et al., 1980). If the spot model is

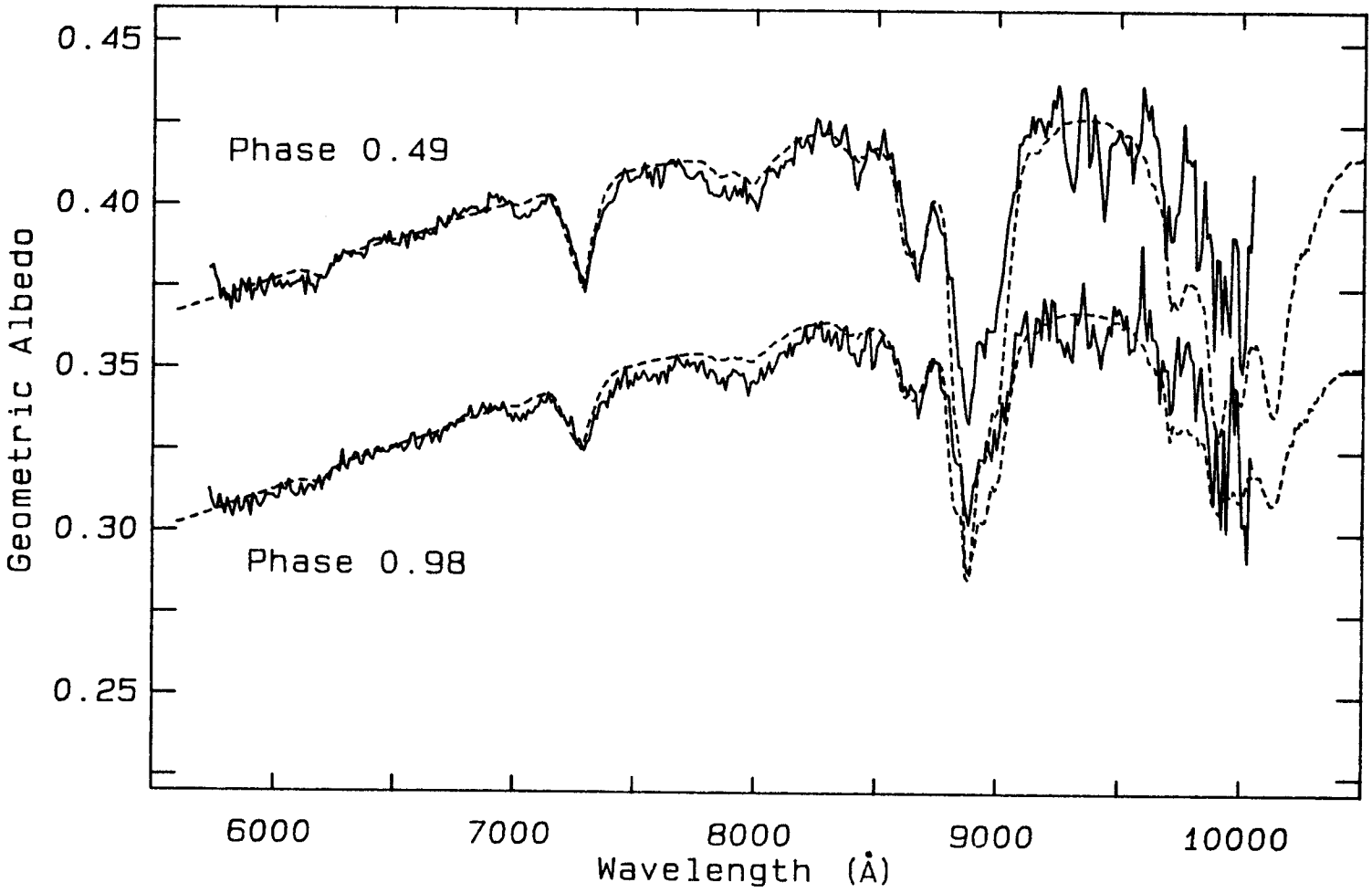

Figure 36 **Gas and Frost Model Fit at the Gas Upper Limit**

Model fit for the point from Figure 35 for dark particle size of zero. Column abundance of gas is 5.6 m-amagats and the bright particle diameter is 4.4 mm. The solid lines are the data and the dotted lines are the calculated curves.

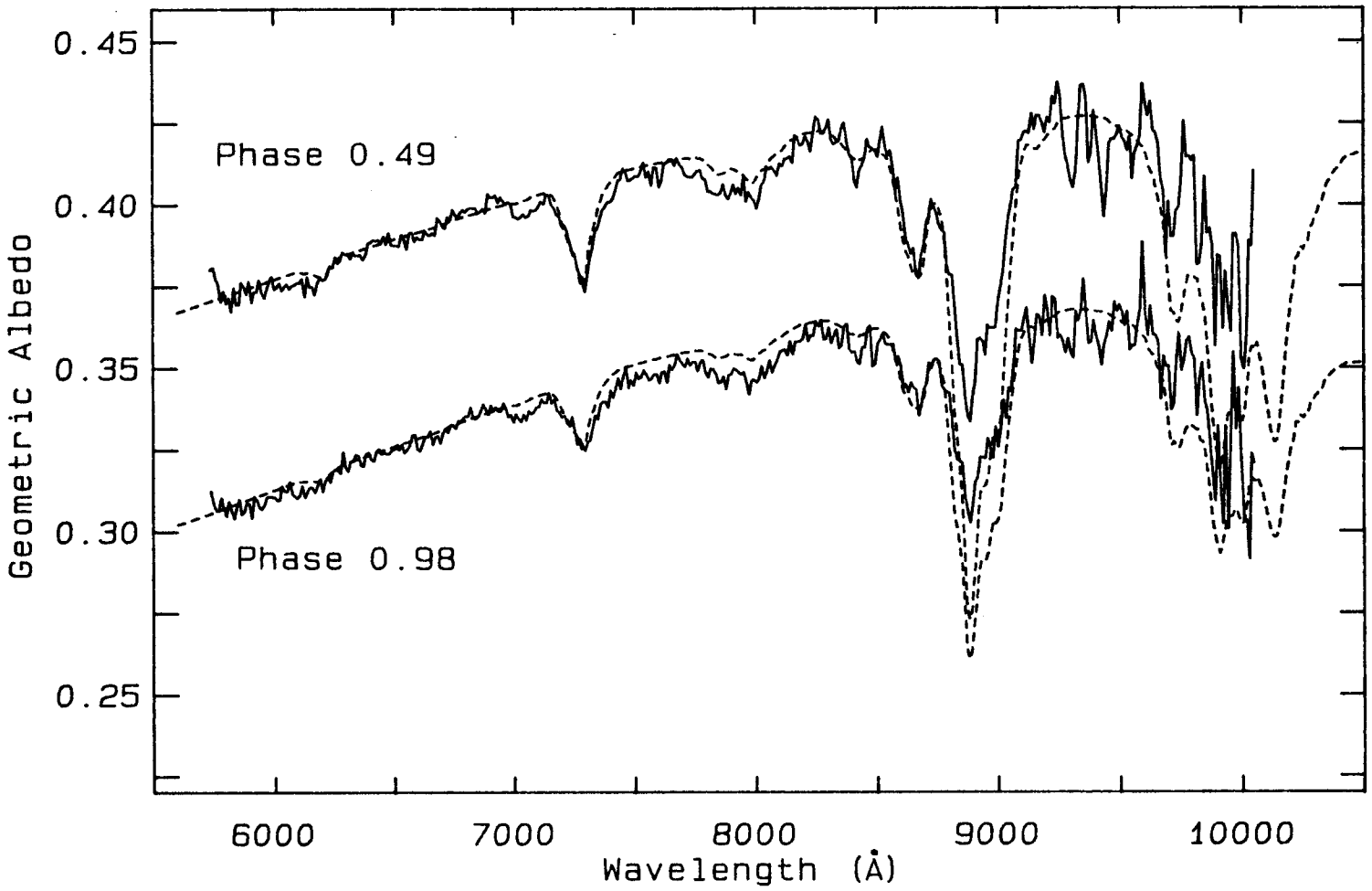

Figure 37 Gas and Frost Model Fit at a Mid-Range Solution

Model fit for a column abundance of 3 m-amagats, bright particle diameter of 6.1 mm, and a dark particle diameter of 4.7 mm. The solid lines are the data and the dotted lines are the calculated curves.

used and no methane is allowed in the dark regions the present model assumptions give an upper limit of 5.4 m-amagats. The column abundance derived from the model also depends on the light contributed by Charon. Since the satellite is assumed to be void of methane gas and frost it represents a neutral component that reduces the absorption depth for a given column abundance. If methane frost exists on the surface of Charon, the derived methane column abundance would decrease.

The model of Pluto presented in this work includes albedo variations and a distribution of methane frost along with an atmosphere of methane gas. The model can explain the rotational phase variation of the methane features. The particle sizes are predicted to be up to 12 mm in diameter. The numbers derived from the model depend on the choices made for the phase function and Charon's contribution to the total light. Changing these parameters will affect the derived particle sizes and the column abundance, but not the general apperance of synthetic spectrum.

A major problem with the model is its failure to reproduce the relative band strengths between the 7290 and 8900 Å bands. The frost is assumed to consist of a single particle size within a given terrain. The failure of the model to explain all of the methane features simultaneously might be explained by a more complex frost on the surface of Pluto. Clark and Roush, (1984) have shown that a two component frost (ie. two particle sizes) will reduce the band ratio between weak and strong features. Another possible model that might yield a better fit is one that separates the continuum absorber and the methane frost. If the the two components are separated on the surface

so that their scattering properties are independent, then the spectrum will be an average of a bright (methane) spectrum and a dark continuum spectrum and the methane absorption features will no longer be washed out by the continuum absorber. The primary goal of this research was to explain the newly discovered phase variation of the spectrum. Other models were not investigated at this time for this reason and because there is no other information yet available to help distinguish between them.

The spots on the surface of Pluto are assumed to explain the lightcurve. The photometric spot model by Marcialis (1983) matches the observed lightcurve up to 1982. The observations presented in this work were done in 1983 thus the spot model should still give a good approximation to the lightcurve. The positions and sizes of the spots can be improved using a revised ephemeris for the orientation of Pluto and by using the contrast ratio predicted from the spectroscopic model developed in this work. This correction is expected to be small and should not have a major influence on the synthetic fit to the spectra.

A more serious problem with the spot model is that it cannot explain the secular dimming of Pluto. One suggestion made by Marcialis (1983) proposes a net evaporation of methane from the surface over the past 35 years. The structure of the 8900 Å band shown in Figure 15 may be related to this net evaporation. The double absorption peak seen in the spectrum of Fink et al. (1980), verified by Apt et al. (1983), is not seen in the 1983 data. This indicates that the physical characteristics of the methane could have changed during only one year. Interpretation of this change is difficult due to the lack of

appropriate laboratory spectra, but the phenomena of increased band structure with decreasing temperature and changes in phase has been reported by Fink and Sill (1978) for methane. This is consistent with the fact that Pluto is still approaching perihelion and therefore its mean temperature should be slowly increasing. Not enough is known about methane or Pluto to fully understand this behavior at this time. Further observations are required as Pluto passes through perihelion and begins to move away from the Sun.

The absorption coefficients used for the frost were approximated by measurements of liquid methane. Measurements of the absorption coefficients for the solid will improve the spectroscopic model. Details of the band shapes could be relied upon if a laboratory comparison can be done. For the same reason it would be useful to have methane gas absorption coefficients measured at Plutonian temperatures (40 to 60 K). The gas measurements would be more difficult to obtain due to the low vapor pressure of methane at those low temperatures but would aid in separating the frost and gas contributions to the spectrum of Pluto.

The impending series of predicted mutual eclipses (most recently predicted by Hege et al., 1984) between Pluto and Charon will provide an opportunity to measure the radii of Pluto and Charon. Spectroscopy during the eclipses will yield some information about the individual spectra of Charon and Pluto. The events are predicted to last up to 5 hours and thus are well within the capabilities of current instrumentation.

REFERENCES

Andersson, L. E. and Fix, J. D. (1973). Pluto: New Photometry and a Determination of the Axis of Rotation. Icarus, 20, 279-283.

Apt, J., Carleton, N. P., and Mackay, C. D. (1983). Methane on Triton and Pluto: new CCD spectra. Astrophys. J., 270, 342-350.

Arvsen, J. C., Griffin, Jr., R. N., and Pearson, Jr., B. D. (1969). Determination of extraterrestrial solar spectral irradiance from a research aircraft. Applied Optics, 8, 2215-2232.

Benner, D. C. (1979). The Visual and Near Infrared Spectrum of Methane and its Application to Uranus, Neptune, Triton and Pluto. Ph.D. Thesis, University of Arizona, Tuscon, AZ.

Bevington, P. R. (1969). 'Data Reduction and Error Analysis for the Physical Sciences'. McGraw Hill, New York.

Binzel, R. P. and Mulholland, J. D. (1983). Photometry of Pluto During the 1982 Opposition. Astron. J., 88, 222-225.

Bracewell, R. (1965). 'The Fourier Transform and Its Applications', McGraw Hill, New York.

Christy, J. W. and Harrington, R. S. (1978). The Satellite of Pluto. Astron. J., 83, 1005-1008.

Clark, R. N. (1981). The Spectral Reflectance of Water-Mineral Mixtures at Low Temperatures. J. Geophys. Res. 86, 3074-3086.

Clark, R. N. and Roush, T. L. (1984). Reflectance Spectroscopy: Quantitative Analysis Techniques for Remote Sensing Applications. J. Geophys. Res. 89, 6239-6340.

Cruikshank, D. P., Pilcher, C. B., and Morrison, D. (1976). Pluto: Evidence for Methane Frost. Science, 194, 835-837.

Cruikshank, D. P. and Silvaggio, P. M. (1980). The Surface and Atmosphere of Pluto. Icarus, 41, 96-102.

Davies, M. E., Abalakin, V. K., Cross, C. A., Duncombe, R. L., Masursky, H., Morando, B., Owen, T. C., Seidelmann, P. K., Sinclair, A. T., Wilkins, G. A., and Tjuflin, Y. S. (1980). Report of the IAU Working Group on Cartographic Coordinates and Rotational Elements of the Planets and Satellites. Celestial Mechanics, 22, 205-230.

Fink, U., Benner, D. C., and Dick, K. A. (1977). Band Model Analysis of Laboratory Methane Absorption Spectra from 4500 to 10500 Å. J. Quant. Spectrosc. Radiat. Transfer, 18, 447-457.

Fink, U. and Sill, G. T. (1978). The Infrared Spectral Properties of Frozen Volatiles. In Comets (Wilkening, L. L., Ed.), pp. 164-202. Univ. of Arizona Press, Tucson, Arizona.

Fink, U., Smith, B. A., Benner, D. C., Johnson, J. R., Reitsema, H. J., and Westphal, J. A. (1980). Detection of a CH4 atmosphere on Pluto. Icarus, 44, 62-71.

Goody, R. M. (1964). 'Atmospheric Radiation'. Clarendon Press, Oxford.

Gunn, J. E. and Westphal, J. A. (1981). Care, feeding and use of charge-coupled device (CCD) imagers at Palomar Observatory. SPIE, 290, 16-23.

Hapke, B. (1963). A Theoretical Photometric Function for the Lunar Surface. J. Geophys. Res. 68, 4571-4586.

Hapke, B. (1981). Bidirectional reflectance spectroscopy: 1. Theory. J. Geophys. Res., 86, 3039-3054.

Hapke, B. and Wells, E. (1981). Bidirectional reflectance spectroscopy: 2. Experiments and Observations. J. Geophys. Res. 86, 3055-3060.

Hardie, R. H. (1965). A Re-Examination of the Light Variation of Pluto. Astron. J., 70, 140.

Harris, D. L. (1961). Photometry and Colorimetry of Planets and Satellites. In 'The Solar System', vol 3., Planets and Satellites, (Kuiper, G. P. and Middlehurst, B. M., eds.), pp. 272-342. Univ. of Chicago Press, Chicago, Illinois.

Hege, E. K. and Drummond, J. (1984). IAU Circular 3986.

Hege, E. K., Hubbard, E. N., Drummond, J. D., Strittmatter, P. A., and Worden, S. P. (1982). Speckle Interferometric Observations of Pluto and Charon. Icarus, 50, 72-81.

Johnson, H. L. (1965). The Absolute Calibration of the Arizona Photometry. Comm. Lunar and Planet. Lab., 3, 73-77.

Johnson, H. L. (1980). The absolute calibration of stellar spectrophotometry. Rev. Mexicana Astron. Astrof., 5, 25-30.

Johnson, J. R., Fink, U., and Larson, S. M. (1984). CCD spectroscopy of comets: Tuttle, Stephan-Oterma, Brooks 2 and Bowell. Icarus in press.

Kiladze, R. I. (1967). Physical Parameters of Pluto. Solar System Research, 1, 173-175.

Lane, W. A., Neff, J. S., and Fix, J. D. (1976). A Measurement of the Relative Reflectance of Pluto at 0.86 Micron. Publ. Astron. Soc. Pacific, 88, 77-79.

Marcialis, R. L. (1983). A Two-Spot Model for the Surface of Pluto. M.S. Thesis. Vanderbilt University, Nashville, TN

Marcoux, J. E. (1969). Indicies of Refraction of Some Gases in the Liquid and Solid State. J. Opt. Soc. Amer., 59, 998.

Neff, J. S., Lane, W. A., and Fix, J. D. (1974). An investigation of the rotational period of the planet Pluto. Publ. Astron. Soc. Pacific, 86, 225-230.

Ramaprasad, K. R., Caldwell, J., and McClure, D. S. (1978). The Vibrational Overtone Spectrum of Liquid Methane in the Visible and Near Infrared: Applications to Planetary Studies. Icarus, 35, 400-409.

Russel, H. N. and Merrill, J. E. (1952). The Determination of the Elements of Eclipsing Binaries. Contrib. Princeton Univ. Obs., 23, 1-374.

Soifer, B. T., Neugebauer, G., and Matthews, K. (1980). The 1.5-2.5 micron Spectrum of Pluto. Astron. J., 85, 166-167.

Stern, S. A. and Trafton, L. (1984). Constraints on Bulk Composition, Seasonal Variation, and Global Dynamics of Pluto's Atmosphere. Icarus, 57, 231-240.

Stroud, A. H. and Secrest, D. (1966). 'Gaussian Quadrature Formulas'. Prentice-Hall, Englewood Cliffs, N. J.

Tedesco, E. F., and Tholen, D. S. (1980). Photometric observations of Pluto in 1980. Bull. Amer. Astron. Soc. 12, 729.

Tholen, D. S. (1983). Private communication.

Tholen, D. S. and Tedesco, E. F. (1985). Pluto's Lightcurve: Results from Four Apparitions. Submitted to Astron. J.

Trafton, L. (1980). Does Pluto Have a Substantial Atmosphere? Icarus, 44, 53-61.

Trafton, L. and Stern, S. A. (1983). On the global distribution of Pluto's atmosphere. Astrophys. J., 267, 872-881.

Vilas, F. (1984). The Nature and Origin of Outer Solar System Asteroids from Reflectance Spectrophotometry. PhD Thesis, University of Arizona, Tucson, AZ.

Walker, M. F. and Hardie, R. (1955). A Photometric Determination of the Rotational Period of Pluto. Publ. Astron. Soc. Pacific, 67, 224-231.

Westphal, J. A. (1981). Private Communication.